UNIVERSITÀ DEGLI STUDI DI PADOVA

Dipartimento di Fisica e Astronomia "Galileo Galilei"

Master Degree in Astrophysics and Cosmology

Final Dissertation

Intermediate Seyfert: optical spectroscopic characteristics

Thesis supervisor

Prof. Stefano Ciroi

Thesis co-supervisor

Dr. Marco Berton

Candidate

Benedetta Dalla Barba

Academic Year 2021/2022

Alla mia famiglia, a Valerio, ai miei amici
e a tutti quelli che mi sono stati più vicini.
Ma sopratutto a me stessa per essermi
dimostrata che "volere è potere".

Abstract

Active Galactic Nuclei (AGN) are a particular class of galaxies characterized by a pretty luminous central region produced by an accreting disk. According to the Unified Model (UM) around this central structure we can recognize three regions: the Broad-Line Region (BLR) characterized by high velocity clouds, the Narrow-Line Region (NLR) with small velocity clouds, and the obscuring torus (Antonucci, 1993). The last component is fundamental in explaining the differences between AGN. According to the angle between the orientation of the torus and the observer we can find Seyfert 1 (Sy1), Seyfert 1.2/1.5/1.8/1.9 (IS), and Seyfert 2 (Sy2) galaxies (Khachikian & Weedman, 1974; Osterbrock, 1981). The second group defines what are called Intermediate Seyfert galaxies, in which both the NLR and the BLR can be seen due to the inclination. This work is focused on this kind of AGN, often ignored and never extensively studied as a class. Indeed, most of the studies tend to include them in the type 1/2 classification, causing a clear pollution of the analyzed samples. In addition, in some cases IS can be confused with Narrow-Line Seyfert 1 (NLS1). Obviously this is an effect of the composite profile of the Balmer lines, that makes difficult to easily or automatically separate IS from the other types. The aim of this work is to explore the spectroscopic characteristics of IS that could allow to define criteria to isolate them in a generic sample fo AGN. In addition, studying their properties could confirm the UM or on the contrary give new insights in the AGN structure, suggesting for example the existence of irregular emission from the accretion disk.

The study is divided in: Chapter 1 introduction on AGN and Seyfert galaxies; Chapter 2 presentation of the sample, data analysis, fitting procedure, and physical outcomes; Chapter 3 conclusions and future work.

Contents

Chapter 1

Introduction

1.1 Generalities on AGN

Observationally an active galactic nucleus (AGN) is similar to a luminous star. More precisely, an AGN can be defined as a manifestation of the accretion of gas towards a Supermassive Black Hole (SMBH) which produces a quasi-blackbody emission from viscosity (Hickox & Alexander, 2018). This radiation will interact with the clouds and the dust that surrounds the nucleus. Consequently, we have the generation of a broad band emission that covers all the electromagnetic spectra.
Interestingly, an AGN SED is distinct from that of other astrophysical objects. This is a very helpful way to separate this kind of sources from others (see Figure 1.1 for an example). As previously said, an AGN emission covers a very broad range of energies and so a multiwavelength approach is necessary.

1.1.1 Components

Historically AGN were observed in different bands and with different techniques. This led astronomers to recognize the presence of structures with various emitting or absorbing properties in order to explain the observations. In the following they are briefly presented. The general accepted view comprehends a spinning SMBH in the center of the AGN with masses between $10^6 - 10^9$ $M_\odot$ and an extension related

to the Schwarzschild radius R_S. Just outside the horizon there is an accretion flow, source of the vast majority of the power coming from the AGN. This is constituted by particles that collide and loose energy due to friction. Another important effect is the transport of these small grains towards the Black Hole (BH) called viscous drag. Probably the geometry of this component is a thin disk, even if different types are not ruled out. The emitted radiation (primary radiation) has a power-law trend of $S_\nu \propto \nu^{1/3}$ (Robson, 1996) which will be modified by absorption and scattering when it interacts with the other external structures. The power-law spectrum is the result of the superimposition of a series of almost black bodies at different temperatures (T) and radiates from optical to soft X-rays. The BLR is placed around to the accreting area and, as the name suggest, probably consists on virialized gas clouds orbiting at high speeds of $10^3 - 10^4$ km s^{-1}. A noteworthy aspect is that this structure is composed by discrete elements. As a consequence, in some particular situations, the primary radiation can be seen through the "holes" between the BLR cells. In the region from 10 to 100 pc we can recognize the presence of an optically thick torus made by dust and molecules. This torus will produce the necessary grade of extinction to obscure the accreting disk and partially, or completely, the BLR (see the difference between type 1s and type 2s). The distance limits are the natural consequence of some physical constraints. The inner one is due to grain sublimation, and the outer to the BH influence. Beyond this sort of doughnut shell, we can recognize the NLR. This is a low density gas zone in which clouds move slower with respect to BLR. In some sources this ionized part can extend towards large distances from the center and show a bi-conical shape with an opening angle related to the presence of the dust torus. In this case, we will speak about the Extended Narrow-Line Region (ENLR). At the end, it is useful to mention that some AGN present jets launched perpendicularly to the disk. This feature is produced by the infalling material towards the BH which is interacting with the magnetic field. As a consequence the matter is launched in different ways according to the parameters of the system. These particles emits synchrotron radiation observable from radio to optical/UV bands. Another crucial process is inverse Compton that produces the high frequency bump in the AGN SED (see Figure 1.1). It is important to stress

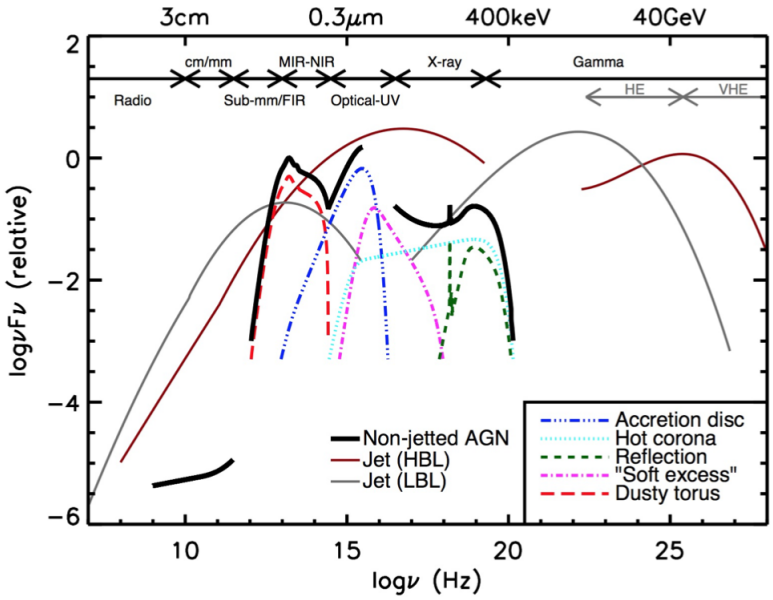

Figure 1.1: Schematic representation of two AGN spectral energy distribution: the first is showed with the black thick line and comes from a non-jetted AGN, the second one is represented by the two thin lines and comes from the jetted case. The figure is from *Järvelä (2018)*.

that jets should be treated as a relativistic process. Indeed, we need to take into account that they undergo some effects as time dilation, Doppler boosting, and beaming (Järvelä, 2018). As we will see later, the presence or not of jets is at the base for a possible classification for AGN. In Figure 1.2, a schematic view of the listed components is presented.

1.1.2 Unified Model and alternatives

One of the most significant progresses on AGN models was made by Antonucci who first theorized the presence of the obscuring torus. His studies were based on a sample of two different types of AGN (Khachikian & Weedman, 1974): what we will later define as type one (Sy1) and type two (Sy2) Seyfert galaxies. These sources show distinct spectral properties as the presence (or not) of forbidden lines from the BLR, line widths, and so on. Using polarized light something happened: NGC 1068, a classical Sy2, showed a polarized flux similar to a Sy1 (Antonucci & Miller, 1985). This discovery can be explained in different ways: either Sy2 do not have the nuclear component or it is obscured. A point in favor of the second possibility is the larger degree of extinction measured in Sy2. This brought Antonucci to propose

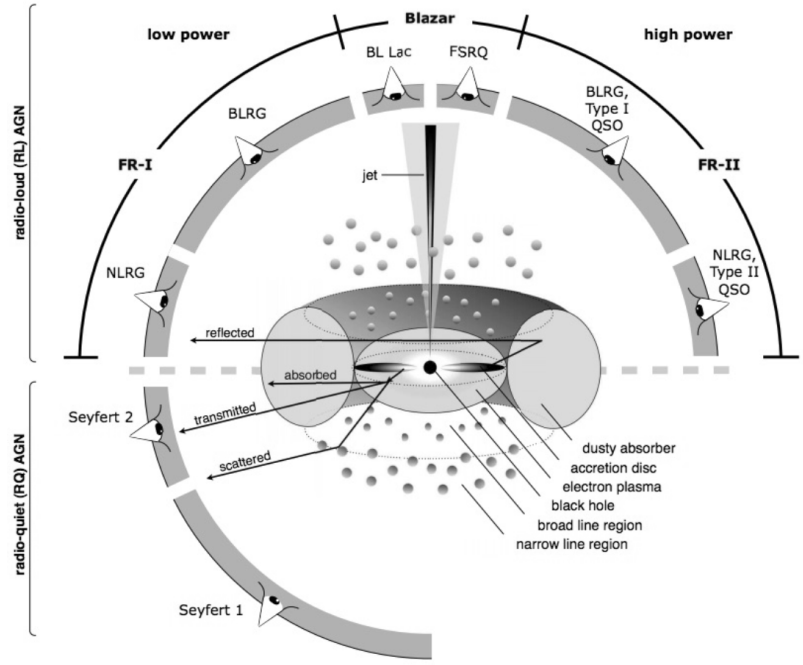

Figure 1.2: A possible representation of an AGN and all its components. In particular we can distinguish the SMBH, the accretion disk, the BLR, the NLR, and the obscuring torus. The figure is from *Järvelä (2018)*.

the presence of a screening structure with the geometry of a doughnut, or more elegantly a torus. To confirm the UM, some evidence can be shown: the general tendency of the NLR to align with respect to radio structures and the bi-conical appearance of the ionized material (Antonucci, 1993). The torus is made by an uneven distribution of dust, the most important prove of it is related to the mid-IR emission. In the UM the dust should obscure the radiation coming from the central regions, but the observations show how the mid-IR part of the spectra can reach the observer. Another point in favour of the clumpiness of the torus is the presence of Si absorption often related to large-scale structures, rather to a smooth and small-scale torus. For the dimension and the localization one should remind that this structure feels the attraction from the SMBH and not disgregate the molecules through sublimation. Summarizing, the presence of the torus and its orientation are fundamental in explaining the difference between some types of AGN. An important parameter linked to the angle is the covering factor (f_c) which defines the AGN portion shielded by the absorbing clouds (Hickox & Alexander, 2018).

Obviously this is not the only model presented. We have two interesting alternatives:

obscuring filaments and disk luminosity (Trippe et al., 2010). The former consists on an intrinsic reddening made by dust structures in the form of filaments. These dimmers can be localized between the BLR and the NLR, or in the same scale of the NLR. The problem with this scenario is that the measured extinction of the two regions is almost the same $E(B-V)_{NLR} \sim E(B-V)_{BLR}$. In this case the galactic absorption should give the most relevant contribute. The latter is based on an irregular emission from the continuum, which is an even more intrinsic explanation for the differences. An important discovery in agreement with this theory is the importance of the AGN disk luminosity (L_{AGN}^{disk}) in modeling the active galactic SED instead of the viewing angle (Ramos-Padilla et al., 2021). As always, there is not a unique "big theory" which is able to solve and explain all the observational problems and discoveries: the right solution is probably a mixed-bag of those previously proposed.

Finally, a brief possible scenario for the formation and evolution of an AGN. The BHs at early cosmic epochs are related to two main processes: an important accretion rate, comparable or even higher to the Eddington ratio ($\dot{M} = L_{bol}/L_{Edd}$), and merging. Depending on the activeness grade of the seed BH, related to $\dot{M}$, we can divide between two feedback scenarios: a "quasar regime" achieved through large-scale inflows triggered by galaxy mergers, and a mechanical one where the AGN-driven bubbles are injected into a gaseous environment. This view can also explain the black hole and stellar mass densities together with the BH influence on the evolution of their host galaxies (Sijacki et al., 2007).

1.2 Classifications

As we just saw AGN are pretty complicated objects. A direct consequence is that there is not a unique way to classify them. A possible solution is considering a single band and obtain specific characteristics for each type of active nuclei. Some classifying parameters are, for example: the presence or not of jets, composed profiles for the spectral lines, the value for the column density, and so on. Exploiting these points we can operate the following separations.

1.2.1 Jetted and non-jetted AGN

Let us start with the radio wavelengths. The most significant emitting sources in this band are jets. AGN can be classified in radio-loud and radio-quiet sources using the presence or not of these features. Generally speaking the 10% of active nuclei can be considered radio-loud (Järvelä, 2018). This division, in any case, is not so strict because also in radio-quiet sources there can be relativistic jets emissions. Furthermore lobe-dominant radio sources shows similar IR/optical/UV properties to radio-quiet AGN (Antonucci, 1993). Radio-loud objects form synchrotron radiation through the interaction between a flux of relativistic electrons and the magnetic field generated by the BH. There are two possible physical mechanisms for creating jets: the first one is extracting the energy from the black hole spin, and the other one from a magnetized accretion disk. The BH mass (M_{BH}) in any case seems to not correlate with any other observed property (Järvelä, 2018).
The quantitative classification method uses the radio loudness R_{radio} defined as the ratio between the flux at 6 cm and the optical one at 4400 Å. If R_{radio}>10 we have a radio-loud object. Another possible parameter is the power at 5 GHz. In this case we have again radio-loud galaxies if $P_{5GHz} > 10^{24}$ W Hz^{-1} (Komossa, 2018).
Before changing energy range, is useful to stress that we started with the aim of dividing AGN using the tool "presence/absence of jets" but we ended up with this kind of feature in both the classes. This is a clear example of how is difficult to find precise limits and boxes in which nature should fit. In reality galaxies present continuous properties. Another aspect to stress is the difficulty in exploiting the radio loudness as a classification parameter. In the past decades it has already become clear that the R_{radio} distribution of AGN is not bimodal. Furthermore, other characteristics as the host galaxy contribution and the variability of the radio flux tends to misclassify the sources (Berton & Järvelä, 2021).

1.2.2 Optical spectra and Seyfert galaxies

AGN are a very intriguing type of objects under the optical point of view. Their spectra show a lot of emission lines with the most diverse properties. The initial

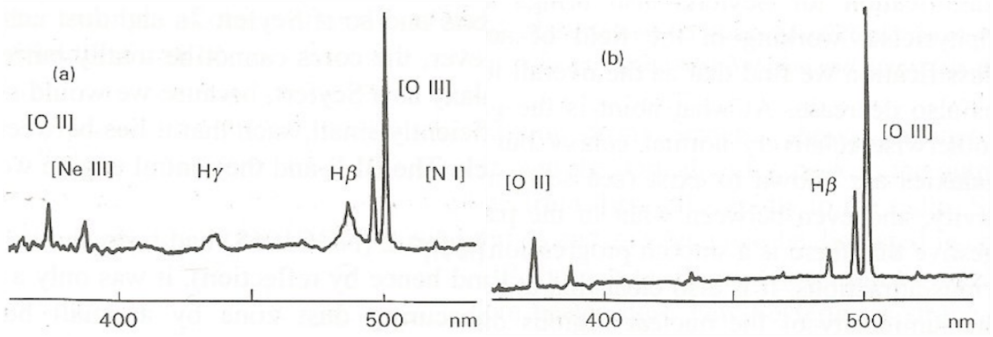

Figure 1.3: Comparison between two spectra from different types of Seyfert galaxies. On the left we have an example of Sy1 and on the right of Sy2. In the first case one can recognize a broad component superimposed to the narrow one, while in the second case there is only the narrow one. The figure is from Robson Ian, *Active galactic nuclei*, 1996, p. 75.

aim is to differentiate them from classical galaxies. Using specific line ratios one can create two interesting classification systems called BTP and VO diagrams (Baldwin, Phillips and Terlevich 1981; Veilleux & Osterbrock 1987) respectively. The idea is that the spectral continuum between AGN and Star-Forming Galaxies (SFG) is completely different. This is related to the nature of this emission: in the first case it comes from the central regions, while in the second from the stars. Using the ratio between the ionized forbidden lines flux and the neutral permitted ones we can separate the two types (Hickox & Alexander, 2018).

In Figure 1.2, we can recognize that the differences between AGN depend on the observer's position. In the UM the inclination angle can identify at least three types of AGN: Sy2 (edge-on), Sy1 (intermediate inclinations), and blazars (face-on). Focusing only on Seyfert galaxies the main characteristics are: intermediate inclination angles and a V-band absolute magnitude of $M_V > -23$ mag (Robson, 1996). The second property comes from the separation between Seyferts and quasars, another important component of the AGN family. Initially Seyfert galaxies were divided in two classes according to spectral lines properties: Sy1 present permitted lines from the BLR and NLR together with forbidden lines from the NLR, while Sy2 only from the NLR (Khachikian & Weedman 1974). In turn this is related to the lines profile, the emission from the BLR is broader ($\sim 10^4$ km s^{-1}) with respect to the NLR one (Weedman, 1977). In the UM this is explained in terms of the visibility of the BLR. In Sy1 this structure is not shielded by the presence of the absorbing dust, while in

Sy2 the angle is such that only the NLR can be seen (Antonucci, 1993). An example for the spectral differences is presented in Figure 1.3.

As an alternative to spectral features, the AGN SED can be used in separating the classes. Type 1 sources present bluer colors in the optical-UV band due to their spectral shape and extinction properties. Type 2 are in general redder because of the larger grade of absorption (Ramos-Padilla et al., 2021). Another possibility is comparing permitted/forbidden line ratios, in particular Hβ with [O III]. This is useful because broad Balmer lines are typical of Sy1, while narrow forbidden ones can be found in both the two types. The difference comes from the characteristics of the forming regions, again BLR and NLR. The two Full Width at Half Maximum (FWHM) can be of the order of $\sim 10^4$ km s^{-1} for the Balmer lines and $\sim 10^3$ km s^{-1} for the oxygen. Instead, for the Sy2 the width of the two types of line is comparable, again see Figure 1.3 (Weedman, 1977). When Hβ is not visible an interesting tool for the classification is the ratio between the narrow and the broad components of the Hα line. The reference equation is (Netzer, 1990; Piconcelli et al., 2006):

$$Type \sim 1 + \left[\frac{I(H\alpha_n)}{I(H\alpha_b)}\right]^{0.4} \tag{1.1}$$

This directly gives the Seyfert type. As we will see later this relation is useful not only for the basic division type 1/2, but also for the intermediate classes.

As mentioned at the beginning, Seyfert galaxies can be sub-classified in type 1.2/1.5/1.8/1.9 according to the prominence of the broad component. In Sy1.2 the BLR emission dominate the profile, while it is almost invisible in 1.9 (Osterbrock, 1981). The separation between these types can be done through similar methods as before. The forbidden/permitted lines one is basically the same and exploits $F([OIII])/F(H\beta) = \mathrm{R}$. According to the result we can define: Sy1 if R<0.3, Sy1.2 if 0.3<R<1, Sy1.5 when 1<R<4, Sy1.8 when R>4, and Sy1.9 when only the Hα is broad (Whittle 1992; Benitez et al., 2012).

A noteworthy aspect is that some authors stressed the difficulty in obtaining a solid separation. In particular when we are dealing with low Signal to Noise (S/N) spectra (Järvelä et al., 2020). In this case some external agents can influence the classification:

the host galaxy and its subtraction (Trippe et al., 2010), the low resolution which produces fainter line wings typical of the BLR emission (Berton et al., 2020), and so on. Automatic separation, which is widely employed with a large amount of data, suffers all these problems so it is important to select only very high quality spectra in the scientific analysis.

1.2.3 Compton-thin and thick objects

Continuing in the electromagnetic spectra we can find X-rays and γ-rays. The X-ray based classification is one of the most complete and is based on the study of the accretion disk radiation absorbed by the shielding material and then re-emitted. In particular, the obscuring component in this case is made by gas rather than dust and, as for the torus, it is organized in discrete clouds. The natural consequence is that AGN are classified as Compton-thin if $N_H < 10^{25}$ cm^{-2}, where N_H is the column density. Conversely, they are Compton-thick. A further division can be done, we have unobscured sources when $N_H < 10^{22}$ cm^{-2} and obscured ones when 10^{22} cm$^{-2} < N_H < 10^{25}$ cm^{-2}. The unobscured sources present a tight relationship between X-rays and optical-UV emissions (Hickox & Alexander, 2018). Another intrinsic relation involves the primary radiation (from the disk) and the X–rays emission from the hot electron corona (Lusso & Risaliti, 2016).

As an alternative we can exploit the spectral features. The X-rays emission has a power-law trend given by N(E)$\propto E^{-\Gamma}$ where N(E) is the photon energy, E the energy, and Γ the photon index. Another interesting feature of the AGN X-ray spectra is the iron line (Fe Kα). This is produced by the material very close to the accretion disk, so it can present also relativistic effects. Exploiting these characteristics we can differentiate the sources using: $\Gamma < 1$, EW(Fe Kα)>500 eV, and F(2-10 keV)/F([O III])<1 similarly to the optical case. If at least two of these points were true, the active nucleus is defined as Compton-thick, otherwise Compton-thin (Hernandez-Garcia et al., 2017).

Interestingly, obscured AGN probably have a fundamental role in the X-rays background (XRB). For years astronomers tried to explain the faint and uniform X-rays emission coming from all the sky directions. More recently they agreed on the

theory for which small and unresolved AGN should form the background (Hickox & Alexander, 2018). In principle with more sensitive instruments these sources will be studied as single objects.

1.2.4 Changing Look sources (CL)

The AGN world is even more complicated than this. Some sources tend to vary in time and in classification. Possible explanations could be intrinsic short term disk instabilities, jet emissions, and long term variations in the absorbing column (Quillen et al., 2000; Hernandez-Garcia et al., 2017; Guolo et al., 2021). The first hypothesis is related to the behavior of the emitting source, and so to the luminosity in the soft range $L_{2-10keV}$. Jetted sources show two distinct emission states: the low one related to the accretion disk and the high one characterized by a new ejection into the jet. This is accompanied by an increase in the flux density in the γ-rays and an optical-UV enhanced emission, separated by a time lag (Järvelä, 2018).
Some authors found an higher number of variable sources between Sy1.8/1.9 samples with respect the other Seyfert classes (Quillen et al., 2000; Guolo et al., 2021). Studying these AGN they stressed how the most significant parameter under this point of view was the absorption column. This favors the external obscuring theory rather than the intrinsic one (Hernandez-Garcia et al., 2017; Guolo et al., 2021). Obviously this has some consequences. The more direct ones are an anti-correlation between $N_H - L_{2-10keV}$ and the constancy of the intrinsic luminosity. Unfortunately these two predictions are not valid, so probably these AGN change their look as a result of intrinsic variations and only partially due to N_H. Another proof is a synchronous variation of the Seyfert type with luminosity, related in turn to the Eddington accretion rate (Guolo et al., 2021). As always, results are not so easy to interpret and other studies need to be done.
Finally, some authors (Elitzur et al., 2014) stressed the possibility of a correspondence between the spectral classification and an evolutionary scenario: Sy1 $\rightarrow$ Sy1.2/1.5 $\rightarrow$ Sy1.8/1.9 $\rightarrow$ Sy2. Following this approach, the intrinsic variations are related to an evolution of the BLR with a decreasing of $\dot{M}$ regulated by the ratio between the bolometric luminosity (L_{bol}) and M_{BH}. In this view, type 2s are not obscured type

1 nuclei, but "true" Sy2 where even in polarized light broad lines are not present (Guolo et al., 2021). The difficulty in obtaining solid information about CL sources is related to the long-time and multiwavelength observations needed.

1.3 IS: what we know

Seyfert galaxies cannot only be separated in two classes, so we need a further distinction. This is mainly due to the fact that some sources, defined as IS, present spectral characteristics in between the main groups. These objects are particularly interesting, since their dual nature tend to mix both with Sy1 and Sy2 contaminating the samples (Vaona et al., 2012; Berton et al., 2020; Peruzzi et al., 2021). The results are scientific works based on, for example, type one objects with some "polluting" intermediate ones. In the following is presented what is the knowledge to date of these kind of Seyferts. An important thing to keep in mind is that not so many authors dedicated specific papers to this argument and so a lot of the listed properties are common also for Sy1 or Sy2 samples.

1.3.1 Radio band (3Hz-30GHz)

The radio emission from normal galaxies is dominated by ionized gas and relativistic cosmic rays electrons, which emit through free-free and synchrotron respectively. If we consider AGN, together with the stellar component of the host galaxy we should take into account also for the jets. As we have seen formerly, the radio classification divides AGN in jetted and non-jetted objects (Perez-Torres & Alberdi, 2007), even if this separation is not so meaningful as Berton & Järvelä (2021) demonstrate, see section 1.2.1.

When we are dealing with jets in active galaxies the two mechanisms to cite are: synchrotron for the radio/infrared/visible bands and inverse Compton for X/γ-rays. Considering the first one, the material which is accreting towards the central SMBH can interact with its magnetic field and generate electron flows. Due to the proximity of the BH, some relativistic effects are present: time dilation, Doppler boosting, and beaming. The radio spectra assume a power-law trend of the type $F_\nu \propto \nu^\alpha$

where α is the spectral index. The value of this parameter changes according to the considered region: ~ -0.7 for the extended components (Robson, 1996), while ~ 0.4 for the nuclear and compact ones (Perez-Torres & Alberdi, 2007).

The study of AGN cannot be limited to the radio band. Indeed some of these sources do not emit in this energy range, while some SFG can infiltrate in the samples. The idea is to complete the observations using the infrared (IR) emission. In general SFG present a relation between IR and radio emissions, while AGN do not (Hickox & Alexander, 2018).

Speaking about the different Seyfert types, an interesting discriminator between the classes is the ratio of the radio power (P_{21cm}) to the optical featureless continuum luminosity (L_{cont}). In particular Sy1 show higher L_{cont} than Sy2, and slightly lower P_{21cm} with respect to Sy2. Furthermore, the intermediates tends to fall in between the two other groups. A similar trend can be observed in the radio/mid-IR emissions diagram (Ulvestad et al., 1986). These results seem to be in contrast with the UM, where IS and Sy2 are Sy1 with an increasing obscuration. Indeed the re-radiation effect should produce an higher IR to radio ratio for type 2s and intermediates instead of type 1s.

1.3.2 Infrared band (1mm-10μm)

The main emission mechanism in this case is the thermal one from the heated dust in the torus, which in turn is related to the covering factor (Robson, 1996). The completeness of the selection of AGN through the mid-IR waveband is very high. The completeness is a concept related to the number of sources that can be found through a specific selection method with respect the total one. In the IR it is high due to the absence of obscuring structures able to block this radiation. Unfortunately the contamination can be very high. Studying the spectral energy distribution and color-color diagrams one can easily distinguish AGN and recognizing their peculiar trend, see Figure 1.1 (Hickox & Alexander, 2018).

Starting from the Far-IR (FIR) spectroscopy we can say that, again, the fundamental radiative component is dust. As a consequence the spectra is dominated by some emissions as the CO molecular lines. The relative strength of the rotational transitions

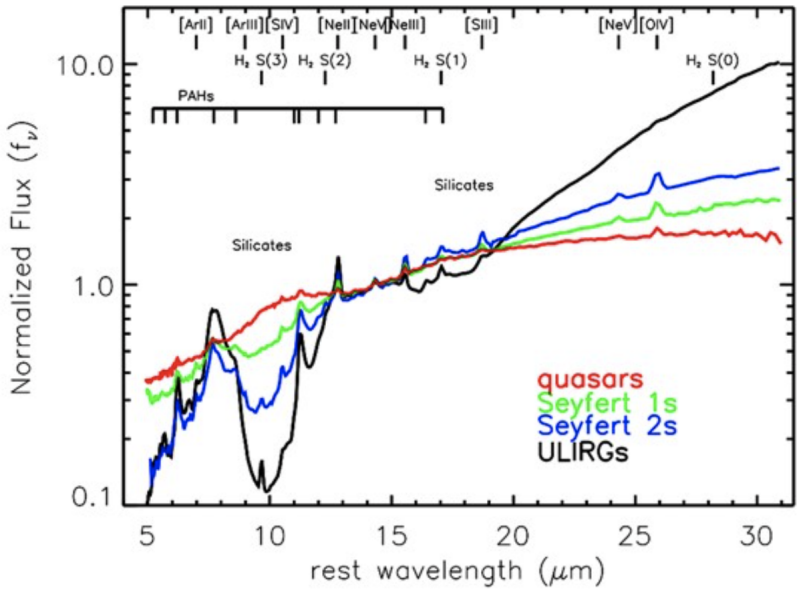

Figure 1.4: Different AGN types and their mid-IR spectra. Some features are indicated: the PAH bands at low wavelength and the silicate absorptions typical for obscured objects as Sy2. The figure is from *Hao et al., 2007*.

depends on the exciting mechanism, which in turn can be related to the heating by an AGN or starbursts. The distinction can be performed using the relation between the radio and the IR bands that we saw in the previous section. In particular, the FIR luminosity (L_{FIR}) and the total radio continuum are strictly tied for the normal galaxies. This dependence is interpreted as the heating of the Interstellar Dust (ISD) coming from supernova explosions. Then the absorbed energy is re-emitted by the ISD in the FIR wavelengths. The far-IR/radio relation is expressed in terms of the ratio q. Following this reasoning, q is an indicator of the relative importance of the AGN or the starburst emission in a galaxy (Perez-Torres & Alberdi, 2007; Hickox & Alexander, 2018).

For the Mid-IR (MIR) point of view other relevant features are generated by Polycyclic Aromatic Hydrocarbons (PAH) and the host galaxy (Trippe et al., 2010). These two components produce multiple polluting stripes which covers all the infrared spectra. The reason again lies in the molecular emission and in the dusty environment in which Seyfert tend to be found, namely in host spiral galaxies (Hickox & Alexander, 2018).

After the spectra correction, the data analysis is concentrated in the fitting procedure.

The most common models in the MIR are: a single Power-Law (PL) typical for Sy1 and a Broken PL (BPL) or a PL with silicates Absorption (APL) for Sy2 (Deo et al., 2007). It is clear that a relation between the Seyfert type and the adopted model is present. Particularly, more complex power-laws as BPL and APL are frequent in type 2s, while simplest models as PL fits well type 1s spectra. Together with the continuum, another important spectral feature are silicates. Referring to Figure 1.4, we can see their role: for obscured AGN the Si absorption is dominant at small wavelengths, while for unobscured sources the same feature is commonly in emission (Hickox & Alexander, 2018). Using these parameters, e.g. the continuum shape and the lines type, we can built a classification tool for the Seyferts in the IR. More precisely, the MIR spectral diagnostic is based on relations between parameters as the spectral indexes (given a PL profile for the continuum) of 6-15 μm and 20-30 μm. In this case Sy1.8/1.9 fall among Sy1 and starburst. Other interesting quantities are the Equivalent Widths (EW) of silicates at 10 μm and the spectral index at 20-30 μm, or the EW of PAH bands at 30 μm and the same spectral index as before. Finally, line ratios as [O IV]λ25.89 μm/[Ne II]λ12.81 μm and [Ne III]λ15.56 μm/[Ne II]λ12.81 μm with tight correlations between Sy2 and intermediates (Deo et al., 2007).

Despite the spectral differences presented before, when we are dealing with MIR imaging, obscured and unobscured AGN have similar properties. This led astronomers again to the conclusion that the dusty screen (torus) is clumpy rather than uniform. Expanding this point, a second proof of this uneven distribution comes from density (ρ) and temperature (T) studies. Some authors measured different (T, ρ) values in distinct parts of the torus for the same object. These results brought them to confirm the irregular nature of this component (Hickox & Alexander, 2018). Information on these physical quantities can be obtained by exploiting the previous listed parameters, in particular those related to the continuum and its extinction.

Last but not least, the Near-IR (NIR) band is a range characterized by an host galaxy emission peak. This unfortunately limits the ability of differentiate between the host and the AGN. A possibility can be to perform polarization measures at 1.6 μm. This would help in differentiate between a thermal or non-thermal origin

for the NIR emission (Quillen et al., 2000). Another possibility is to use diagnostic diagrams. The clearest separation between H II regions and Seyferts comes from: [S III]$\lambda\lambda$9069,9531/Hα versus [O II]λ7325/Hα, [S III]λ6724/Hα versus [O II]λ7325/Hα, and [O III]λ5007/Hβ versus [O II]λ7325/Hα. Finally, the intensities of the most important line ratios in the NIR ([S III]λ9069,9531/Hα and [O II]λ27325/Hα) are in general agreement with Cohen (1983) who studied a sample of IS. This means that the average optical narrow-line intensity ratios are very similar in IS and Sy2 (Osterbrock et al., 1992).

1.3.3 Optical-UV band (1000-8000Å)

Also in these bands there are two possible techniques to study AGN: spectroscopy and photometry. The most powerful, even if is not the most used, is the first one due to the numerous emissions lines in the AGN spectra. The main producing process is photoionization from the accretion disk towards the NLR and the BLR (Robson, 1996). As a consequence, the spectra can show two types of lines: broad and narrow ones. Both of them are important to measure the physical properties of the emitting region, for example the density and the temperature.

The following is a summary of the findings by Cohen et al. 1983. Studying the luminosity of [Fe VII]6087, Sy1 and Sy2 behave in the same way suggesting that the high-ionization forbidden lines form in the same region as the broad permitted ones. As we will see later, under the luminosity point of view intermediates are more similar to Sy2 rather than Sy1. A consequence can be that the EW of the forbidden lines are greater in IS than in those galaxies in which the narrow component is covered by the broad one. Assuming the same energy input mechanism, some possible explanations for the discrepancy between Sy1 and Sy2 are: 1) the suppression of forbidden lines in Sy1 due to a higher density with respect to type 2s. This will inhibit the collisional excitation. We have two problems with this option. The first is a density greater than 10^6 cm^{-3} in the NLR, which is not the case (as a reference we have $10^2 - 10^3$ cm^{-3}, see Cracco et al. 2016 and Vaona et al. 2012). The second one is that the same mechanism responsible for the lower luminosity in the forbidden lines with respect the broad ones, should act also on narrow permitted lines. As a consequence

whatever mechanisms causes a lower luminosity in the forbidden lines, produces the same effect in the narrow permitted ones, again not confirmed. 2) The difference in the quantity of ionized gas in the forbidden-line region of type 1 AGN than type 2s. The correlation of the line luminosity with the continuum one suggests that the emission is photon limited rather than gas limited. This explains why the difference between the Seyferts is not related to the amount of ionized gas. 3) Most of the ionizing radiation can be blocked by the BLR, where forbidden lines are suppressed by the high density. In this case we would need a coverage factor of 85% for the broad-line gas. This last hypothesis is consistent with other results such as the non-spherical distribution of the NLR and the consequent bi-conical shape for the ionized material.

Concentrating now only on the [O III] emission, sometimes its profile can show asymmetries and irregularities. Their nature is not so clear, but Cohen (1983) underlined the possibility of a photoionization model in which the velocity of the gas decreases with the distance from the center. In this view the side closest to us (the blue one) will undergo less extinction producing a blue wing or a blueshift on high ionization lines. The same if the amount of the material responsible for the obscuration decreases outward. According to other authors, a possible cause for the strange [O III] profile can be the dynamic structure of the torus characterized by inflows and outflows (Hickox & Alexander, 2018). These features can be seen not only in Seyfert 1/2, but also in IS.

From this summary we can understand how complex is "to decode" an AGN spectra. That is to obtain physical information about the parameters (as M_{BH}, T, and ρ) and realize which emitting mechanism is able to produce the peculiar profiles of the lines. The spectral analysis can be divided in steps. We can start from the calculation of the absorbing column where the reference parameter is the Balmer decrement. Its theoretical base is the fixed value for the ratio of the hydrogen emissions coming from different excitation states. If there is an obscuring medium, and so recombination and reddening, we will have a value of optical depth depending on the wavelength which will be different from the reference one. From the comparison between the theoretical and the observed ratios we can obtain the reddening E(B-V) (Cohen,

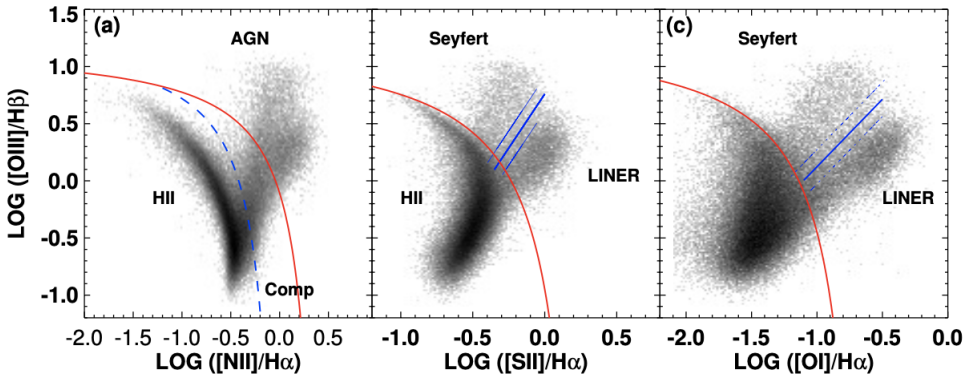

Figure 1.5: Three examples of BTP/VO diagrams that exhibits the difference between AGN, star-forming galaxies (H II), composite systems and LINERs. The figure is from *Hickox & Alexander (2018)*.

1983). For type 2s this reasoning can be easily applied because we have only narrow lines, but it is not so straightforward on intermediates. Assuming that the narrow component of IS behave as the Sy2 ones, we can use the Balmer decrement as in the latter class, but this is not so obvious. Sy1.8/1.9 are more suitable due to the faintness of the broad component, while Sy1.2/1.5 deviate more from the Sy2 case. The reference equation is (Trippe et al., 2010):

$$E(B-V) = \frac{2.5}{R_{H\alpha} - R_{H\beta}} \cdot log \frac{2.9}{\frac{f_{H\alpha}}{f_{H\beta}}} \tag{1.2}$$

With $f^{NLR}_{H\alpha}/f^{NLR}_{H\beta} = 2.9$ from the Case B recombination value, $R_{H\alpha}$ and $R_{H\beta}$ related to the standard Galactic reddening curve $R(\lambda)$. If it is not possible to distinguish the broad component of Hα (Sy1.9) one can put only a lower limit to the reddening. Another problematic feature is the presence of iron multiplets which tend to mix with other lines. In particular these emissions probably form a small blue bump in the near UV. As a matter of fact it is not so simple to distinguish between all the single Fe lines due to different obstacles: the huge number of lines, the broadening and the consequent blending, and the absence of an accurate model for the iron atom (Järvelä et al., 2020).

The spectral analysis can continue with the study of line ratios, which are used to measure T, ρ, and the ionization degree (U) in the NLR. This last one gives information about the ionization level defined as the ratio between the flux of ionizing

photons and the hydrogen density. It is a measure of the amount of ionization that a radiation field can drive as it moves through the nebula. Combining line ratios we can build diagnostic diagrams fundamental in the classification. In particular some reference plots are BPT and VO diagrams, see Figure 1.5 for an example. Seyfert galaxies are those objects showing high ionization levels and large partially-ionized regions (Hickox & Alexander, 2018).

Another interesting parameter is the black hole mass, which can be obtained using the the virial theorem:

$$M_{BH} = f_{BLR} \cdot \frac{R_{BLR} \cdot \Delta v^2}{G} \tag{1.3}$$

Where R_{BLR} is the radius of the broad-line region, Δv the velocity dispersion from a broad emission line width (often $H\beta$), and f_{BLR} is an inclination dependent factor which takes into account projection effects. Obviously other methods can be applied, some examples are: reverberation mapping, spectropolarimetry, SED modelling, host galaxy-BH scaling relations, and so on (Komossa, 2018).

Spectropolarimetry played and plays a significant role in understanding the Seyfert world. In Seyfert 2 once the [O III]λ5007/Hβ ratio is obtained, one can predict fairly accurately the relative intensities of the other stronger lines. These correlations were discovered by Koski (1978). In this work a sample of Sy2 was studied through the forementioned technique and as a result they obtained some relations between the lines. In particular, they proposed the presence of two independent ionization zones in these AGN: one of high ionization which includes He^{++}, O^{++}, Ne^{++}, Ne^{+4}, Ar^{++}, and probably Fe^{+6}, and one of low ionization which includes N^0, N^+, O^0, O^+, and S^+. The cutoff between the two regions is around [O III]λ5007/Hβ=10. This is not the same for IS, indeed the distribution differs from the Sy2 one with a range of 2.56-13.2. Furthermore, form polarization it is demonstrated that forbidden lines and Hβ_n are formed in the same region for a sample of Sy1.5. Instead, they have different properties for Sy2 (Cohen, 1983). On the other hand, as anticipated in the classification chapter, under the polarimetric point of view Sy1 and Sy2 present similar characteristics. This is attributed to a "mirror" component which reflects the radiation coming from the nuclei revealing an almost identical radiation for the two classes, and the same is true for IS (Antonucci, 1993; Hickox & Alexander, 2018).

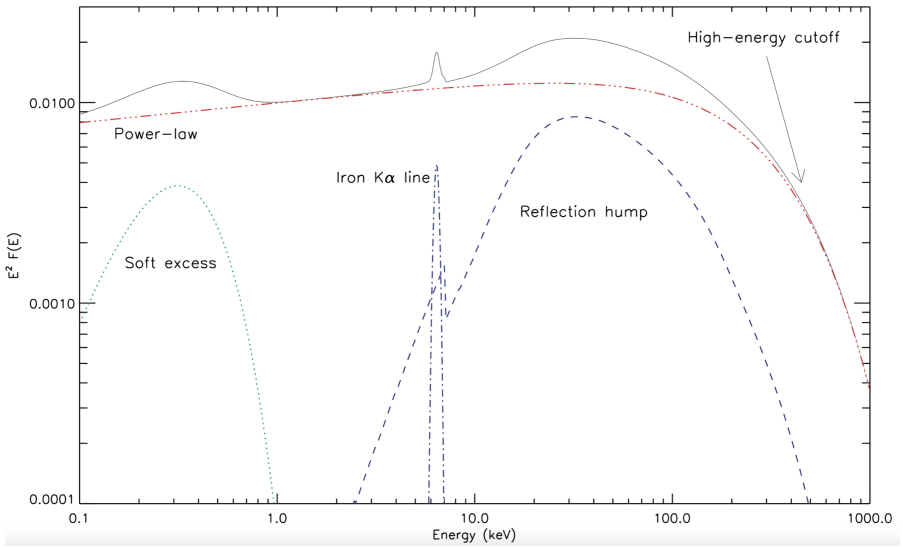

Figure 1.6: The X-rays spectra of an AGN. In this plot we can see all the different components: the power-law trend, the soft excess, the iron line and the reflection hump. Other two interesting features are the high energy and the low energy cutoffs. In particular, the second one is due to galactic absorption. The figure is from *Ricci et al. (2011), PhD thesis*.

Another proof of this relation between the classes comes from the luminosity. Under this point of view, IS are more similar to Sy2 rather than Sy1. But if we compare Hβ in its broad and narrow components to [O III]λ5007, intermediates and Seyfert 1s are analogs (Cohen, 1983). This make IS a bridge between the types.
In section 1.2.4 we presented the possible evolutionary scenario of CL sources. The intermediates were again interpreted as a link between the main classes. Cohen, many years before, in 1983 stressed the difficulty in demonstrating this point due to incompleteness of the samples for all the Seyfert types. This is a further evidence of how works focused only on IS are needed, not only for the intermediates itselves, but for the entire AGN family.

1.3.4 X-ray band (0.2-200 keV)

Again spectroscopy is one of the main techniques employed in the AGN characterization. X-rays observations represent indeed one of the most complete methods for this purpose. In general, this band is divided in soft X-rays with E$<$1 keV, and hard X-rays above this value. This radiation comes from the accretion disk and its corona. The competitor host-galaxy processes for the X-rays emission are the formation of

very massive stars, which are not so common, and an strong Star Formation Rate (SFR) (Hickox & Alexander, 2018).

The high energy spectrum can be fitted with different models. The most used are a single PL with galactic absorption, a single PL with a modulated absorption, and a double PL where the second one is attributed to the reflected component. This last one refers to the radiation emitted by the corona towards the disk and then reflected along the direction of the observer (Trippe et al., 2010). In general, the PL spectrum comes from: the inner part of the disk, the corona localized above the accreting area, or the jets if present. The most relevant emitting mechanism for the X-rays is inverse Compton (IC) due to the reflected nature of this radiation (Robson 1996). Observationally some authors noted that increasing the Seyfert type, also the adopted model becomes more complex, in particular under the absorption point of view. We can deduce that Sy2 are more obscured than IS (Hernandez-Garcia et al., 2017).

Another interesting feature is the soft excess, which is probably generated by the merging of unresolved emission lines coming from a region of photoionized gas (Trippe et al., 2010). In reality its nature is not so clearly understood. Sometimes in these spectra we can find the irregular and broad Fe Kα line at 6.4 keV. It can show asymmetries or broadening, signs of its probable relativistic origin (Järvelä et al., 2020). The idea is that the accretion disk in its inner regions is very dense and undergo relativistic effects due to the BH proximity, which in turn produces the uneven aspect of the iron line. Some objects shows features also at 5-6 keV coming from a complex emitting zone formed by flares and hotspots (Piconcelli et al., 2006). An example of the high energy spectra is shown in Figure 1.6.

An interesting relation holds for unobscured AGN, which links the X-ray and the UV-optical emissions. This can be interpreted as the manifestation of an intrinsic physical relation between the disk, emitting the primary radiation, and the hot electron corona emitting X–rays (Lusso & Risaliti, 2016; Hickox & Alexander, 2018). Another perspective comes from the Guolo et al. (2021) detailed study of NGC 2992, a CL AGN. In this case the high hard-X luminosity ($L_{2-10keV} > 10^{42}$ erg s^{-1}) correlates with the optical detection (or non-detection) of the Hα broad component.

This in turn is related to the changing of the source between the Seyfert types.

1.3.5 γ-ray band (100 MeV-10 TeV)

In general, above 10 keV the spectrum tends to flatten out. As in the X-rays, the principal emission mechanism is IC (Robson, 1996). Seyfert galaxies are not so bright in this band and the vast majority of the γ emitting AGN are blazars, so objects viewed directly along the jets. Associated to this family of AGN we can find the so-called parent population. This is formed by the classical double-lobed radio galaxies, which represent the radio counterpart of the X/γ-ray jetted emission (Landt et al., 2016). Referring to Figure 1.1, the second bump in the the SED related to the gamma range corresponds to the relativistic jet emission. This electron flow can show substructures as blobs which evolve and produce flares. In general, most powerful jets are associated to the most massive BH, of the order $M_{BH} > 10^8$ $M_\odot$. This is the reason why blazars tend to be found in elliptical galaxies (Järvelä, 2018). Soft γ-ray emission has been detected from a few nearby Seyfert galaxies, though it is not clear whether those gamma-rays originate from the nucleus. In any case they represent less than 2% of the total AGN number producing very high energy photons. The detection of γ radiation from Seyferts challenges the scenario in which radio-loud AGN are hosted by elliptical galaxies as a consequence of merging events (Dermer & Giebels, 2016).

1.3.6 Summary

It is quite evident that IS are an ambiguous class of objects of which we ignore a lot of properties. In general multiwavelength observations are crucial in obtaining a complete sample, but are not so easily achievable. Before changing topic, is useful to summarize some interesting parameters for the different Seyfert types, reported in Table 1.1. As we can finally see, all these quantities corroborate the UM demonstrating an increasing viewing angle and extinction from Sy1 to Sy1.9, but a decreasing disk luminosity through the same path. Probably both the intrinsic and the extrinsic hypothesis for the differences between the Seyfert types are valid.

	Sy1	**Sy1.2**	**Sy1.5**	**Sy1.8**	**Sy1.9**
Viewing angle i	25°	25°	25°	45°	45°
Disk luminosity L_{AGN}^{disk}	$>10^{10}L_{\odot}$	$>10^{10}L_{\odot}$	$=10^{10}L_{\odot}$	$<10^{10}L_{\odot}$	$<10^{10}L_{\odot}$
Extincion $E(B-V)$	0	0	0.1-0.3	0.4	0.4

Table 1.1: Summary of the information about Intermediate Seyfert galaxies. These parameters comes from *Ramos-Padilla et al. (2021)*.

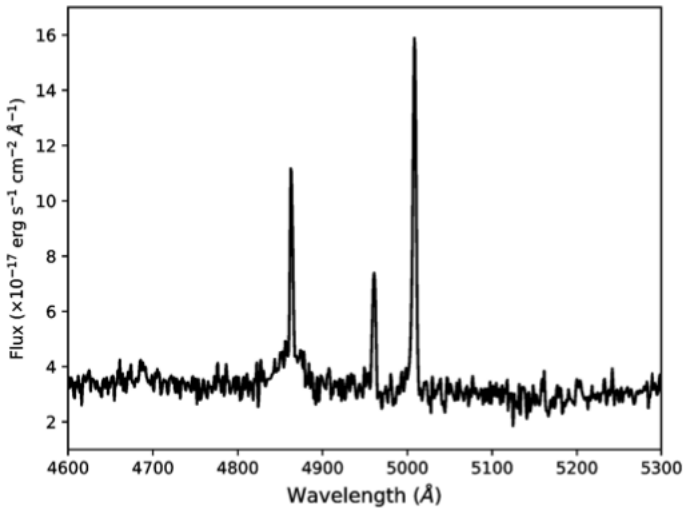

Figure 1.7: A clear example of wrong classification. This object was interpreted as a NLS1 due to the listed qualities, but in reality is an intermediate Seyfert galaxy. This can be inferred from the presence of both the narrow and the broad components of the Balmer line. The figure is from *Berton et al. (2020)*.

1.4 NLS1

Another interesting class of AGN is formed by NLS1. Optically they are selected using parameters as the presence of narrow Balmer lines, strong Fe II emission and low [O III]/Hβ ratios. Additionally the oxygen line can be very asymmetric, similarly to the C IV emission, showing blueshifts. Other two significant quantities are: C IV/Lyα and [S II]$\lambda\lambda$6716/6731. In NLS1 samples, the former tends to be small, while the latter to be high. These values agrees with the density values typical of BLR and NLR. The calculated M_{BH} seem to be systematically lower with respect to Broad-Line Seyfert 1 (BLS1), the classical Sy1 when compared to NLS1. A second connected parameter is the accretion rate, in turn related to the Eddington ratio L_{bol}/L_{Edd}. Under this point of view NLS1 tend to accrete close to the Eddington limit and sometime above it (Komossa, 2007).

In any case the focus needs to be on the similarities between this kind of sources and intermediates. Both are selected using the same lines and line ratios which not always are so well defined. In Figure 1.7 we have a clear example of how these listed characteristics are not so precise in classifying AGN. This is a case in which a IS was considered a NLS1. This would not be a problem if these two classes show analogue physical properties. On the contrary, if IS are clearly different from NLS1s then the intermediates can pollute the conclusions. The aim of the following work is to understand if IS represent a separate group of AGN, or can be included in the Sy1/Sy2 samples without the doubt of obtaining contaminated results.

Chapter 2

Sample and data analysis

2.1 Selection

The initial sample was formed by 1984 spectra, in which we can find a heterogeneous group of AGN. They were selected by Cracco et al. (2016). The spectra used for this work come from the Sloan Digital Sky Survey DR7 (SDSS-DR7). The first approach was based on a visual inspection to separate the objects through the S/N ratio. All those spectra in which the main features, such as Hα or [O III]$\lambda\lambda$4959,5007, were not distinguishable from the noise were rejected. From this preliminary selection the sample has been reduced to 1475 sources. The second criterion consisted in the flux difference between Hα and the continuum at 5100 Å. All those galaxies with a $F_{H\alpha} - F_{5100} > 250$ were accepted. The flux level was selected in a tentative way increasing the value from 100 to 250 to get a number of objects in between 50<N<100. With this screening 89 sources were obtained. The third step involved a new visual inspection with the aim of choosing the final 50 galaxies. In this case the discriminant was the Seyfert type. The final goal was obtaining a diverse sample in terms of this characteristic. Comparing the fluxes of [O III]λ5007 and Hβ, Whittle (1992) provided a selection method that is explained in section 1.2.2. Unfortunately this ratio can be exploited only in a second moment, during the data analysis. In any case the initial purpose was achieved getting 24 Sy1.5 and 23 Sy1.8. It is important to stress the

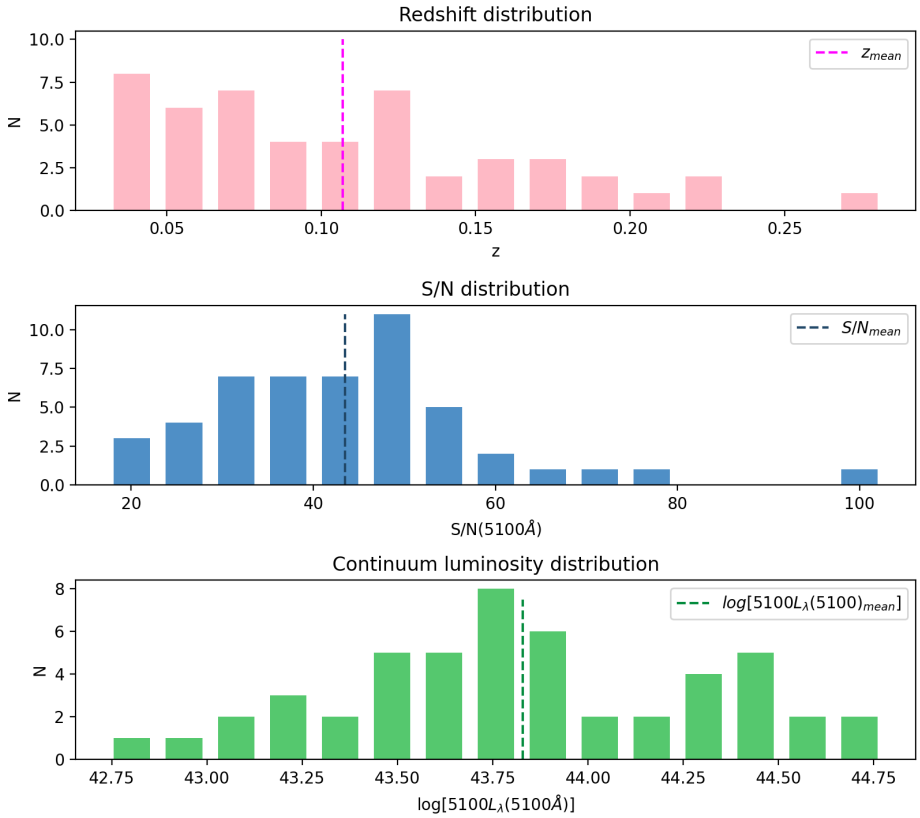

Figure 2.1: Distributions of the redshift (top), S/N ratio of the continuum at 5100Å (middle) and the luminosity of the continuum always at 5100Å (bottom).

lack of type 1.2 (only three AGN) and 1.9 (no objects) in this sorting. Obviously this separation needs to be confirmed because the classification was operated in an tentative way, as it will be described later.

2.2 Characteristics

The final sample is formed by 50 sources. In this group of objects we can find mainly IS and one Sy1, see the table in the Appendix for the entire list. The redshift ranges between $0.03 \leq z \leq 0.28$ with a mean value of ~ 0.11 (top panel of Figure 2.1). This implies that all the spectra present the major optical emission lines ([O II]λ3727, Hβ, [O III]$\lambda\lambda$4959,5007, [O I]λ6300, Hα, [N II]$\lambda\lambda$6548,6583, and [S II]$\lambda\lambda$6716,6731) within 3700 Å and ∼7500-8950 Å.

These spectra are characterized by high S/N ratios to distinguish among the classes (see section 1.4). The mean value for them is ∼43 (middle panel of Figure 2.1). In

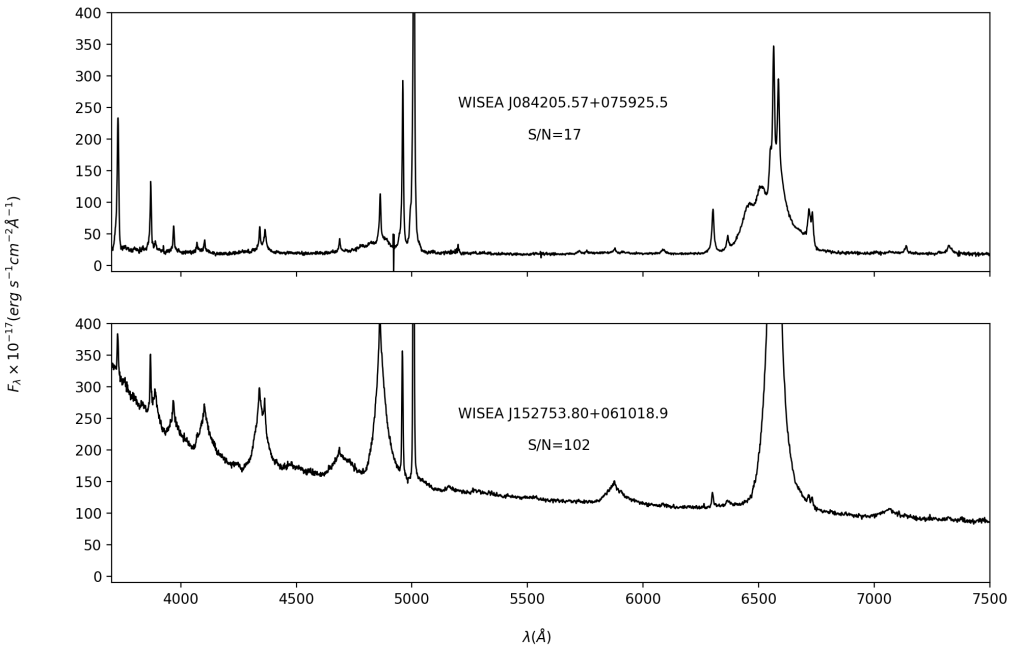

Figure 2.2: Comparison between two spectra, one with the lowest signal to noise ratio in the sample (top) and the other with the highest one (bottom).

Figure 2.2 it is presented a comparison between sources with different S/N ratios from the selection. In both cases all the lines and the features are clear distinguishable from the noise. This is really useful in fitting properly the emissions.
Another important characteristic is the continuum luminosity at 5100 Å. For the NLS1 galaxies we have a reference value of $10^{42} - 10^{44.5}$ erg s^{-1} (Chen et al., 2018). In this IS sample the distribution ranges between $10^{41} - 10^{44.5}$ erg s^{-1}, as we can see from the bottom panel in Figure 2.1. This can be explained in terms of the UM. In Sy1 the observer can see the central part of the AGN, while in the intermediates this luminosity is partially blocked by the BLR.

2.3 Fitting

Some corrections to the spectra were applied before to proceed with the analysis. The main steps consisted on: the galaxy de-reddening exploiting the V-band extinction values from NED and the rest frame wavelength shifting. All these passages were carried out by means of *IRAF*. The adopted cosmology is $H_0 = 70$ km s^{-1} Mpc^{-1},

$\Omega_M = 0.3$, and $\Omega_\Lambda = 0.7$.

2.3.1 Lines and constrains

A specific code for each object was created to fit properly all the features present in the main spectral lines. The reference program in this case is *Python 3.0* instead of *IRAF*. The studied spectral lines were: e.g. [O II]λ3727, Hγ, [O III]λ4363, Hβ, [O III]λ4959, [O III]λ5007, [O I]λ6300, [S III]λ6312, Hα, [N II]λ6548, [N II]λ6583, [S II]λ6716 and [S II]λ6731. These lines were chosen due to their prominence, or because they can be used to calculate properties such as the temperature and the density of the NLR.

Each line was fitted with one or a combination of multiple Gaussian profiles. The output parameters were the center of the curve (x_0), its amplitude (A), and the dispersion (σ). This kind of model was selected due to the ability in representing the gas distribution of the emitting source. In some cases a Lorentzian profile was more suitable for the broad components, but this can be reproduced anyway with two Gaussians with the same center. The residuals and the χ^2_{red} were exploited to compare the results. In those cases in which three Gaussians were not sufficient for the fit, an extra curve was added if it improves the χ^2_{red} moving its value toward 1.

In the procedure the first step consists in finding a reasonable function for the continuum. Linked to this problem we have the wavelength range identified for the spectral feature. For all the lines this was done through visual inspection looking for those points in which the emission mixes with the noise, except in some cases for [O III]λ4959. This line is extremely close to the Hβ profile which in turn can present very broad wings. In those situations, the continuum has been considered not to start from the valley between the oxygen and the Balmer line, but from the region before the hydrogen feature around 4750 Å.

The fitting proceeds with the prominent emissions, in particular Hβ and [O III] lines at 4959 and 5007 Å. The reason for using the first approach to the second Balmer line, instead of Hα, is the presence of nitrogen lines. These emissions mix to the Hα profile which globally forms complicated structures to study. From Hβ we can infer some properties to employ in the Hα+[N II] profile fitting which will be more

	[O II] λ3727	Hγ λ4340	[O III] λ4363	Hβ λ4861	[O III] λ4959	[O III] λ5007	[O I] λ6300	[S III] λ6312	[N II] λ6548	Hα λ6563	[N II] λ6583	[S II] λ6716	[S II] λ6731
1	46	2	41	-	13	13	50	30	50	-	48	50	50
2	4	34	9	7	35	35	-	-	5	7	2	-	-
3	-	13	-	28	2	2	-	-	-	28	-	-	-
4	-	1	-	10	-	-	-	-	-	9	-	-	-
5	-	-	-	5	-	-	-	-	-	6	-	-	-

Table 2.1: In the first raw we have all the fitted lines, while in the first column the number of Gaussians used for each line. As a consequence, in the boxes are listed the number of objects in which the spectral features are reproduced by a specific number of Gaussian profiles.

constrained. Some of them are the position with respect the rest frame λ and the width of the components w. The same for [O III]$\lambda\lambda$4959,5007, these two oxygen lines are linked by a transition probability of 3 (NIST) which will be the ratio between the two intensities. As before, the difference in wavelength among the fitted curve (or curves) and the rest frame, together with the width of the adopted Gaussian (or Gaussians), should be the same in [O III]λ4959 and [O III]λ5007. Also for [N II]$\lambda\lambda$6548,6583 there are similar relations: the transition probability in this case is 2.96 (NIST), added to the center and the width constrains. For [S II] we have only the last two conditions, which in any case are sufficient for these simple emissions. Summarizing there is a list of possible constrains to exploit in the fitting procedure. The reason is to leave as few free parameters as possible. The main of them are the relations between x_0 and σ of the same components of connected lines (for example narrow$_{H\beta}$ and narrow$_{H\alpha}$), but also transition probabilities.

Table 2.1 presents the number of Gaussians used for each line in the fitting. Focusing on the Balmer lines, we can see that more than half of the profiles were reproduced with three functions identifying one narrow component and two broad ones. This is again related to the fact that the two largest functions can be replaced by a single Lorentzian. Particularly for those cases in which these two Gaussians have compatible centers. Some interesting spectra needed more than 3 components. In these situations the emission is more complex and presents multiple bumps. For the oxygen lines one or two Gaussians were sufficient, except for two objects. In this case we can divide between the core NLR emission and the outflows. Hγ is linked to the other hydrogen lines. Generally speaking it needs less components due to its faintness and the fact that the broad emissions tend to mix easily with the noise.

The same for the near [O III]λ4363 line which is related to the oxygen doublet at 4959 and 5007 Å, but it is fainter. In general, all the other profiles are reproduced by single curves except in specific cases where a broad component could not be ignored. Finally, [S III] was fitted only for 30 sources. This line is very faint in almost all the cases, but sometimes it is blended with [O I]λ6300. In these situations the sulfur line was considered in order to get an improved fit for the close [O I] profile.

2.3.2 Invalid constrains

Let us spend some other words about the fit of Hα+[N II] complex. As we said previously, there are some constrains that we can exploit to limit the number of free parameters and obtain a controlled result. Despite this possibility, some objects do not respect these criteria. Starting from the relation between the center of the broad components of Hα and Hβ we have a displacement to the rest frame wavelength ($\Delta_{line} = |\lambda^0_{line} - \lambda^{fit}_{line}|$) for the first Balmer line in between 0.12 Å $< \Delta_{H\alpha} <$12.19 Å, while in the second one is 0.13 Å $< \Delta_{H\beta} <$8.13 Å. The mean values are of 3.13 Å and 5.41 Å respectively. As we can see the two ranges do not coincide. This is due to the fact that for these sources the central parameter was let free to vary to obtain an improved fit. Indeed if the constrain was maintained, the result was not as good as in the other situation. Even if the discrepancy seems to be not so big, when we compare the two deltas ($\Delta_{H\alpha} - \Delta_{H\beta}$) we have a maximum difference of 4.95 Å and a minimum one of 1.68 Å. Converting the calculated gaps in terms of velocities, this means a difference of 10^2 km s^{-1} as order of magnitude, which is not really negligible.

In some other sources $\sigma_{H\alpha}$ was not forced to be the same as in Hβ. They are only three cases. The first one is not so significant due to a difference between the two widths of only 0.64 Å. But in the other two situations we have values around 19.40 Å and 20.47 Å. These gaps are between the largest component of Hα and Hβ (indicated as Hα_{b1} and Hβ_{b1}), see Figure 2.3. This is not easily explainable, but we can hypothesize that the differences are related to a not perfect fit of the Hβ profile. In this case Hβ is not completely able to reproduce all the Hα features. Another possibility is that the Gaussian model is not the most suitable, so we need a more

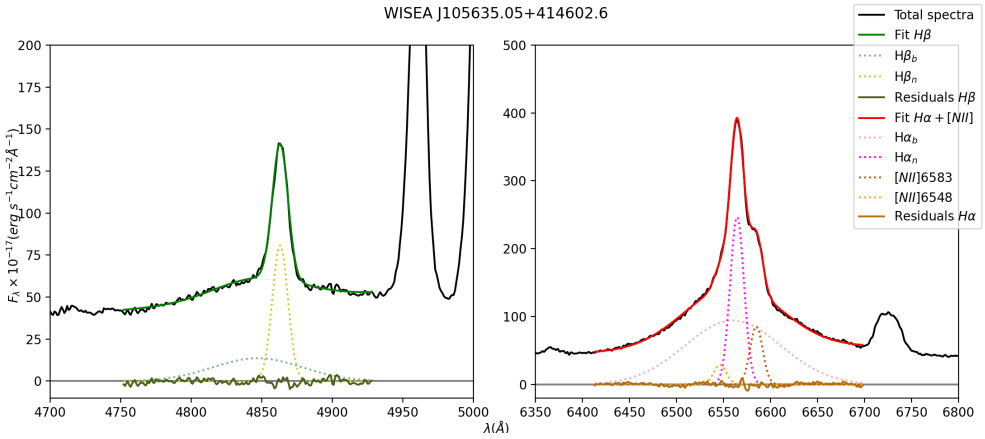

(a)

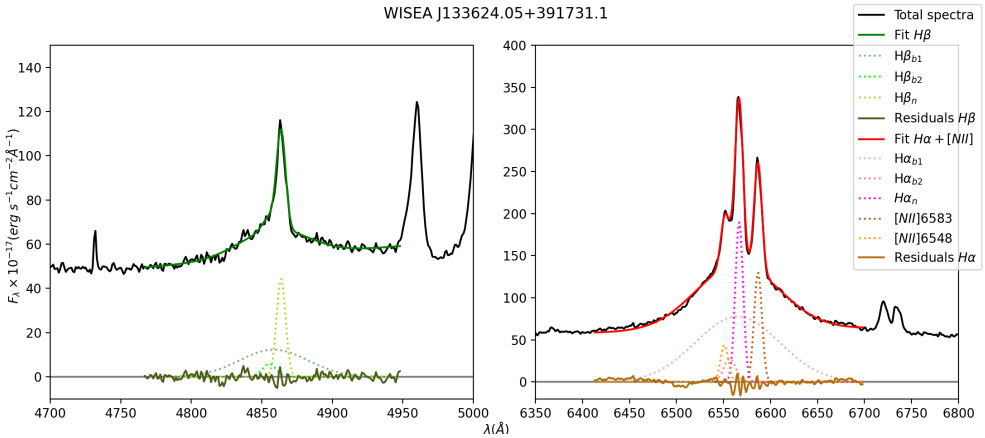

(b)

Figure 2.3: Hβ and Hα fits indicated in green and red respectively. The two selected sources are those in which the width of the broad components in the first Balmer line are not related to the other one. In particular, (a) represent *WISEA J105635.05+414602.6* and (b) *WISEA J133624.05+391731.1*. As always, the dotted curves indicates the single components.

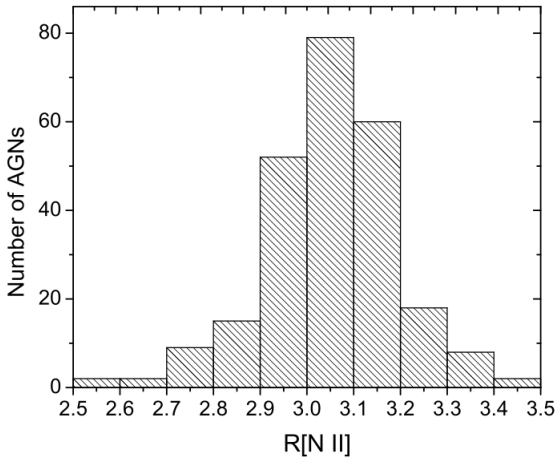

Figure 2.4: Transition probability range for the ratio between [N II]λ6583 and [N II]λ6548 versus the number of objects in the selected AGN sample. The plot is from *Dojčinović et al. (2022)*.

complex one. Anyway, the BLR emission should be the same between the Balmer lines. These bumps are produced by the same gas in the AGN, so there should be a correspondence.

Finally we can treat the nitrogen lines. In some spectra the transition probability relation is not respected, they are four cases. In one of them the intensity ratio cannot be calculated due to the fact that the fainter line, the one at 6548 Å, is not detected. The others show ratios as 2.08, 5.01, and 6.13. These numbers are clearly different from the reference value of 2.96. Other literature values are in the ranges 2.93-3.07 or 2.52-3.69 depending on the AGN type and on the observing technique. In any case these are different from what we obtained, see Figure 2.4 for the results of Dojčinović et al. (2022). The role of the noise in [N II] intensity measurements is important, particularly for [N II]λ6548. Even a small difference in the continuum level and in the slope due to noise could affect the measured line intensities. In turn this affects strongly the value of the nitrogen lines ratio. Dojčinović and others obtained a final transition probability around 3.05, considering also relativistic corrections and the magnetic pole operator. Unfortunately, this value does not fit with our examples. One possibility could be a bad fit of the Hα profile and the corresponding lack of components. Another one is the presence of broad emissions related to nitrogen which will contribute to the ratio, but in our cases are not detected. Indeed the fits seem to reproduce quite well the spectra and so this hypothesis should not be

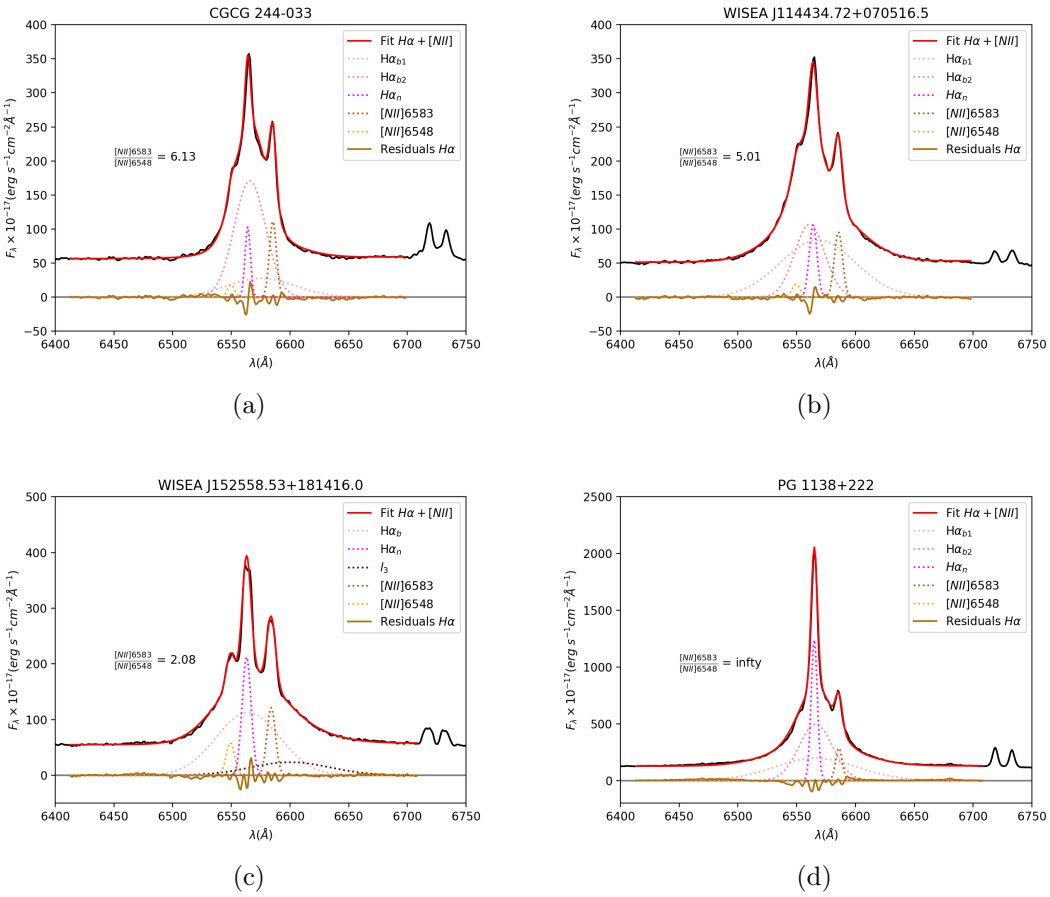

Figure 2.5: The Hα region of those objects which shows a different nitrogen intensity ratio with respect the NIST value of 2.96. Following the order we have: (a) *CGCG 244-033* with 6.13, (b) *WISEA J114434.72+070516.5* with 5.01, (c) *WISEA J152558.53+181416.0* with 2.08 and (d) *PG 1138+222* with the fainter line absent, and so a ratio that tends to infinity.

correct. The last solution could be a more complex model required to fit properly Hα. This case contemplates the presence of bumps under the [N II] doublet which will explain these ratios, see Figure 2.5 for a comparison. The only ambiguous case is the last one (d) where maybe a faint line is present around 6550 Å but the fitting program was not able to recognize it even if putted manually. Finally we can say that the blending between the nitrogen features and the hydrogen one makes the interpretation difficult.

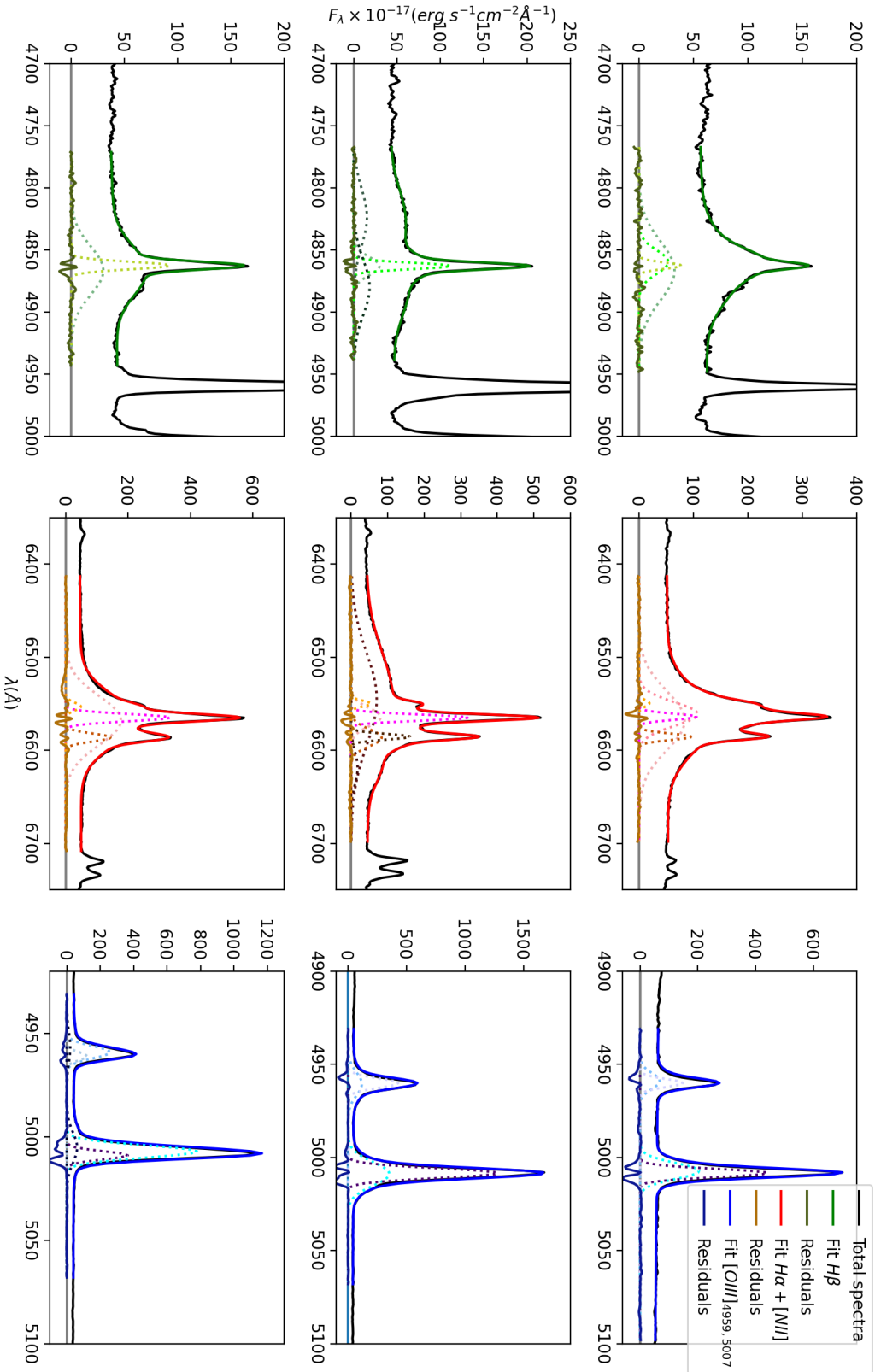

Figure 2.6: Some fit examples, from the first row the selected objects are: *WISEA J114434.72+070516.5*, *WISEA J211646.34+110237.4* and *WISEA J134915.20+220032.6*. The three columns corresponds to Hβ in green, Hα in red and [O III] in blue. In each plot there are some dotted curves which symbolize the single components of the whole fit.

2.3.3 Normal and pathological spectra

In Figure 2.6 some fit examples are presented for typical and atypical cases. Starting from the first row we have Hβ, Hα, and [O III]$\lambda\lambda$4959,5007 for a classical case in this sample. Here the Balmer lines are reproduced by three components (narrow in olive green, broad$_1$ in neon green and broad$_2$ in sage green, the same for the other hydrogen line, but in red), [N II] by one Gaussian for each feature (orange and dark orange), and finally the oxygen lines with two curves each (narrow in violet and broad in cyan, the same but with different colors for [O III]λ4959). In the second row an atypical case in which Hβ and Hα are fitted with four Gaussians, probably linked to a disk structure of the BLR. Here [N II] presents one curve for the faint line at 6548 Å and two for the 6583 Å one. [O III] is analogue to the previous case. In the last row it is important to stress the third component needed for the oxygen lines fit.

As we can see from this brief comparison, all these spectra present multiple characteristics and so are difficult to classify. One possible separation is the presence (or not) of peculiar components in the fit such as a number of Gaussians greater than 3 in the Hβ profile. Using the described method, the objects were divided in two classes: "normal" profiles and "pathological" profiles. In general, the average variation of the broad components between $\lambda^{fit}_{H\beta}$ and $\lambda^{0}_{H\beta}$ is $\sim$8.5Å. If we divide the sample as before, we have a mean value of $\sim$3.5Å in the "normal" objects, while $\sim$13.3Å in the "pathological" ones. This is due to those extra components added for the BLR emissions fit represented in dark green (Hβ) and dark red (Hα) in the central row of Figure 2.6. These features can be a couple of curves, in a sort of Keplerian disk emission, or single profiles with a very different center with respect to the others. In this last case, if we mix the broad features we could use skewed Gaussian models instead of simple ones.

2.3.4 Asymmetries

About the asymmetries in the Hβ profiles we can summarize the results in this way: half of the broad components are shifted towards the blue part of the spectra

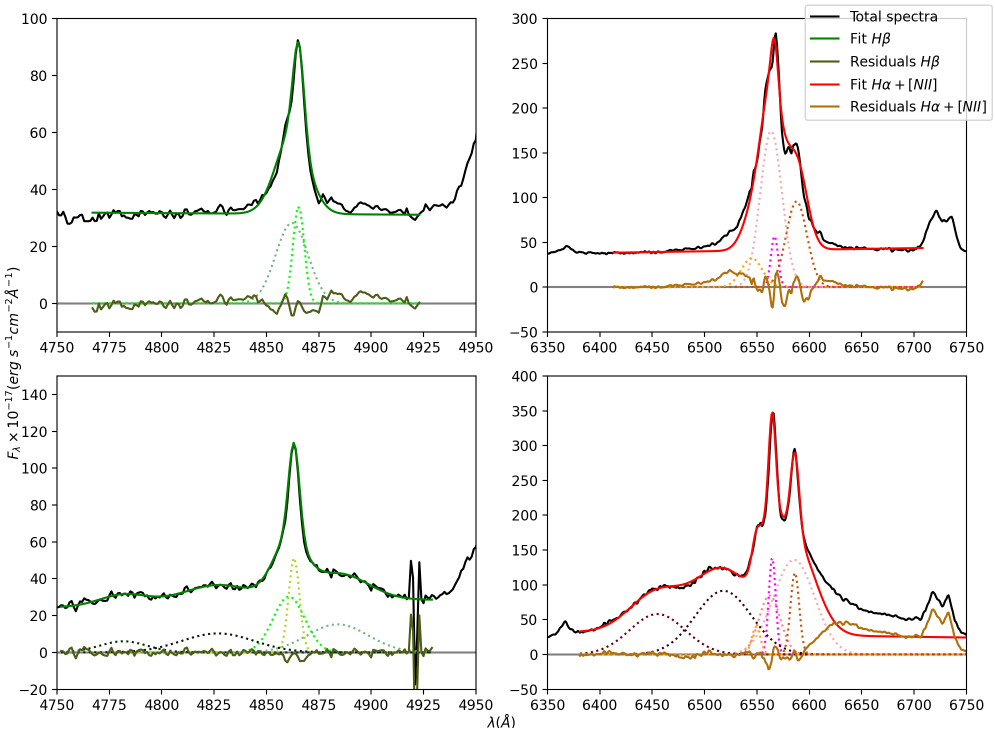

Figure 2.7: Two bad fits which cannot reproduce properly all the spectral features of Hβ, Hα, or both. In the first row we have *WISEA J164819.02+302210.8*, while in the second one *WISEA J084205.57+075925.5*. Again the red and green solid lines are the fits, the dotted Gaussians all the single components, and the black line the initial spectra.

with respect the narrow peak, a not negligible part of the sample (11 sources) have redshifted features, while 14 AGN have almost symmetric profiles. In this last group we can divide the real symmetric profiles (8 cases) where $H\beta$ is fitted with two Gaussians with approximately the same center. The other family (6 objects) is represented by those profiles with two extra curves which generates "symmetric asymmetries" around the center. Another important thing to say is that some displacements, and so blue/redshifts, are really small. In the symmetric cases we have an equal division between normal and pathological fits. For these fits we can replace the double Gaussian profile, needed for the BLR emission, with a Lorentzian one. Instead, the NLR component is always represented by a single Gaussian.
Considering the BLR emission in the Hβ profile, we have a general trend which consists in a global shift of the line towards the blue part of the spectra.

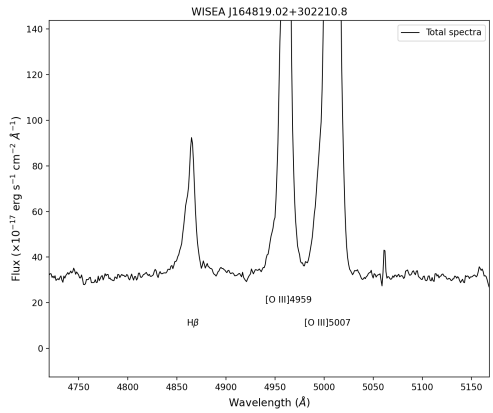

(a)

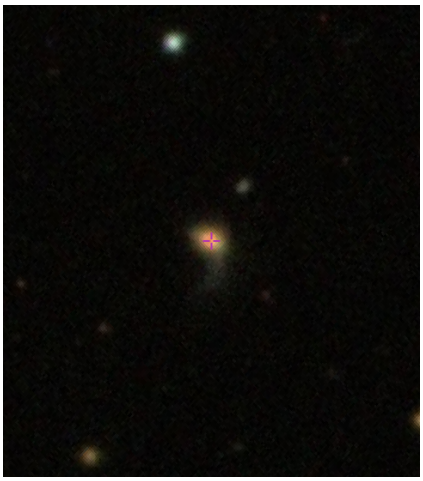

(b)

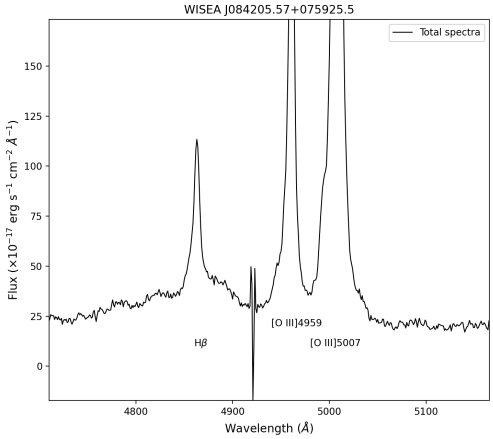

(c)

(d)

Figure 2.8: (a) and (c) Hβ−[O III]$\lambda\lambda$4959,5007 region of *WISEA J164819.02+302210.8* and *WISEA J084205.57+075925.5*. (b) and (d) SDSS9 color images of the same sources with a FoV of 1.3', from http://cdsportal.u-strasbg.fr/?target=LEDA%203095819 where other bands images and surveys could be found.

2.3.5 Bad fits

It is important to stress that some fits were not so good in reproducing the Balmer lines. Particularly in two cases: *WISEA J164819.02+302210.8* and *WISEA J084205.57+075925.5*. As we can see from Figure 2.7 the former (first row) is quite well reproduced in its Hβ emission, while Hα presents some problems especially in the wings, but also in the nitrogen lines. In Figure 2.8 panels (a) and (b) refers to this AGN. The SDSS image does seem to show some possible signs of interaction, perhaps in the form of a tidal tail. This could explain the strange shape of the lines and the broad [N II] emissions. This does not mean that the nitrogen feature comes from the BLR, but it can be the consequence of a cinematic effect. In this case different components of the NLR overlaps and produce a line that appears broad.
In the second row of Figure 2.7, the other profile is again well fitted by the green line, both in the peak and the wings. On the contrary, Hα is underestimated on the right side showing a smoother decrement with respect to the red curve. In particular, in this last spectrum the problems could be three: the bad signal feature around 4925 Å, the proximity of [O III]λ4959, or a possible gas perturbation. In the second case the long wing visible in the Hα profile can be hidden under the oxygen lines at 4959 and 5007 Å and so not easily reproducible starting from the other Balmer emission, as we can see from the bottom-left panel of Figure 2.8. For the third possibility we need the SDSS image of *WISEA J084205.57+075925.5*, which is visible in the bottom-right panel of the same figure. The gas perturbation can be the consequence of a jetted emission, the radiation pressure from the disk, or an interaction. Jarvis M. E. et al. (2021) presented some radio properties of this source. In the supplement, they suggested that this can be a barely resolved lobe-core-lobe structure, possibly related to radio-jets. As a consequence this can be the reason for the observed strange profile.

2.4 Velocity diagrams

A possible way to compare the Balmer lines and the [O III]λ5007 profiles is creating velocity diagrams in which the x-axis represents the velocity of the emitting clouds

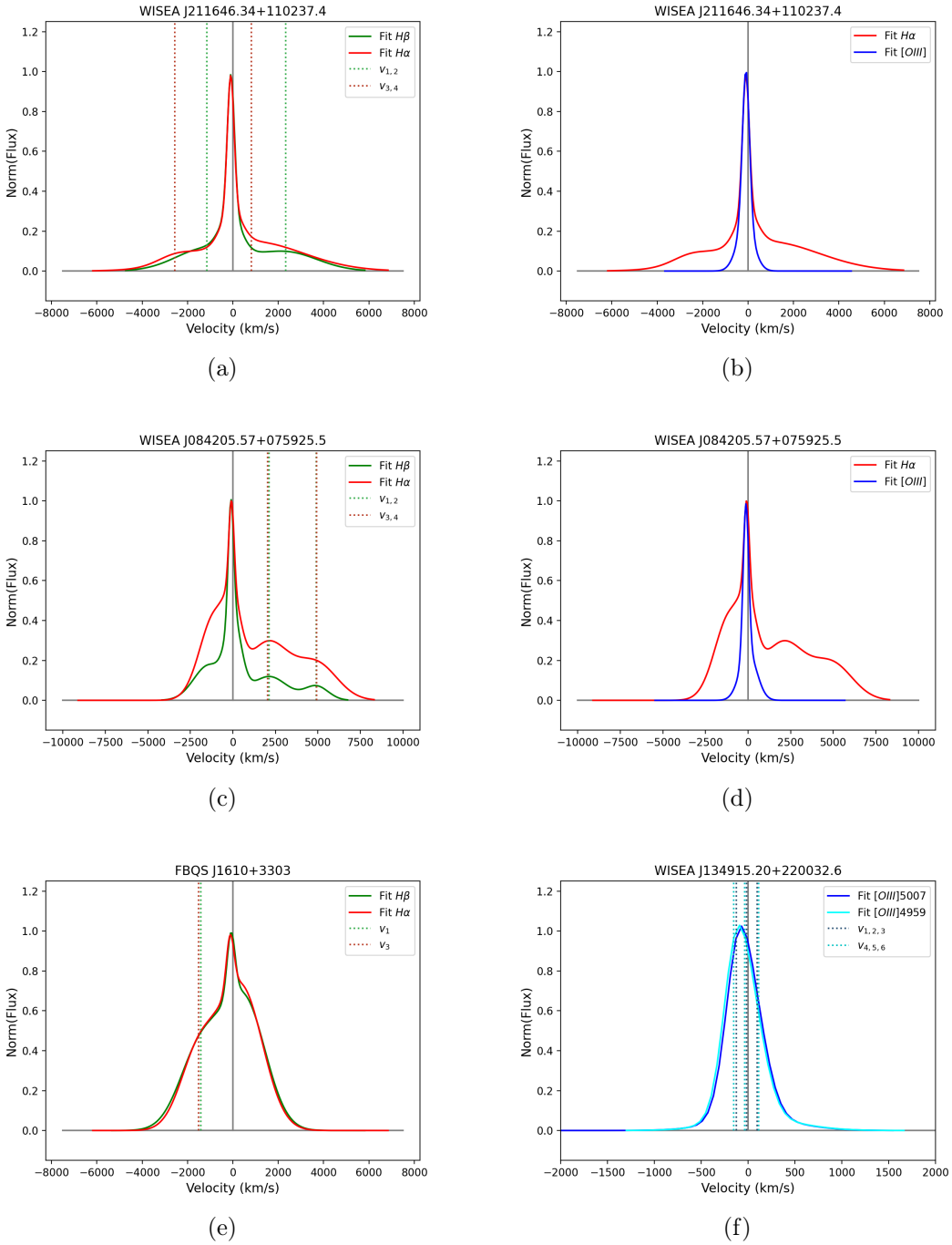

Figure 2.9: Following the panel sequence we have: the comparison between Hα−Hβ in red and green, Hα−[O III]λ5007 in red and blue, and [O III]λ5007−[O III]λ4959 in blue and cyan. The selected objects are (a) and (b) *WISEA J211646.34+110237.4*, (c) and (d) *WISEA J084205.57+075925.5*, (e) *FBQS J1610+3303* and (f) *WISEA J134915.20+220032.6*.

for each component (NLR and BLR) and the y-axis the normalized flux. The idea is to understand if in those "pathological" objects the extra Gaussians in Hα, Hβ and [O III] are related, or if they are peculiar characteristics. As a consequence, this procedure was applied only to the atypical sources. To convert the wavelength into a velocity we need the following relation:

$$v = \left(1 - \frac{\lambda_1}{\lambda_2}\right) \cdot c \tag{2.1}$$

Where λ_1 is the wavelength of the selected line (for example Hβ), λ_2 is the one of the compared line (in general Hα) and c the speed of light. Another important step is to scale the peaks of the selected lines to normalize them:

$$R = \frac{1}{F_{line}} \tag{2.2}$$

Where F_{line} is the flux of the selected peak. After this last passage it is possible to plot the results and check if the extra components of each profile are related to the others. Clearly the nitrogen emissions should be removed from the Hα fit to superimpose the lines easily. Some examples are given in Figure 2.9. In the first row we have *WISEA J211646.34+110237.4* with the comparison of Hα (in red) with Hβ (in green) and [O III]λ5007 (in blue). As we can see from panel (a) the Balmer lines show similar profiles. The extra components, depicted with the dotted vertical lines, do not coincide in velocity. This is interesting because the BLR which produces these features is the same region in both cases, but this cannot be inferred from this spectra. In panel (b) we have the same AGN, but the selected lines are Hα and [O III]λ5007. Despite the wings which are not present in the oxygen blue profile, the central part seems to be analogue.

In the second row we have a "bad fit" case, *WISEA J084205.57+075925.5*. Here the comparison between the Balmer lines is surprisingly useful. Both the added Gaussians present almost identical velocities between these profiles, which confirms the idea of the common BLR emission. It is important to stress that the left side of this spectrum is not well fitted in the Hα line. Concentrating on the [O III]$-$Hα parallel, again the central region (NLR emission) is basically the same in the two

lines.

In the left part of the last row we have *FBQS J1610+3303* and *WISEA J134915.20 +220032.6* on the right. The first object shows a very good agreement between the two fitted hydrogen lines and the extra components have basically the same velocity values. The same for the other source in which the comparison is between the two oxygen features at 4959 and 5007 Å. This is the only case in which [O III] lines were superimposed. The reason is related to the number of curves employed in the fitting, three Gaussians. This last source is very interesting, the complex [O III] emission can be possibly related to an ongoing merging process as we can see from the SDSS image in the Appendix (Figure B.5, panel g).

2.5 Line ratios

One of the most useful tool to exploit in the spectroscopic studies is line ratios. The idea is to consider different emission features and calculate the ratio between the intensities, the FWHM, and so on. The final aim depends on the selected lines, for example the O_{123} diagram represents the ratio between the oxygens. The x-axis is a tracer of the hardness of the ionizing spectrum at large radii from the source, while the y-axis a measure of the ionization level (Vaona et al., 2012). Globally this plot separates different AGN types. Other classification methods are the VO and the BPT diagrams in which the involved lines are [N II]λ6583, [S II] doublet, [O I]λ6300, [O III]λ5007, Hα, and Hβ. In particular, a high ratio between the ionized forbidden lines and the neutral permitted ones implies more energetic radiation fields and so AGN (Hickox et al., 2018). Instead, if we plot FWHM(Hα) against FWHM(Hβ) we have insights on the velocity components of lines.

To summarize, line ratios are fundamental in the characterization of a source and its physical structure. In the following some results for the selected sample are presented.

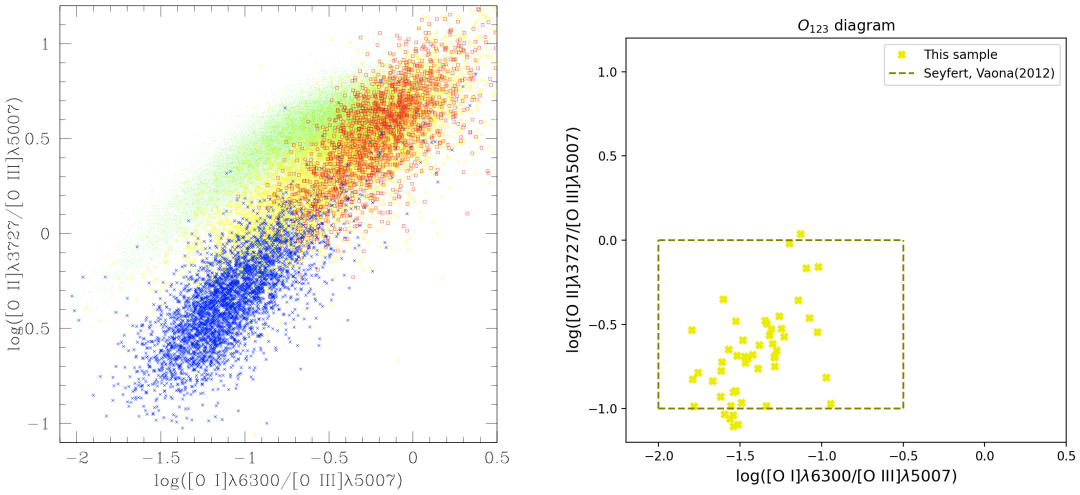

(a) (b)

Figure 2.10: (a) O_{123} diagram from *Vaona et al. (2012)* in which the oxygen line ratios are useful in dividing the AGN between Seyfert 2 in blue, LINERs in red, and SFG in green. (b) O_{123} diagram of the selected intermediates (yellow crosses). Almost all the objects fall in the same region with respect the Sy2 sample of Vaona.

2.5.1 O_{123} diagram

This diagnostic diagram in general is used for selecting specific AGN types as Sy2, LINERs, or star forming galaxies. The basic idea is to plot [O II]λ3727/[O III]λ5007 (indicated also as O_{23}) against [O I]λ6300/[O III]λ5007 (called O_{13}). The first ratio indicates the ionization level, while the second the hardness of the ionizing spectrum at great distances from the centre. The advantages of these plots are the presence of three different states of ionization in the optical range, the oxygen emissions presence in all the AGN spectra, the sensitiveness to the ionization parameter defined before (see section 1.3.3), and the non contamination of stellar features. A negative aspect is the reddening effect which acts more on O_{23} with respect to O_{13}. Indeed, [O II]λ3727 is in the longest wavelength part of the spectrum which means that is more affected by the reddening (Vaona et al., 2012).

As we can see from Figure 2.10, panel (a) shows the reference plot in which Sy2 galaxies are depicted with the blue crosses. That type of Seyfert galaxies was the central part of the sample in the Vaona study. Concentrating on (b) we can easily see how in the same region, indicated with the olive rectangle, the vast majority of

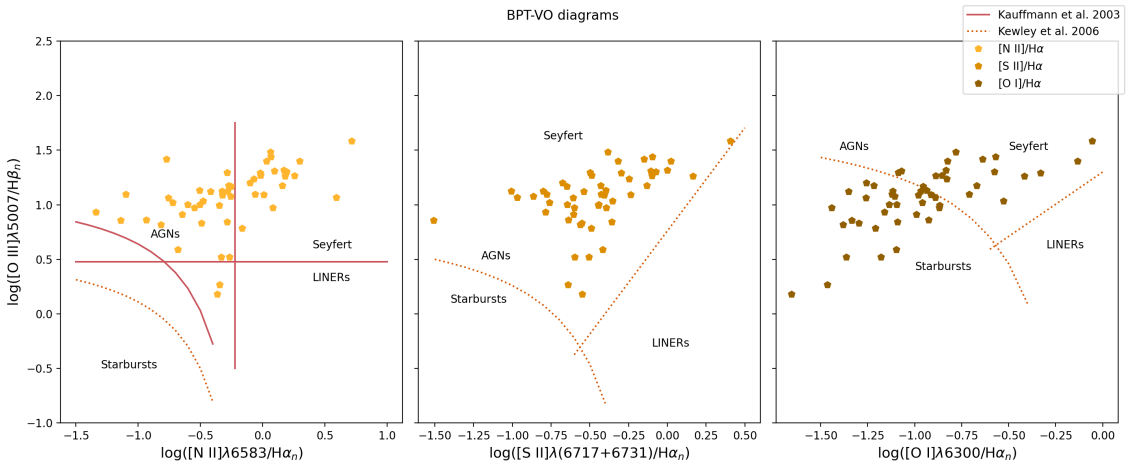

Figure 2.11: BPT and VO diagrams of the selected sample. Starting from the first part we have: a comparison between [N II]λ6583/Hα, [S II](6716+6730)/Hα, and [O I]/Hα with [O III]/Hβ in the y-axis. The reference curves and lines comes from Kauffmann et al. (2003) in solid pale red and Kewley et al. (2006) in dotted orange. These tracers identify some regions as the AGN/starbursts ones or the division between Seyfert galaxies and LINERs.

the intermediates can be found. This should be a signal that also IS present similar characteristics as Sy2 under the oxygen lines point of view. Consequently, they can be diagnosed in the same way using this plot. Unfortunately there are no studies on Sy1 in which the O_{123} diagram is considered. It will be very interesting to understand how these AGN are organized in terms of O_{123}.

Returning to the IS sample, there is a great concentration of galaxies in the low part of the diagram indicating lower ionization levels and lower hardness of the ionizing spectrum. In any case these trends should be improved by a larger statistical base.

2.5.2 VO and BPT diagrams

Figure 2.11 presents BPT-VO diagrams of the selected IS. In the same plots we can recognize the curves that divide the space in two regions. In the bottom part we have star-forming while in the top one AGN. This behavior is produced by the different radiation field characteristics as explained before in the introduction. [N II], [S II] and [O I] emission lines arise preferentially in a zone of partly ionized hydrogen. This zone is quite extended in objects photoionized by a spectrum containing a large fraction of high-energy photons, but it is nearly absent in galaxies photoionized by OB stars. This is the physical difference that distinguishes a narrow-line AGN from

an H II region-like object (Veilleux & Osterbrock, 1987). From these considerations some parameters to distinguish between the different ionization mechanisms were found. The used ones come from Kauffmann et al. (2003) depicted with the solid pale red lines and Kewley et al. (2006) with the dotted orange ones. In particular the equations for the first plot are ([N II]/Hα):

$$\begin{cases} log\left(\frac{[OIII]}{H\beta}\right) > \frac{0.61}{log[NII]/H\alpha - 0.05} + 1.30 \quad , \quad \frac{[OIII]}{H\beta} > 3 \quad , \quad \frac{[NII]}{H\alpha} > 0.06 \\ log\left(\frac{[OIII]}{H\beta}\right) > \frac{0.61}{log([NII]/H\alpha) - 0.47} + 1.19 \end{cases} \tag{2.3}$$

For the second one ([S II]/Hα):

$$\begin{cases} log\left(\frac{[OIII]}{H\beta}\right) > \frac{0.72}{log([SII]/H\alpha) - 0.32} + 1.30 \\ log\left(\frac{[OIII]}{H\beta}\right) > 1.89 \cdot log([SII]/H\alpha) + 0.76 \end{cases} \tag{2.4}$$

And for the last plot ([O I]/Hα):

$$\begin{cases} log\left(\frac{[OIII]}{H\beta}\right) > \frac{0.73}{log([OI]/H\alpha) + 0.59} + 1.33 \\ log\left(\frac{[OIII]}{H\beta}\right) > 1.18 \cdot log([OI]/H\alpha) + 1.30 \end{cases} \tag{2.5}$$

In the following all the references comes from Kewley et al., 2006. The first line of Equation 2.3 represents the Kauffmann group. The first of these together with the second line of the same system and the firsts of the other two, indicate the division between AGN and starbursts in the three plots. The other two conditions in eq. 2.3 identify the separation between Seyferts and LINERs. The same for the second lines of eq. 2.4 and 2.5. We can say that LINERs and Seyferts have different properties: the former have older stellar populations, are more massive, less dusty, present higher velocity dispersions, and lower [O III] luminosities. Furthermore, considering a fixed L[O III]/σ^4 value, which is an indicator of $\dot{M}$, all differences between Seyfert and LINER host properties disappear. The correlation between L[O III]/σ^4 and $\dot{M}$ comes from two considerations: 1) the accretion rate is proportional to L_{bol}, while the stellar velocity dispersion can be used as an estimate of M_{BH}; 2) in Sy1 and quasars $L_{[OIII]}$ scales with L_{bol} (see section 2.7.2). This means that $L[OIII]/\sigma^4$ is proportional

to $\dot{M}$. Finally, on average, LINERs have low ionization lines that are much more prominent than what is typically observed in Seyfert galaxies.

The two curves in the first plot depicts the different classifications proposed by Kewley and Kauffmann. The last one modified the previous scheme to include an empirical line dividing pure star-forming galaxies from Seyfert–H II composite objects whose spectra contain significant contributions from both AGN and star formation. In the [N II]/Hα panel the Kauffmann boundaries seems to fit better than the Kewley ones.

Globally referring to Figure 2.11, the points are spread in the Seyfert region as expected. The only critical point is the ratio [O I]/Hα, here part of the sources also lie in the starburst zone. It is important to stress that the oxygen line at 6300 Å is a very faint one and so in some cases the fit could be not optimal. Another point is that the used spectra are not corrected for the galaxy contribution and for the reddening effect, which can be related to the difficulty in comparing our results with the Kewley ones. Returning on the boundaries, the maximum starburst line is defined by the upper limit of the theoretical pure stellar photoionization models. Galaxies lying above this line are likely to be dominated by an AGN. Following this separation, Kewley defined as ambiguous those galaxies which lies in the starbursts region in one or two diagrams and in the AGN zone in the remnant ones. So the sources that lie below the AGN/starburst line in the [O I]/Hα plot could be transitional objects or composites. The optical spectra of these composites can be due to either a combination of star formation and a Seyfert nucleus, or a combination of star formation and LINER emission. This means that these classes represent a conjunction between two groups. This separation is arbitrary, because there was no clear division in the last diagram between the classes. Another problematic point is the percentage of ambiguous galaxies identified in the [O I]/Hα plot. From the Kewley study the fraction of this type of sources is around the 8%, while in our case is the 62%. Comparing the characteristics of the intermediates in the two regions of the last BPT diagram we can state that the problem is not concerning the S/N ratio, indeed the difference between the groups is only around 1.6. Another possibility could be the fitting process. As we said previously, the [O I] line is very faint and so

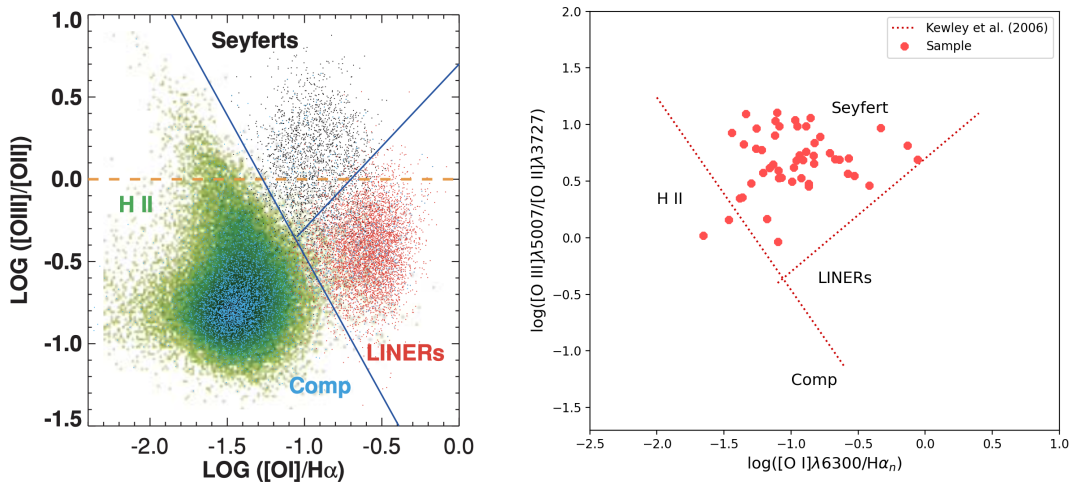

(a) (b)

Figure 2.12: [O I]λ6300/Hα vs [O III]λ5007/[O II]λ3727 plots. (a) Reference diagram in which the galaxies are separated by some empiric relations into H II, composites, Seyferts, and LINERs. The figure is from *Kewley et al. (2006)*. (b) The same plot, but for the selected sample.

this makes the fitting difficult. Comparing the two χ^2_{red}, which is a goodness reference parameter, the confirmed AGN show a mean value of 65.58 while the ambiguous IS around 72.47. Generally [O I] is well fitted in those galaxies that fall in the upper right part of the plot. There seems to be a difference between these groups, but in any case it is not net. Some authors stressed the inconsistency in the [O I]/Hα with the photoionization models adopted, saying that maybe the calculation of the flux of the faint line might suffer from missing non thermal heating sources (Ji et al., 2020).

2.5.3 [O I]/Hα vs [O III]/[O II] diagnostic

Another diagnostic is based on the comparison between [O I]/Hα and [O III]/[O II] in a sort of mixed $O_{123}-$BPT diagram, which is shown in Figure 2.12. The reason for the separation is twofold: [O III]/[O II] is a sensitive diagnostic of the ionization parameter of the gas, whereas [O I]/Hα is sensitive to the hardness of the ionizing radiation field. Seyfert galaxies have a higher U than LINERs or star-forming galaxies. Therefore, Seyferts separate vertically from the other classes of objects.

Both Seyfert galaxies and LINERs have hard power-law ionizing radiation fields and thus are separated from star-forming galaxies in the horizontal direction (Kewley et al., 2006). The boundaries for the Seyfert region are:

$$\begin{cases} log\left(\frac{[OIII]}{[OII]}\right) > -1.701 \cdot log\left(\frac{[OI]}{H\alpha}\right) - 2.163 \\ log\left(\frac{[OIII]}{[OII]}\right) > 1.0 \cdot log\left(\frac{[OI]}{H\alpha}\right) + 0.7 \end{cases} \tag{2.6}$$

As we can see from Figure 2.12 also those objects that were classified as starbursts in the BPT/VO diagram fall in the Seyfert region, excluded two cases. In the original plot, panel (a), ambiguous sources were not considered differently in our case where they are included. Comparing the S/N ratio and the χ^2_{red} of the two groups, we have a substantial difference in the first parameter. The separation between the correctly classified Seyferts and the H II classified Seyferts, |S/N(Sy)-S/N(HII)| $\sim$ 6.8, indicates high quality spectra in the former class. Under the fitting point of view, χ^2_{red} reveals best fitted [O I] lines in the two H II galaxies. Again the solution is not easy to interpret, but as we said before it is important to keep in mind that Kewley results comes from corrected spectra while ours do not include host galaxy subtraction and internal extinction correction.

2.5.4 FWHM(Hα) vs FWHM(Hβ)

Plotting the FWHM of the first two Balmer lines we can compare the gas velocity of the different components. The three classes are: narrow, broad, and extra. These last ones identify those one or two Gaussians added to fit properly the BLR emission in the pathological cases. In general the results are accurately spread around the 1:1 line, indicating a correspondence between the two lines. This is due to the binding between the two FWHM in almost all the cases, as explained in section 2.3.1. In the left part of Figure 2.13 the narrow component (indigo crosses) strictly follow the diagonal. Indeed this feature in Hα is well constrain to the Hβ one, the same for the broad Gaussians (cyan big dots). For the other two cases there is some spread around the 1:1 line. The intermediate-broad feature (light blue stars) is well constrained in almost all the cases while the extra ones (blue small dots) do not. This is related to

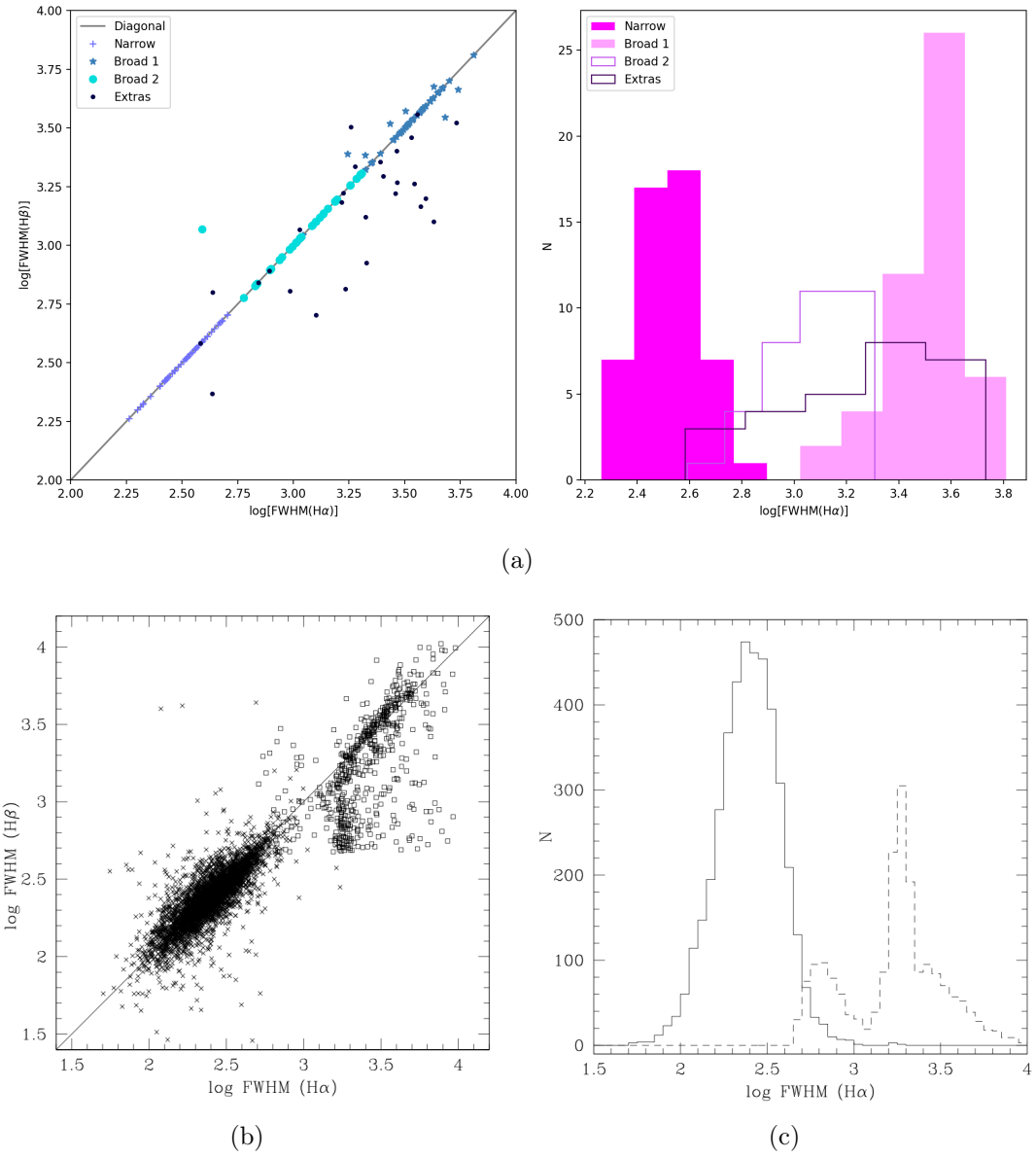

Figure 2.13: First raw, left side: FWHM(Hα) and FWHM(Hβ) for the 50 selected objects. All the components are plotted, the crosses indicates the narrow one, the big dots the broad one, the stars the intermediate-broad one, and the small dots the extra bumps. This last ones are present only in the pathological spectra. Right side: FWHM(Hα) histogram for the different components, in filled magenta the narrow one, in filled pink the first broad one, in unfilled pink the second broad one, and in unfilled violet the extra bumps. Second raw: tha same plots but for the Vaona et al. (2012) sample.

the missing relations between the added bumps of the two Balmer lines, in fact they were let free to vary specially in width. This implies that the extra components are not necessarily equal in the two lines, but this should be verified through the errors. In any case we can state that there is a sort of diagonal trend also for the small dots. Performing statistical tests, in particular Pearson, Spearman and Kendall correlations we can prove if the extra components shows a real diagonal trend. The results for the three cases are $(r_p, p-value) = (0.80, 4.42 \cdot 10^{-7})$, $(r_s, p-value) = (0.70, 4.77 \cdot 10^{-5})$ and $(r_k, p-value) = (0.51, 1.10 \cdot 10^{-4})$. From these numbers we can infer that the p-value is such that also for the last component there is a real correlation between the two lines, assuming a confidence level of 95%. The rank is positive, and the relationship is strong as for the diagonal trend of the other components.

In the right part of the same figure there is a histogram which represents the widths of the different components of the Hα line and the corresponding number. As in the previous plot, the first three features present concentrated values while the last one (extra, in unfilled violet) is more diffuse. Another thing to note is the number of objects for the two unfilled histograms. These small values are due to the presence of three Gaussians only in some profiles (see the pink unfilled plot) and more than three just in the pathological objects (see the violet unfilled plot), for a comparison see Table 2.1.

Comparing these results with the Sy2 ones (Vaona et al., 2012), the two plots, in panels (b) and (c) of Figure 2.13, agrees showing an increasing spread according to the number of components in the FWHM one, and wider and smaller peaks in the histograms.

2.6 IS type

As we can see from Figure 2.14 there are four histograms which show the sub-classification of IS galaxies of the selected sample. The first separation in panel (a) was operated using the Whittle (1992) method which compares the fluxes between the [O III]λ5007 line to the Hβ one, including the BLR components. The boundaries were presented in section 1.2.2. In panel (b), (c) and (d) the selection method was

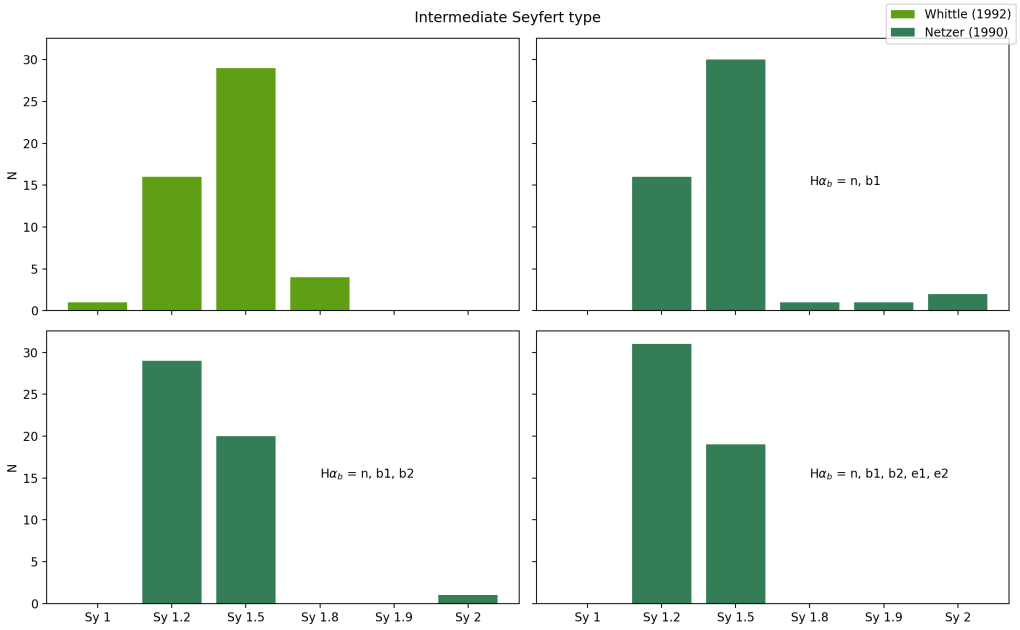

Figure 2.14: (a) Seyfert type histogram obtained from the ratio between the fluxes of [O III]λ5007 and Hβ using the Whittle (1992) method. (b), (c) and (d) The same plot but using the method described by Netzer (1990). It exploits the ratio between the narrow and broad component of Hα. The difference between the three Netzer plots is on the selected components to include in the Hα broad one due to the fact that this is not specified in the paper.

the Netzer one always described in section 1.2.2. This division was made by the ratio between the narrow and the broad component of the Hα profile (see Equation 1.1). In the dark green plots are also specified what components were included in the calculus of Hα_b. In the first case only the broad$_1$ Gaussian was taken into account, in the second one the two broad curves and in the last one all those features that are not the narrow one.

As said at the beginning, the initial goal was to obtain a homogeneous sample, which is partially achieved in terms of Sy1.2 and Sy1.5. For the other classes the number of sources is limited. Comparing these results with the selection characterization (see section 2.1) we can state that Sy1.5 are easy to distinguish also through visual inspection, while the other groups were mixed and misclassified.

If we concentrate on the two selections, we have similar results in the two main Seyfert types, while there are substantial differences on the major classes (Sy1.8, Sy1.9 and Sy2). The Whittle ratio do not recognize any Sy1.9 (and over), while the Netzer one identified also some Sy2. There are also some inconsistencies if we

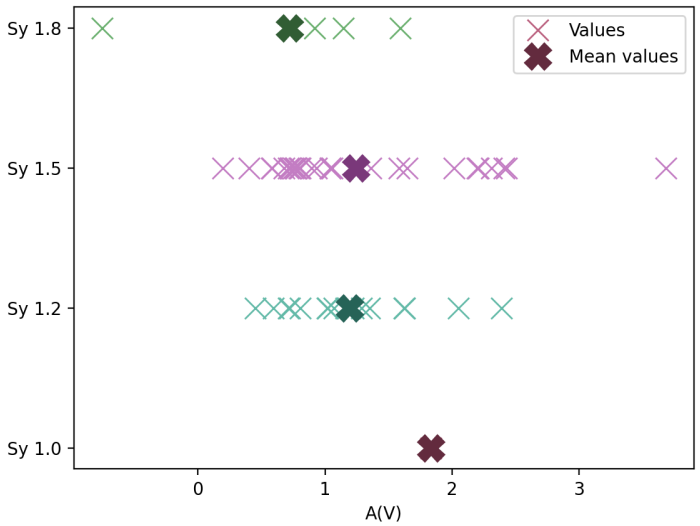

Figure 2.15: The internal extinction values calculated through Equation 2.7 and divided for the identified Seyfert classes in Figure 2.15. The thin "×" indicate the calculated $A(V)$ for each object, while the thick crosses the mean value for the single classes.

compare the Netzer histograms. Including different components, the classification changes moving towards a result similar to the Whittle one. Probably this last ratio is more reliable due to the fact that the selected lines, [O III]λ5007 and Hβ, present less pathological profiles with respect the Hα one. Another point is that it is not clear if the extra bumps should included in the Balmer lines broad components, and this limits the second classification.

2.7 Physical quantities

2.7.1 *A(V)* and Balmer decrement

From the ratio between the narrow components of Hα and Hβ we can find the extinction $A(V)$ for each galaxy in the sample. The reference equation is the following from Cardelli et al. (1989):

$$A(V) = 7.215 \cdot log\left(\frac{2.86}{R}\right) \quad , \quad R = \frac{H\alpha}{H\beta} \tag{2.7}$$

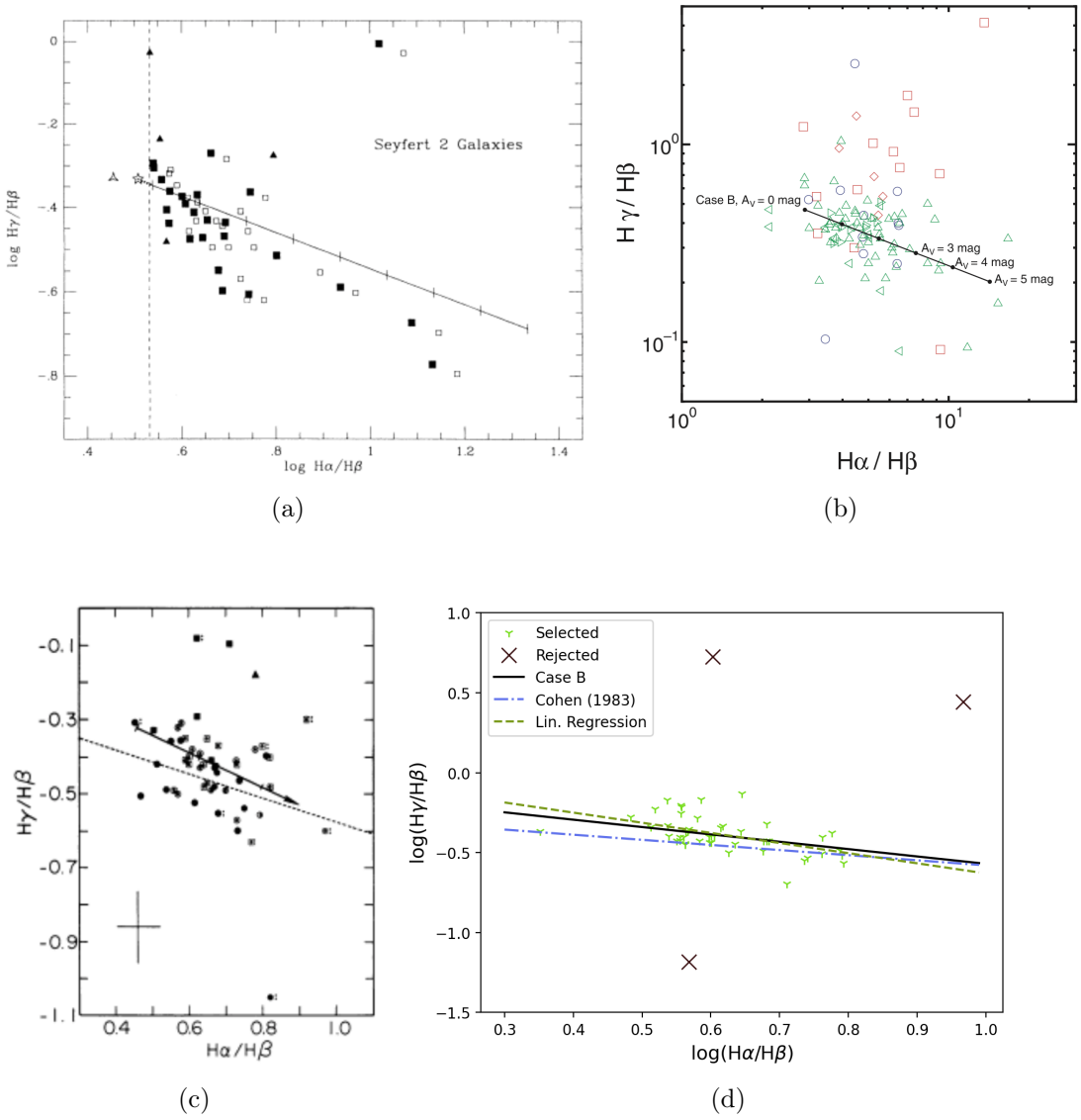

(a) (b)

(c) (d)

Figure 2.16: Balmer decrements comparison between Hα/Hβ and Hγ/Hβ. In panel (a) the results from *Binette et al. (1990)* on a sample of Sy2, the symbols indicate the samples from which the objects comes from and the solid line the reference case B recombination. In panel (b) the *Nagao et al. (2001)* results for a group of NLS1, BLS1, Sy1.5, and Sy2. The markers indicates the listed objects in the same order: diamonds, squares, circles and triangles, while the black line is the case B reference. In panel (c) the plot for the *Cohen (1983)* IS sample, the symbols are related to the intermediate type. Again the solid line refers to the recombination theoretical reference while the dotted one to the best fit. In the last panel (d) the results for the selected objects in this work. The dashed and the solid lines are the references (Cohen fit and case B), the dotted green line the fitted trend.

Assuming a theoretical ratio of 2.86. In Figure 2.15 there are the results divided according to the Whittle (1992) classification operated before. As we can see, the mean value (indicated by the thick crosses) tends to decrease moving from Sy1 to Sy1.8. The numeric values are: 1.83, 1.19, 1.24 and 0.72. Obviously it is important to stress the scarcity of Seyfert 1 and 1.8 in the sample, which can also contribute to the results. See for example the single point for the first type. Vaona et al. (2012) obtained a median value of 1.4 for the Sy2 and 0.9 for IS and explained these outcomes as a deeper look inside the NLR for the IS galaxies together with a lower dust quantity due to winds and sublimation. This trend is confirmed for Sy1.5 and Sy1.2, which represents the vast majority of the sample. These groups show a decreasing trend according to the Seyfert type. For the others, the results clearly disagree with the Vaona ones, but as previously noted this may come from the small number of selected sources. Another thing to stress is the Sy1.8 object with a negative $A(V)$ which is an unphysical value. This source is a bad fit case, in particular *WISEA J164819.02+302210.8*, which can be seen in the first part of Figure 2.7. Due to the difference between the real profile and the fitted one, this reddening is not reliable. A possible future step could be calculation of the errors, in this way the obtained results should be more comparable to the others.

Other authors preferred to compare directly the Balmer decrement between Hα/Hβ and Hγ/Hβ, as we can see from Figure 2.16. The first three panels present the results from Binette et al. (1990), Nagao et al. (2001), and Cohen (1983) respectively. The selected sample are different: in the first work only Sy2 were present, in the second one a mixture of AGN, and in the last only IS. Panel (d) shows the results for the current objects. In all the diagrams we can see the reference theoretical case B trend (solid line) that Cohen summarized with the values of -0.46 and of -0.11 for the slope and the intercept. Their fit presents a slope of -0.32 and an intercept of -0.26 (dashed line). For the current sample the values are -0.63 (more inclined) and 0.004 as intercept, as we can see from the comparison in the last plot (dotted profile). If we compare the regions occupied by the sources we can easily see how Sy1 (red sources in panel b) tend to be above the reference line, Sy2 (panel a, and the green triangles in panel b) under or along the case B line, while intermediates

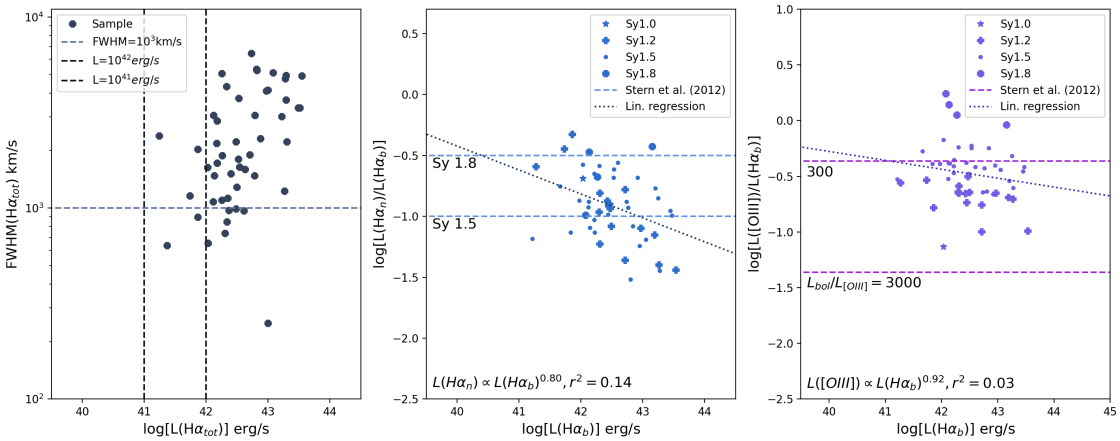

Figure 2.17: Results for the comparison between the total luminosity of Hα and (a) its FWHM, (b) the ratio L(Hα_{narrow})/L(Hα_{broad}) and (c) the ratio L([O III])/L(Hα_{broad}). The horizontal and vertical lines comes from *Stern et al., (2012)*. While the inclined ones represents the linear regression to the data. Additionally the different symbols correspond to the indicated Seyfert type ("stars" type 1, "crosses" type 1.2, "dots" type 1.5, and "octagons" type 1.8).

(panels c and d) follows the reference. Obviously this trend should be confirmed using a composite sample as the Nagao one. They noted that most of the Sy2 can be well described by the case B prediction taking the effects of dust extinction into account, while most of the Sy1 cannot be explained by the same prediction with dust extinction (Nagao et al., 2001). A noteworthy aspect is that in the selected sample three objects were rejected in the linear regression operation due to their very large distance from the others, see the dark crosses in panel (d). Two of them present very low S/N ratio and so the fitting procedure, in particular for the faint Hγ, is not so reliable. The third rejected source was a bad fit case, in particular the one in the right upper part of Figure 2.7.

2.7.2 Hα and [O III] luminosities

Stern et al. (2012) show how the luminosity (L) obtained from the [O III]λ5007 profile gives information about the bolometric luminosity and some insights on the nature of intermediates. Their sample was selected through the Hα broad component characteristics. The idea is to apply their classification to our sources in order to see if the two classifications agrees and then calculate L_{bol}. In Figure 2.17 we can see the results. In the first panel we have the distribution of the objects in

the total FWHM(Hα), or Δv, versus the Hα luminosity plane. As a reference the horizontal line at FWHM=10^3 km s^{-1} is also plotted. The trend for our sample almost corresponds to the Stern one showing a decreasing in FWHM(Hα) profile with the luminosity. The transition from Δv<10^3 km s^{-1} to Δv>10^3 km s^{-1} (horizontal line) falls around $L(H\alpha) \sim 10^{42}$ erg s^{-1} while Stern identify a value of 10^{41} erg s^{-1}. This can imply that at low L the NLR component dominates the spectra while the BLR is the main one at high luminosities. Or that our IS represent the principal class of AGN in the $L(H\alpha) > 10^{42}$ erg s^{-1} range. As a consequence, we can say that the parameter $\Delta v > 10^3 km/s$ is a valid classification method to select those AGN in which Hα is dominated by the broad component, as for the IS.

The second panel shows the relation between the Hα luminosity in its narrow and broad components. As we can see the trend is evident even if the point spread is not negligible. If we compare this trend to the Stern one we have a different slope. Here the relation is a power-law with an index equal to 0.80 while in the reference paper is around 0.66$\pm$0.01. In the same plot, we have the separation between the Seyfert type according to the Whittle (1992) method, indicated with different symbols. From this plot we cannot see a strong correlation between the two axes, neither with the Stern reference dashed lines. The results for the statistical tests (the same as in section 2.5.4) are: $(r_p, p-value) = (-0.38, 6.75 \cdot 10^{-3})$, $(r_s, p-value) = (-0.37, 7.74 \cdot 10^{-3})$, and $(r_k, p-value) = (-0.26, 7.25 \cdot 10^{-3})$.

In the last plot the comparison included the [O III] luminosity. Here the points are even more spread around the linear regression result and the slope is 0.92 while Stern calculated a value of 0.72$\pm$0.01. In any case a decreasing trend seems to be confirmed, even if the slopes are not comparable. Again an error measure is needed for our IS sample. If we observe the plot of Figure 2.17 a true separation between the classes is clear. In general, when increasing the Seyfert type the ratio between the [O III] and the Hα_b luminosity decreases as Stern noted. Probably this clear division comes from the fact that the Whittle classification is based on the same properties: the [O III] flux and the Hβ (related to Hα) one. Then we can calculate the ratio between the oxygen luminosity and the bolometric one (L_{bol}) in order to use the narrow line as a tool. Assuming that $L_{bol}/L_{H\alpha}^{broad} = 130$ (Stern et al., 2012),

we obtained:

$$\frac{L_{bol}}{10^{43} erg/s} = 465 \cdot \left(\frac{L_{[OIII]}}{10^{43} erg/s} \right) \tag{2.8}$$

The proportionality factor is around 450, instead of the reference 4000-3500. This difference can come from the limited number of points in the sample, but this trend agrees with the Stern consideration that Sy1.5 will tend to have lower intrinsic luminosities than Seyfert 1s, while Sy1.8s will have even lower L_{bol}. The tendency of Seyfert 1.8s to have low bolometric luminosities has been noted by other authors (Deo et al., 2007, 2009; Trippe et al., 2010).

The decreasing of the observed BLR emission cannot be explained in terms of a partial obscuration or a reddening, Stern says. In the first case the problem is with the dimension of the obscurer and the fraction of the object that can be seen in the UV. While the second possibility seems to be not valid due to the presence of the same kind of decreasing trend both in the second and the third plots which present lines characterized by different opacities. This can be also referred to the results in section 2.7.1 where Figure 2.15 shows an unclear situation in the $A(V)$ measure. Another interesting quantity can be the covering factor (CF) of the two regions. A decrease in the CF_{NLR} value will produce the drop in $L(H\alpha_n)/L(H\alpha_b)$ and $L([OIII])/L(H\alpha_b)$ with $L(H\alpha_b)$.

A consequence of this reasoning is that the last plot can be used in the type 2s selection, dividing those objects that do not have a BLR (true Sy2) from the ones that are only obscured (standard Sy2). For the IS classification this should be confirmed with more data.

2.7.3 Black hole mass

The classical way of estimating the black hole mass is to use the relation between $M_{BH} - \sigma_*$. The problem is what is a good tracer of the dispersion σ_*. As a reference we can use Equation 1.3, where the mass is related to the BLR radius and to the velocity variation through constants. In particular, G and f_{BLR} which gives information about the inclination of the AGN. The projection dependent factor in this case is assumed to come from the isotropic distribution of the BLR clouds hypothesis

in which $v = \sqrt{3}/2 \cdot$ FWHM. In reality this approximation is the most diffused one, but was criticized by some authors who preferred a disc model for the BLR (Decarli et al., 2008). Indeed they show how the mass can be well estimated by this shape for the BLR. This is also valid for the intermediates where the BLR is only partially visible. Another aspect to take into account, and linked to this reasoning, is that in IS we can see only a limited portion of BLR. As a consequence, the calculated mass will be not exactly the true value, but a limit. Particularly, the M_{BH} determination pass through the use of the FWHM instead of the dispersion velocity. It makes the implicit assumption that the velocities are distributed randomly in the BLR. If this component is a flat structure dominated by rotation, the FWHM is also proportional to the angle between the normale and the line of sight. This implies that small inclination can lead to a large underestimation of the keplerian velocity and therefore of the mass (Collin & Kawaguchi, 2004). Starting from these considerations we can list the exploited methods to obtain M_{BH}. The first one comes from Greene et al. (2010) where the FWHM is the Hβ broad component one and the dimension of the BLR is:

$$log\left[\frac{R_{BLR}}{10\ light\ days}\right] = A_2 \cdot log\left[\frac{L(H\beta_b)}{10^{43} erg/s}\right] + B_2 \tag{2.9}$$

With $A_2 = 0.53 \pm 0.04$ and $B_2 = 0.85 \pm 0.05$. The results are in Figure 2.18 indicated by the yellow points. In this sample the masses ranges between $10^6 - 10^9\ M_\odot$, which agrees with the general mass trend of SMBHs.

The second method comes from Kaspi et al. (2000) who preferred the use of $\lambda L_\lambda(5100)$ to estimate the R_{BLR} term with respect the Hβ luminosity as before. Unfortunately in IS the host galaxy contribution is not negligible. As a consequence, the continuum luminosity at 5100 Å is often overestimated and in turn an higher M_{BH} with respect the real value. In any case it is interesting to see what are the results and compare them to the others. The FWHM is always related to the Balmer line. The reference equation is:

$$\frac{M_{BH}}{M_\odot} = 4.82 \cdot 10^6 \left[\frac{\lambda L_\lambda(5100)}{10^{44} erg/s}\right]^{0.7} \left[\frac{FWHM(H\beta)}{10^3 km/s}\right]^2 \tag{2.10}$$

The calculated values are again in the same figure but indicated by the green symbols. The mass range is the same as before, even if we can recognize that this method led

to slightly high masses with respect the previous one. This trend can be confirmed when we calculate the difference between the two masses of the single objects. The mean difference is 0.19 $M_{\odot}$. Even if not so relevant, this can be attributed to the host galaxy contribution.

The third method is the Ho & Kim (2014) one which considers the [O III]λ5007 profile, and so a narrow line. This comes from the consideration that, because of the dusty torus, the Hβ profile is highly affected by the partial obscuration and so it seems to not be a good choice. An idea can be to exploit the forbidden lines, as [O III], dividing the profile in the core and in the wing component. It is important to keep in mind that the oxygen poorly correlates with σ_* and so the dispersion outcome should be interpret as an upper limit. In the following the used equation (Ho & Kim, 2014):

$$log\left[\frac{M_{BH}}{M_{\odot}}\right] = 8.49 + 4.38log\left[\frac{\sigma_*}{200km/s}\right] \tag{2.11}$$

with $\sigma_* = FWHM^{core}_{[OIII]}/2.35$. The values are in the central panel of Figure 2.18 depicted with the blue dots. The linear trend comes from the nature of the equation which gives a directly dependence between M_{BH} and σ_*.

Concentrating on the plot in the right part of Figure 2.18, there is a direct comparison between the methods that exploits the Hβ profile (Greene and Kaspi) versus the one with [O III]λ5007 (Ho & Kim). It is particularly interesting how the points are spread. The x-axis is basically all covered by the results while the y-axis sees a sort of concentration around $\log(M_{BH}) \sim 7.7$ $M_{\odot}$. The median and the standard deviation for these points is (7.66$\pm$0.47). Probably this is related to the low reliability of the Nelson & Whittle (1996) method used by Ho & Kim. The link between FWHM([O III]) and σ^* is not so close, and this can be the reason under the observed trend. If we consider again the difference between the calculated masses we have 0.55 $M_{\odot}$ and 0.61 $M_{\odot}$ comparing Greene - Ho & Kim methods and Kaspi - Ho & Kim ones respectively. The separation in these cases is more relevant underlying the different nature of the listed tools.

To understand if these measures are reliable or affected by an underestimation

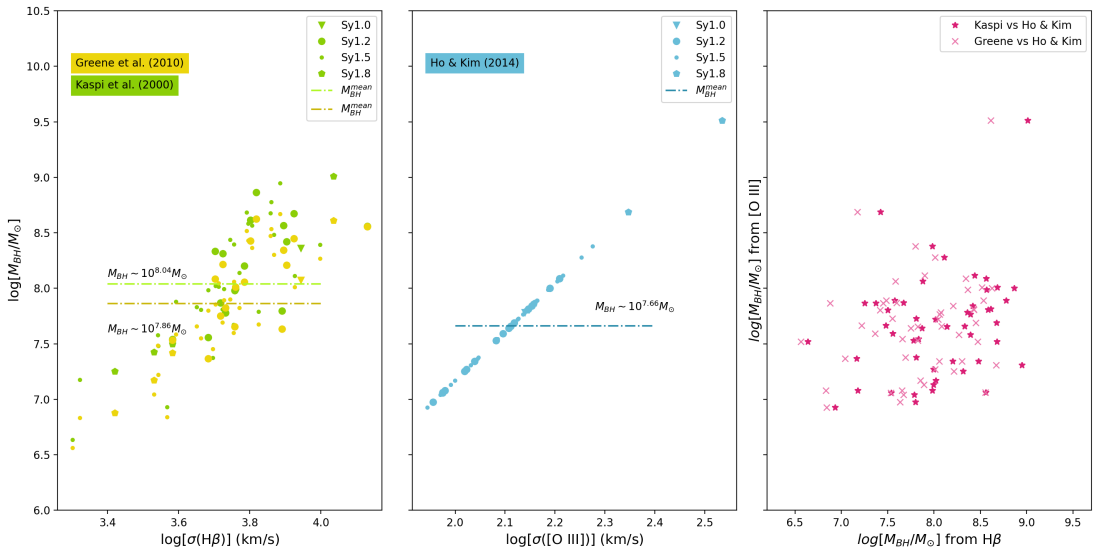

Figure 2.18: The results for the three methods employed in the calculation of the black hole mass. The horizontal lines represents the mean value for the sample. All the calculated M_{BH} are in between $10^6 - 10^9$ $M_\odot$. The different symbols of the first two panels are related to the Seyfert type considered from the Whittle classification. In the last plot is presented the comparison between the results obtained using the Hβ line (x-axis) and the [O III] one (y-axis).

introduced by the partial observation of the BLR, other methods should be employed. One of the most important is the reverberation mapping which is based on the study of the effects of the gravitational field produced by the BH on the surrounding gas. Particularly it estimates the radius of the BLR from the time delay between the difference in the response of the emission lines with respect variation of the continuum. Unfortunately only for one of the selected sources this technique was applied, Mrk 110. The obtained value is $M_{BH} = (1.4 \pm 0.3) \cdot 10^8 M_\odot$ (Porquet et al., 2021) which should be compared to the calculated ones: from the first method we have $2.37 \cdot 10^7$ $M_\odot$, from the Greene equation $2.83 \cdot 10^7$ $M_\odot$, and for the [O III] one $7.33 \cdot 10^7$ $M_\odot$. So we can confirm that the Hβ and the [O III] lines gives only underestimations of the black hole mass. Particularly the large discrepancy between the two masses is explained by the use of a virial factor of $f \sim 1$, which is equivalent to a thin disk BLR with an inclination of 30 degrees. Therefore the discrepancy can be related to an higher value for f, and so a system seen almost face-on (Porquet et al., 2021). The same can be inferred for the other AGN, but as we said, we need the reverberation mapping evaluation of the BH mass.

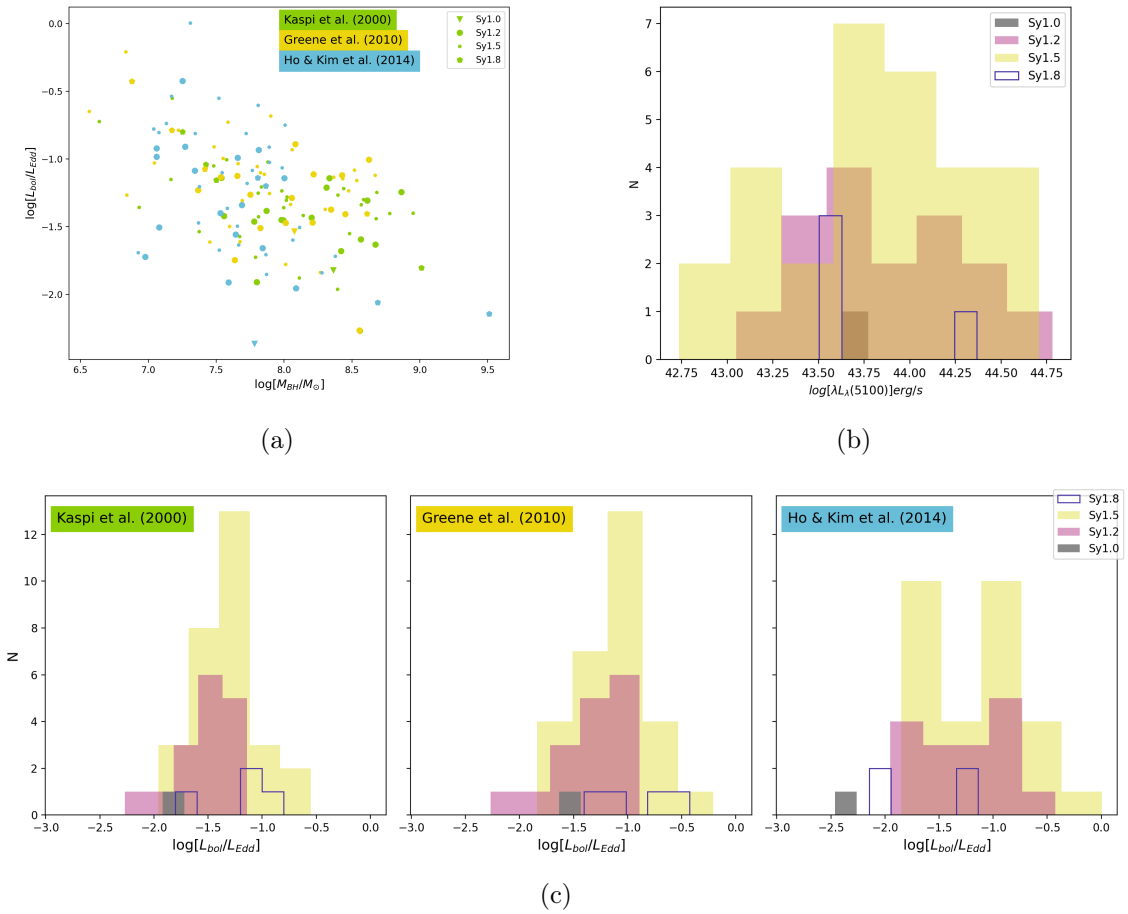

(a) (b)

(c)

Figure 2.19: In panel (a) the comparison between the calculated masses and L_{bol}/L_{Edd}. The three methods are indicated as in Figure 2.18. In panel (b) the comparison between the different Seyfert type and the continuum luminosity used to calculate the bolometric one. In panel (c) The Eddington ratio divided for the three methods and for the Seyfert classes.

2.7.4 Eddington ratio

Another extremely important characteristics for AGN is the Eddington ratio, and so the comparison between the bolometric luminosity (L_{bol}) and the Eddington one (L_{Edd}). This gives insights on the accretion process showing what is the rate at which the BH "sucks" the surrounding material. The reference is the Eddington limit, which comes from the balance between the gravitational force and the radiation pressure in a spherical body. This is strictly true for those objects that are in hydrostatic equilibrium. Due to this strong hypothesis, in our case we can have some AGN that overcome this reference. The value can be calculated starting from the M_{BH}

obtained before and then using:

$$L_{Edd} = 1.3 \cdot 10^{38} \frac{M_{BH}}{M_{\odot}} \tag{2.12}$$

And for the bolometric luminosity we can exploit the continuum one:

$$L_{bol} = 9 \cdot \lambda L_{\lambda}(5100) \tag{2.13}$$

From a value calculated in a single energy band, plus a fixed correction, we get the total luminosity (Komossa, 2007). These equations were exploited to obtain L_{bol}/L_{Edd}. Again it is important to keep in mind that the continuum luminosity is highly affected by the host contribution, so this should be considered as an upper limit. In the previous section we obtained the mass using three different methods. As a consequence we will have three evaluation for the Eddington ratio for each AGN. In particular, Equation 2.12 and 2.13 are used together with Greene and Kaspi masses. While for Ho & Kim we can exploit:

$$log\left[\frac{L_{bol}}{erg/s}\right] = (7.54 \pm 9.07) + (0.88 \pm 0.22) \cdot log\left[\frac{L_{[OIII]}}{erg/s}\right] \tag{2.14}$$

This law is an empirical one obtained by Berton et al. (2015) and can be used not only for NLS1, but also for Sy2 and IS samples. The results are depicted in Figure 2.19 panel (a) using the same colors and symbols as in Figure 2.18. There is not a clear division between the Seyfert types, the same for the Eddington ratios which are all in the range $10^{-2} - 10^{0}$. The Eddington limit is respected because none of the sources falls in the region $L_{bol}/L_{Edd} > 1$. On the other hand if we concentrate on panel (b) we can see how the two more represented classes, Sy1.5 and Sy1.8, show a small trend about the continuum luminosity. In particular, as the UM foresees, increasing the Seyfert type also the inclination increases together with the obscuration of the central regions. This can be translated in the diminished $\lambda L_{\lambda}(5100)$ observed, according to the class. This result, together with the host contribution, obviously should be taken into account when we compare the Eddington ratios which in turn depend on the bolometric luminosity and so on the continuum (see Equation 2.13).

In Figure 2.19 panel (c) we have L_{bol}/L_{Edd} for the three methods (Equations 2.12, 2.13, and 2.14) divided for the different Seyfert type. As we can see more clearly here, there seems to be a compatibility in the Eddington ratio values between the classes, no trend is distinguishable.

Another aspect to keep in mind is the dependence of L_{bol}/L_{Edd} from the black hole mass. As we stressed before, the estimation of M_{BH} for IS through Hβ and [O III] carries significant problems. In particular, the partial observation of the BLR which implies an underestimation of M_{BH} and consequently of the Eddington ratio.

2.7.5 Densities and temperatures

The values of electron density and temperature are calculated using the *PyNeb* package for Python. Its purpose is the analysis of emission lines such as [O III] and [S II]. In this specific case the involved ratios are [O III](5007+4959)/4363 for the electron temperature (T_e), and [S II]6716/6731 for the density (N_e). Fortunately, in these spectra the commonly faint [O III]λ4363 line were clearly distinguishable due to the high S/N ratio. In particular, *getCrossTemDen* gives the two quantities, T_e and N_e, starting from an initial guess. The selected temperature is $T_e = 10^4$ K. At the end of the calculus, the program gives the converged values for the temperature and the density.

The results can be seen in Figure 2.20 part (a). In the left panel we have the N_e distribution, the median of ~ 430 cm^{-3}, and the reference values for the Vaona et al. (2012) sample together with the Cracco et al. (2016) ones. The same for the right panel with T_e. In this plot we have two results from the Vaona study due to the nature of the sources. There the sample was divided between Sy2 and IS. In the Cracco case, instead, [O III]λ4363 was to faint to be detected and fitted. As a consequence, they preferred to assume the temperature of $T_e = 10^4$ K, and calculate only the densities from the sulfur lines ratio. The results for the current sample are: for N_e a median of 428 cm^{-3} with a standard deviation of 401 cm^{-3}, while for T_e 11524 K with a deviation of 3257 K. For the whole list see Table A.2 in the appendix. Comparing these values to the other works we have an agreement both in the temperature and in the density. Considering again Figure 2.20, in panel (b)

we have the same plots as in panel (a), but here the objects are divided according to the Seyfert type. The classification method comes again from Whittle (1992) described in section 1.2.2. In each of the two plots there is not a net separation between the classes, even in those well represented (Sy1.2 and Sy1.5). Bennert et al. (2006) compare two samples of Seyfert galaxies, in particular Sy1 and Sy2. Under the density point of view, they found a compatibility between the two types with results of $\sim 10^3$ cm^{-3}. This is slightly higher with respect to the median in our sample, but within the distribution. For the temperature Bennert obtained a difference between Sy1 and Sy2. The corresponding values are around T_e(Sy1) $\sim$ 33600 K and T_e(Sy2)$\sim$ 14500. In our case this difference cannot be confirmed. Comparing the median of our IS sample with the forementioned Sy1 and Sy2 ones, we have a T_e(IS) closer to the Seyfert 2s outcome rather than Seyfert 1s. This cannot be easily explained. In this case, the objects tend to fit well in the Sy2 family instead of Sy1. In Figure 2.21, we have a comparison between the Seyfert types in terms of [O III]5007/4363 and [S II]6716/6731. These two ratios were used to calculate T_e and N_e respectively. The classification is applied using, again, the Whittle (1992) method. In blue and light blue are represented the AGN of our sample, while in yellow and orange the data from Cohen (1983). In this work they put all the intermediates in the same class. As a consequence we can find a superposition between our Sy1.5 and those Seyferts. Sy2, instead, form a separate category. In these plots there is a clear trend both in the oxygen and in the sulfur lines ratio. Increasing the Seyfert type [O III]5007/4363 increases, while [S II]6716/6731 decreases. Again we should take into account that Sy1, Sy1.8, and Sy2 (this last one from Cohen) are underrepresented. In their study Cohen stressed how other authors find a similar correlation, but it cannot be confirmed (Osterbrock, 1977; Phillips, 1978a; Koski, 1978; Heckman & Balick, 1979). The reason is related to the errors included in these measures. In the same way, can be useful to include the errors in the current treatment to obtain more solid conclusions.

In Figure 2.22 panel (a) are presented the results for the possible relations between the calculated densities and the redshift or the S/N ratio. In the same plots we have also the linear regressions. As we can clearly see, in both the cases there is not an

important correlation between the listed quantities. As a consequence the obtained values should not include systematic errors or biases. The same can be done for T_e, the outcome is presented in panel (b) of Figure 2.22. As previously, the linear regression does not identify a significant trend in the data. Also in this case we can assume the absence of biases fairly accurately in these results. The values for the statistical tests for the $z - N_e$ comparison are: $(r_p, p - value) = (0.08, 5.62 \cdot 10^{-1})$, $(r_s, p - value) = (0.05, 7.29 \cdot 10^{-1})$, and $(r_k, p - value) = (0.03, 7.44 \cdot 10^{-1})$. For $S/N - N_e$: $(r_p, p - value) = (0.14, 3.24 \cdot 10^{-1})$, $(r_s, p - value) = (0.02, 8.69 \cdot 10^{-1})$, and $(r_k, p - value) = (0.02, 8.61 \cdot 10^{-1})$. The same statistical tests were produced for the temperature, starting with $z - T_e$: $(r_p, p - value) = (-0.12, 4.24 \cdot 10^{-1})$, $(r_s, p - value) = (-0.11, 4.63 \cdot 10^{-1})$, and $(r_k, p - value) = (-0.07, 4.98 \cdot 10^{-1})$. Finally for $S/N - T_e$: $(r_p, p - value) = (-0.04, 7.69 \cdot 10^{-1})$, $(r_s, p - value) = (-0.02, 8.84 \cdot 10^{-1})$, and $(r_k, p - value) = (-0.01, 9.53 \cdot 10^{-1})$.

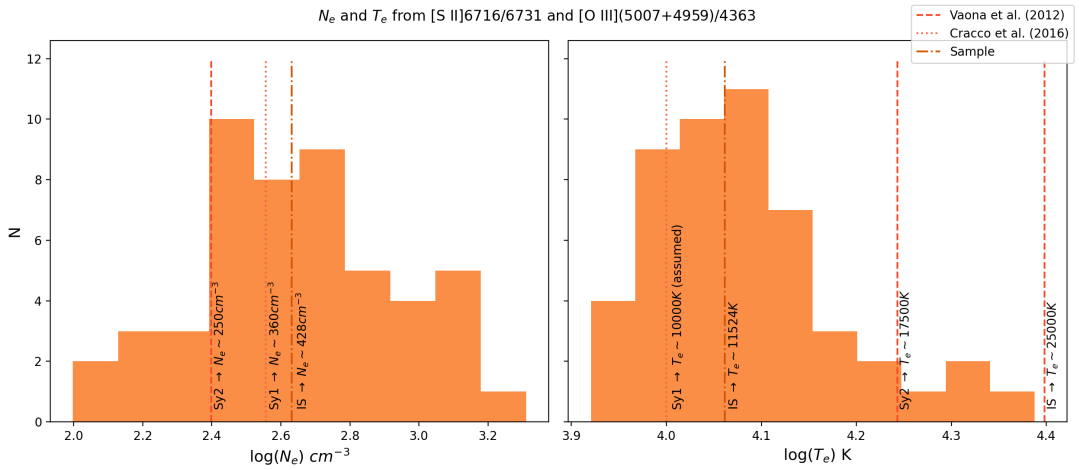

(a)

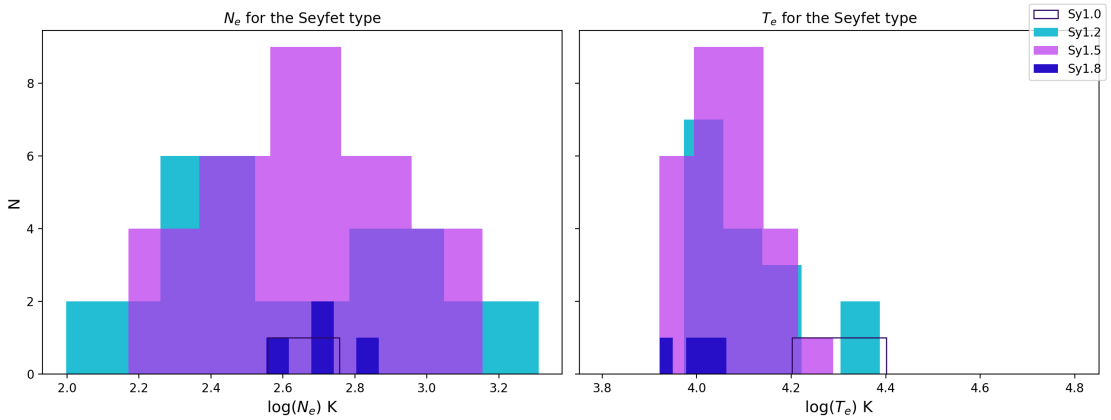

(b)

Figure 2.20: (a) Results from the calculation of Ne and Te for the sample. In the left panel the densities with the median value and the comparison with respect to Vaona et al. (2012) and Cracco et al. (2016). In the right panel, the same as for the densities but for the temperatures. (b) Comparison between the results of N_e and T_e divided for the Seyfert type according to the Whittle (1992) method (see section 1.2.2).

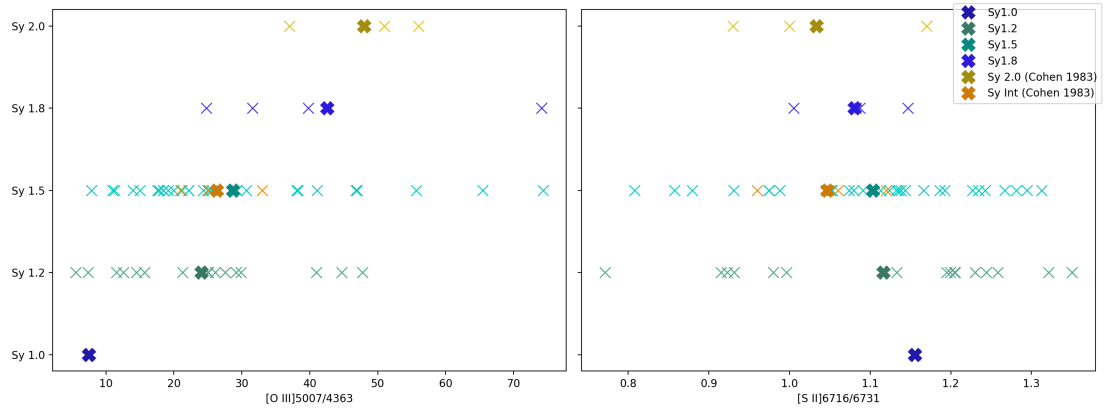

Figure 2.21: (a) Distribution for the results of [O III]5007/4363 divided for the Seyfert type using the same method as before. The blue crosses represent the outcome for our sample, while the yellow and orange ones comes from Cohen (1983). They consider IS as a whole class, as a consequence their results are put together with the Sy1.5 of our sample. (b) The same as for panel (a), but for [S II]6716/6731.

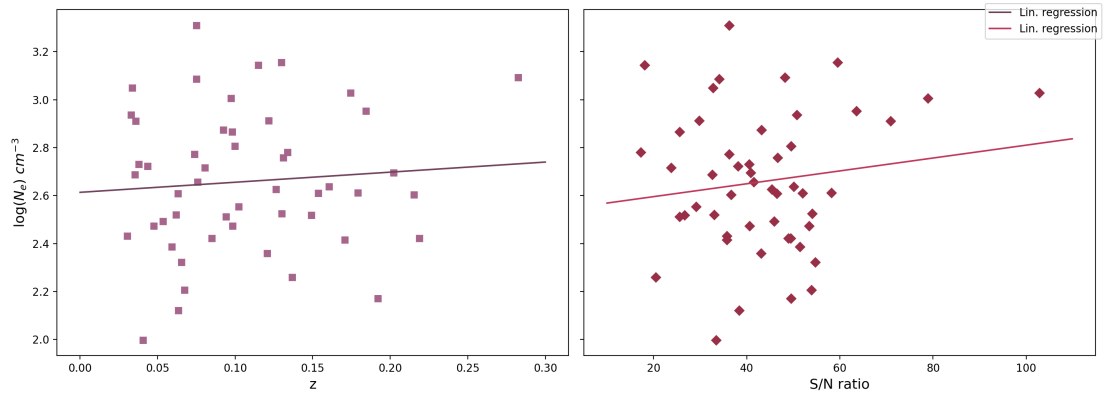

(a)

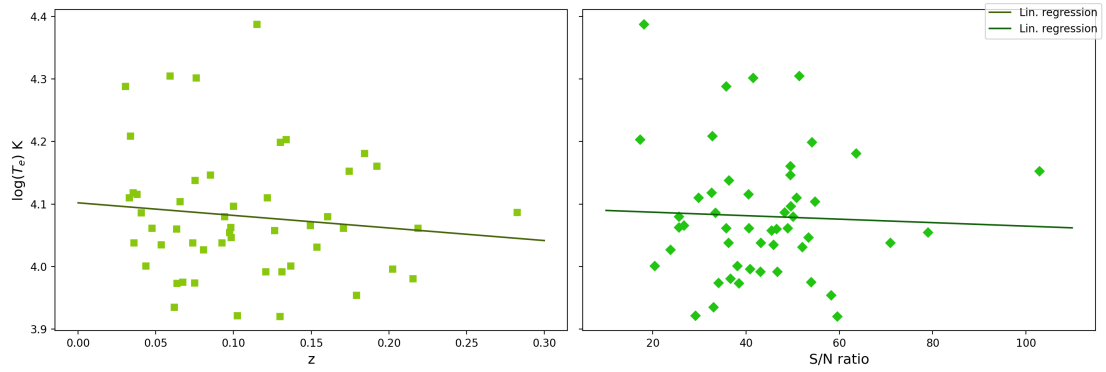

(b)

Figure 2.22: (a) Relations between the calculated densities with the redshift and the S/N ratio. No clear trend is visible. (b) The same as for panel (a), but for the temperatures. Also here no trend can be easily recognize.

Chapter 3

Summary and conclusions

The present work concentrates on a sample of 50 IS, almost equally divided between Sy1.2 and Sy1.5. The spectrum of these sources, characterized by high S/N ratios ($\sim$43), was studied is its main emission lines to obtain physical quantities as $A(V)$, $L_{[OIII]}$, $L_{H\alpha}$, L_{bol}, M_{BH}, $\dot{M}$, N_e, and T_e. Through single or multiple Gaussian functions we were able to reproduce the emission profiles, both in their broad and narrow components. Some relations between the parameters were exploited to get a controlled fit. In particular: the central displacement with respect to the rest frame wavelength, the width of the components, and the transition probability. The sample was divided in two groups according to the number of Gaussians employed in the Hβ profile. Normal profiles present 3 curves which are related to a simple narrow component and a broad one formed by two Gaussians. Pathological spectra, instead, are characterized by multiple bumps forming a possible disk emission or outflow from the BLR. Unfortunately, *WISEA J164819.02+302210.8* and *WISEA J084205.57 +075925.5* are fitted in an inappropriate way due to the difficulty in the process.
The data analysis starts with the production of velocity diagrams where the wavelength is converted in km s^{-1} through Equation 2.1. The results show how the BLR profile in Hα and Hβ tends to superimpose correctly. The same for the narrow emission in Hα and [O III]. Then diagnostic diagrams were exploited, in particular: O_{123}, BPT & VO, and [O I]/Hα vs [O III]/[O II]. From all these plots we can distinguish

between Seyferts, LINERs, and starburst galaxies. Comparing the FWHM of the two main Balmer lines we inferred some properties about the extra added components in the pathological cases. Then we performed a sub-classification of IS according to Whittle (1992) and Netzer (1990) methods. Exploiting this separation, all the other properties were divided according to the Seyfert type. These quantities are: $A(V)$ and the Balmer decrement, the Hα and [O III] luminosity, M_{BH}, $\dot{M}$, N_e, and T_e. The first shows a small difference between Sy1.2 and Sy1.5. The same for $L_{H\alpha}$ vs $L_{[OIII]}$. The black hole mass calculated through R_{BLR} is a lower limit, as the UM foresee. The Eddington ratio is comparable to the other Seyferts. These two last points should also consider the host galaxy effect on L_{cont} which increases the sole contribution made by the AGN. Finally, both [O III](4959+5007)/4363 and [S II]6716/6731 show trends according to the Seyfert type. Particularly, the oxygen lines ratio increases from Sy1 to Sy2, while the sulfur lines one decreases. Nagao et al (2001) verify these dependence showing an important significance in the case of [O III] and a small or not systematic relation for [S II]. As a consequence, also our results should be confirmed through the error and statistical analysis.

From the results that we obtained, we can list the outcomes in favour of the UM. The extinction (see Section 2.7.1) measured in Sy1.2 and Sy1.5 shows a trend that corroborates the inclination-dependent framework. In particular Sy1.2 have $A(V) \sim 1.19$, while Sy1.5 have $A(V) \sim 1.24$, both the two values represent the average. If we take the median we have $A(V) \sim 1.12$ and $A(V) \sim 0.90$ respectively. Assuming that the difference of these values is real, the increasing behavior of the average can be explained in terms of an increasing obscuration of the central emission due to the torus. In Sy1.2 the primary radiation is less blocked with respect Sy1.5. On the contrary, the median gives an opposite trend which cannot be interpreted in favour of the UM. About the Balmer decrement, the comparison between our results and other studies (Cohen, 1983; Binette et al., 1990; Nagao et al., 2001) gives a compatibility with the case B recombination reference. Further, Nagao stressed the presence of a possible trend in the Hα/Hβ vs Hγ/Hβ plot. Sy1 are in the upper part of the diagram, Sy2 in the lower part, and IS in between the two (see Figure 2.16). From this point of view we can state that Sy1 and 2 are linked through IS, as can

be inferred from Nagao results. Another sequence trend of the type Sy1-IS-Sy2 is visible in Figure 2.17 in the last panel. Here the comparison is expressed in terms of the luminosities of Hα and [O III]. The separation between the Seyferts in the y-axis (Sy1 in the lower part and Sy1.8 in the higher one) can be highly related to the classification method adopted (Whittle, 1992). Indeed this sorting exploits [O III] and Hβ, while the plot relates [O III] and Hα. Due to the link between the Balmer lines, the hydrogen-oxygen luminosity trend can be the consequence of the adopted method. Comparing Hβ and Hα directly (mid panel of the same figure), there is a relation between the two lines. The black hole mass, instead, confirms the UM prediction. In two of the three methods (Greene and Koski) it is exploited the virial theorem through Equation 1.3. As a consequence, due to the partial visibility of the BLR, the M_{BH} for our sample results to be a lower limit to the real value. This can be inferred from the comparison between the masses with the only source of our sample for which a reverberation mapping estimation is present, Mrk 110. The third method, instead, is related to [O III]. In this case the discrepancy between the reverberation mapping value and the calculated one is smaller, but still around one order of magnitude. Furthermore, the [O III] method seems to be biased as we can see form Figure 2.18 in the last panel. If Hβ-based masses spread in the whole x-axis, the y-axis values are concentrated around $log(M_{BH}) \sim 7.7$. Finally, the electron density and temperature are comparable with other studies concentrated on Sy1 and Sy2 samples (Vaona et al., 2012; Cracco et al., 2016). Some authors compared these classes in terms of N_e and T_e (Bennert et al., 2006). They obtained a similarity in terms of the density around 10^3 cm^{-3}, which is slightly addressed to our median value of 430 cm^{-3}, but within the distribution. For the temperatures they showed a discrepancy: (33590$\pm$7070)K for Sy1 and (14470$\pm$440)K for Sy2. According to this separation in terms of the temperature, our results are similar to the Sy2 ones. This cannot be explained by the nature of the selected sample. Finally, comparing the two line ratios used in the N_e and T_e calculus we can see a clear trend (see Figure 2.21). The sulfur lines ratio decreases with the Seyfert type, while the oxygen lines one increases. This can be an interesting point to deepen, but we should include more sources in the study, adding also Sy1.8/1.9.

Altogether IS present different properties in between the other Seyfert classes. As a consequence the UM seems to foresee quite well the outcomes, even if the other possibilities should not be ruled out. In particular we are speaking about the disk luminosity and the presence of obscuring filaments. Though the latter has not so many proof in favour, as Trippe et al. (2010) show. About the similarity between IS and the other Seyferts we can state that this heterogeneous class of sources behaves in a continuous way. Consequently Sy1 samples can also include Sy1.2 and Sy1.5, but should keep attention on the higher types. On the contrary, Sy1.8 and Sy1.9 can be added to Sy2 sources, while the lower classes should be eliminated.

3.1 Future work

As a final point we can list some of the possible next steps related to this work. One of the most important, in order to have more reliable results, is the error analysis. This can be operated adding a Gaussian noise to lines proportional to the continuum one. In this way the spectral fitting of the emission features will be repeated, for example for N=100 times, obtaining a distribution for the fit parameters. Once we have the distribution we can get the median and the standard deviation to use in the data analysis. Another point is to obtain a O_{123} diagram also for Sy1, to compare the three main classes of Seyfert and understand if there are some differences to exploit in the classification. This could be a possible implementation to the automatic classifier developed by Peruzzi et al. (2021). Related to this possibility, we should also consider a larger statistical base of IS formed by $\gg$50 sources. This will produce a more heterogeneous sample in terms of IS types and as a consequence more reliable outcomes for each group. Finally, a detailed study of the BLR emission is needed. In some of the selected sources, the pathological cases, this component was characterized by multiple bumps. Some of them show a probable disk emission which produces two curves with different intensity. From the disk fitting one can have insights on the inclination of this component and, for example, confirm this structure for the BLR. Alternatively other models can be adopted, e.g. a spherically symmetric structure or a bipolar flow (Romano et al., 1996). None of these possibilities is completely

confirmed or rejected, so a detailed study can lead to meaningful conclusions.
The world of AGN is formed by a variety of different sources. IS are an important group of this family, even if often forgotten. Specific studies on these Seyferts can add different points of view on the AGN class giving a more complete understanding of the galaxies formation, structure, and evolution.

References

- Antonucci R. (1993), *"Unified Models for Active Galactic Nuclei and Quasars."*, Annu. Rev. Astron. Astrophys., 31, pp. 473-521.

- Antonucci R. & Miller J.S. (1985), *"Spectropolarimetry and the nature of NGC 1068."*, The Astrophysical Journal, 297, pp. 621-632.

- Baldwin J.A. et al. (1981), *"Classification parameters for the emission-line spectra of extragalactic objects."*, Publications of the Astronomical Society of the Pacific, 93.551, pp. 5.

- Benítez E. et al. (2012), *"Characterization of a sample of intermediate-type AGN. I. spectroscopic properties and serendipitous discovery of new dual AGN."*, The Astrophysical Journal, 763.1, pp. 36.

- Bennert N. et al. (2006), *"Size and properties of the narrow-line region in Seyfert-1 galaxies from spatially-resolved optical spectroscopy."*, Astronomy & Astrophysics, 459.1, pp. 55-69.

- Berton M. et al. (2015), *"Parent population of flat-spectrum radio-loud narrow-line Seyfert 1 galaxies."*, Astronomy & Astrophysics 578, pp. A28.

- Berton M. et al. (2020), *"Line shapes in narrow-line Seyfert 1 galaxies: a tracer of physical properties?."*, arXiv preprint arXiv:1909.12343.

- Berton M. et al. (2021), *"Hunting for the nature of the enigmatic narrow-line Seyfert 1 galaxy PKS 2004-447."*, Astronomy & Astrophysics, 654, pp. A125.

- Berton M. & Järvelä E. (2021), *"Peaked sources and narrow-line Seyfert 1s: A love story."* Astronomische Nachrichten, 342.9-10, pp. 1066-1070.

- Binette L. et al. (1990), *"Balmer decrements in Seyfert 2 galaxies." Publications of the Astronomical Society of the Pacific*, 102.653, pp. 723.

- Cardelli J.A. et al (1989), *"The relationship between infrared, optical, and ultraviolet extinction."*, The Astrophysical Journal, 345,pp. 245-256.

- Chen S. et al. (2018), *"Probing narrow-line Seyfert 1 galaxies in the southern hemisphere."*, Astronomy & Astrophysics 615 (2018): A167.

- Cohen R.D. (1983), *"The narrow-line region of intermediate Seyfert galaxies."*, The Astrophysical Journal, 273, pp. 489-504.

- Collin S. & Kawaguchi T. (2004), *"Super-Eddington accretion rates in Narrow Line Seyfert 1 galaxies."* , Astronomy & Astrophysics, 426.3, pp. 797-808.

- Cracco V. et al. (2016), *"A spectroscopic analysis of a sample of narrow-line Seyfert 1 galaxies selected from the Sloan Digital Sky Survey."*, Monthly Notices of the Royal Astronomical Society, 462.2, pp. 1256-1280.

- Decarli R. et al. (2008), *"Are the black hole masses in narrow-line Seyfert 1 galaxies actually small?."*, Monthly Notices of the Royal Astronomical Society, 386.1, pp. L15-L19.

- Deo R.P. et al. (2007), *"Spitzer IRS observations of Seyfert 1.8 and 1.9 galaxies: a comparison with Seyfert 1 and Seyfert 2."*, The Astrophysical Journal 671.1, pp. 124.

- Deo R. P. et al. (2009), *"The mid-infrared continua of Seyfert galaxies."*, The Astrophysical Journal, 705.1, pp. 14.

- Dermer C.D. & Giebels B. (2016), *"Active galactic nuclei at gamma-ray energies."*, Comptes Rendus Physique, 17.6, pp. 594-616.

- Dojčinović I. et al. (2022), *"The flux ratio of the [N II] λλ 6548, 6583 Å lines in sample of Active Galactic Nuclei Type 2."*, Advances in Space Research.

- Greene J.E. et al. (2010), *"The lick AGN monitoring project: Alternate routes to a broad-line region radius."*, The Astrophysical Journal, 723.1, pp. 409.

- Elitzur M. et al. (2014), *"Evolution of broad-line emission from active galactic nuclei."*, Monthly Notices of the Royal Astronomical Society, 438.4, pp. 3340-3351.

- Guolo M. et al. (2021), *"The Eddington ratio-dependent 'changing look' events in NGC 2992."*, Monthly Notices of the Royal Astronomical Society, 508.1, pp. 144-156.

- Hao L. et al. (2007), *"The distribution of silicate strength in spitzer spectra of AGN and ULIRGs."*, The Astrophysical Journal, 655.2, pp. L77.

- Heckman T. M. & Balick B. (1979), *"Physical conditions in the narrow line region in active galaxies and quasars."*, Astronomy and Astrophysics, 79, pp. 350-353.

- Hernández-García L. et al. (2017), *"X-ray variability of Seyfert 1.8/1.9 galaxies."*, Astronomy & Astrophysics 602, pp. A65.

- Hickox R.C. & Alexander D.M. (2018), *"Obscured Active Galactic Nuclei."*, Annu.Rev. Astron. Astrophys., arXiv:1806.04680v1.

- Ho L.C. & Kim M. (2014), *"The black hole mass scale of classical and pseudo bulges in active galaxies."*, The Astrophysical Journal, 789.1, pp. 17.

- Järvelä E. (2018), *"Narrow-line Seyfert 1 galaxies - Observational and statistical analysis."*

- Järvelä E. et al. (2020), *"SDSS J211852. 96-073227.5: The first non-local, interacting, late-type intermediate Seyfert galaxy with relativistic jets."*. Astronomy & Astrophysics, 636, pp. L12.

- Jarvis M.E. et al. (2021), *"The quasar feedback survey: discovering hidden Radio-AGN and their connection to the host galaxy ionized gas."*, Monthly Notices of the Royal Astronomical Society, 503.2, pp. 1780-1797.

- Ji X. et al. (2020), *"Upper boundaries of active galactic nucleus regions in optical diagnostic diagrams."*, Monthly Notices of the Royal Astronomical Society, 496.2, pp. 1262-1277.

- Kaspi S. et al. (2000), *"Reverberation measurements for 17 quasars and the size-mass-luminosity relations in active galactic nuclei."*, The Astrophysical Journal, 533.2, pp. 631.

- Kauffmann G. et al. (2003), *"The host galaxies of active galactic nuclei."*, Monthly Notices of the Royal Astronomical Society, 346.4, pp. 1055-1077.

- Kewley L.J. et al. (2006), *"The host galaxies and classification of active galactic nuclei."*, Monthly Notices of the Royal Astronomical Society, 372.3, pp. 961-976.

- Khachikian E.Y. & Weedman, D.W. (1974), *"An Atlas of Seyfert Galaxies."*, The Astrophysical Journal, 192, pp. 581-589, http://dx.doi.org/10.1086/153093.

- Komossa S. (2007), *"Narrow-line Seyfert 1 galaxies."*, arXiv preprint arXiv:0710.3326.

- Komossa S. (2018), *"Multi-wavelength properties of radio-loud Narrow-line Seyfert 1 galaxies."*, arXiv preprint arXiv:1807.03666.

- Koski A.T. (1978), *"Spectrophotometry of Seyfert 2 galaxies and narrow-line radio galaxies."*, The Astrophysical Journal, 223, pp. 56-73.

- Landt H. et al. (2016), *"A physical classification scheme for blazars."*, Monthly Notices of the Royal Astronomical Society, 351.1, pp. 83-100.

- Lusso E. & Risaliti G. (2016), *"The tight relation between X-ray and ultraviolet luminosity of quasars."*, The Astrophysical Journal, 819.2, pp. 154.

- Nagao T. et al. (2001), *"Seyfert-type dependences of narrow emission-line ratios and physical properties of high-ionization nuclear emission-line regions in Seyfert galaxies."*, Publications of the Astronomical Society of Japan, 53.4, pp. 629-645.

- Nelson C.H. & Whittle M. (1996), *"Stellar and Gaseous Kinematics of Seyfert Galaxies. II. The Role of the Bulge."*, The Astrophysical Journal, 465, pp. 96.

- Netzer H. (1990), *Active Galactic Nuclei*, Saas-Fee Advanced Course, 20 (Springer), pp. 57.

- Osterbrock D. E. (1977), *"Spectrophotometry of Seyfert 1 galaxies."*, The Astrophysical Journal, 215, pp. 733-745.

- Osterbrock D.E. (1981), *"Seyfert galaxies with weak broad H alpha emission lines."*, The Astrophysical Journal, 249, pp. 462-470.

- Osterbrock D.E. et al. (1992), *"Near-infrared spectra and classification diagnostics of Seyfert galaxies."*, The Astrophysical Journal, 389 (1992): 196-207.

- Pérez-Torres M.A. & Alberdi A. (2007), *"Radio emission from the Sy 1.5 galaxy NGC 5033."*, Monthly Notices of the Royal Astronomical Society, 379.1, pp. 275-281.

- Peruzzi T. et al. (2021), *"Interpreting automatic AGN classifiers with saliency maps."*, Astronomy & Astrophysics, 652, pp. A19.

- Phillips M. M. (1978a), *"Permitted fe II Emission in Seyfert 1 Galaxies and QSOs I. Observations."*, The Astrophysical Journal Supplement Series, 38, pp. 187.

- Piconcelli E. et al. (2006), *"4U 1344-60: a bright intermediate Seyfert galaxy at z= 0.012 with a relativistic Fe Kα emission line."*, Astronomy & Astrophysics, 453.3, pp. 839-846.

- Porquet D. et al. (2021), *"The first simultaneous X-ray broadband view of Mrk*

110 with XMM-Newton and NuSTAR.", Astronomy & Astrophysics, 654, pp. A89.

- Quillen A.C. et al. (2000), *"The Variability of Seyfert 1.8 and 1.9 Galaxies at 1.6 microns."*, The Astrophysical Journal, 532.1, pp. L17.

- Ramos Padilla A.F. et al. (2021), *"The viewing angle in AGN SED models: a data-driven analysis."*, Monthly Notices of the Royal Astronomical Society, 510.1, pp. 687-707.

- Robson Ian (1996), *"Active Galactic Nuclei."*, Wiley-Praxis Series in Astronomy & Astrophysics, pp. 75-85-155-160-166-229.

- Romano P. et al. (1996), *"On the wings of broad Ha emission in active galactic nuclei."* Monthly Notices of the Royal Astronomical Society, 279.1, pp. 165-170.

- Sijacki D. et al. (2007), *"A unified model for AGN feedback in cosmological simulations of structure formation."*, Monthly Notices of the Royal Astronomical Society, 380.3, pp. 877-900.

- Stern J. & Laor A. (2012), *"Type 1 AGN at low z–II. The relative strength of narrow lines and the nature of intermediate type AGN."*, Monthly Notices of the Royal Astronomical Society, 426.4, pp. 2703-2718.

- Trippe M.L. et al. (2010), *"A multi-wavelenght study of the nature of type 1.8/1.9 Seyfert Galaxies."*, The Astrophysical Journal, 725.2, pp. 1749.

- Ulvestad J.S. (1986), *"Radio properties of type 1.8 and 1.9 Seyfert galaxies."*, The Astrophysical Journal, 310, pp. 136-144.

- Vaona L. et al. (2012), *"Spectral properties of the narrow-line region in Seyfert galaxies selected from the SDSS-DR7."*, Monthly Notices of the Royal Astronomical Society, 427.2, pp. 1266-1283.

- Veilleux S. & Osterbrock D.E. (1987), *"Spectral classification of emission-line galaxies."*, The Astrophysical Journal Supplement Series, 63, pp. 295-310.

- Weedman D.W. (1977), *"Seyfert galaxies."*, Annual review of astronomy and astrophysics, 15.1, pp 69-95.

- Whittle M. (1992), *"Virial and jet-induced velocities in Seyfert galaxies. I-A compilation of narrow line region and host galaxy properties."*, The Astrophysical Journal Supplement Series, 79, pp. 49-75.

Appendix A

Tables

In Table A.1 the list of the selected objects with the coordinates (RA, DEC), the redshift (z), the signal to noise ratio (S/N), and the extinction (A_V). See http://ned.ipac.caltech.edu. In Table A.2 the list of the results for the electron densities (N_e) and temperatures (T_e). In Tables A.3, A.4, A.5, A.6, A.7, and A.8 the list of the parameters (amplitude A, center x_0, and width w) from the fits of Hα, Hβ, [O III]λ5007, [O III]λ4959, [O II]λ3727, [N II]λ6583, [O I]λ6300, [S II]λ6716, and [S II]λ6731.

Name	**RA**	**DEC**	**z**	**S/N**	**A$_V$**
WISEA J123022.17+662154.6	187.59241	66.36516	0.18435	63.56121	0.03900
UM 614	207.47018	2.07919	0.03284	50.77165	0.03288
MRK 1392	226.48565	3.70731	0.03590	70.92879	0.03588
WISEA J235654.30-101605.4	359.22627	-10.26819	0.07376	36.23836	0.08800
MRK 0110	141.30355	52.28620	0.03529	32.57561	0.03529
WISEA J211646.34+110237.4	319.19308	11.04378	0.08057	23.77619	0.21600
WISEA J101043.35+061201.4	152.68070	6.20040	0.09815	25.56018	0.06800
WISEA J115341.16+101754.0	178.42152	10.29832	0.16057	50.08462	0.08300
MRK 0699	245.94119	41.08233	0.03355	32.72050	0.03383
WISEA J133120.18+484013.9	202.83413	48.67050	0.12153	29.77357	0.01800
SBS 1340+569	205.54213	56.70285	0.04057	33.39606	0.04045

WISEA J164819.02+302210.8	252.07926	30.36968	0.10228	29.14466	0.10200
[HB89] 1612+261	243.55501	26.07117	0.13095	46.65839	0.13095
WISEA J165551.37+214601.7	253.96405	21.76716	0.15361	51.99344	0.15600
FBQS J081738.3+242330	124.40973	24.39169	0.28258	48.2266	0.28233
WISEA J084205.57+075925.5	130.52322	7.99044	0.13374	17.24651	0.20200
WISEA J111907.07+413014.5	169.77942	41.50406	0.09421	25.56937	0.06100
WISEA J105635.05+414602.6	164.14608	41.76738	0.20226	40.84957	0.03700
B3 0745+453	117.27712	45.17609	0.19215	49.49006	0.19216
CGCG 244-033	189.21325	45.65116	0.03043	35.73969	0.03034
WISEA J104326.47+110524.2	160.86031	11.09008	0.04753	40.59312	0.07500
WISEA J114347.71+112847.8	175.94879	11.47998	0.12056	43.04564	0.10200
WISEA J134548.50+114443.5	206.45211	11.74543	0.12636	45.40011	0.07000
FBQS J1610+3303	242.69887	33.06042	0.09735	78.93261	0.09733
WISEA J114434.72+070516.5	176.1447	7.08792	0.07492	34.06042	0.05000
2MASS J12421060+3317027	190.54421	33.28406	0.04355	38.0927	0.21093
WISEA J133624.05+391731.1	204.10027	39.29197	0.17913	58.21838	0.01200
MRK 0646	181.45779	35.17943	0.05347	45.87068	0.05354
VIII Zw 327	204.78558	11.9817	0.09240	43.15578	0.09247
WISEA J091848.61+211717.0	139.70255	21.28807	0.14925	26.6297	0.10100
MRK 1220	133.6635	17.68955	0.06546	54.75265	0.06521
SDSS J104427.75+271806.3	161.11564	27.30175	0.07580	41.48977	0.07582
[HB89] 1142+310	176.29278	30.78812	0.05906	51.3945	0.05897
FBQS J1227+3214	1186.95475	32.2497	0.13683	20.4339	0.13663
WISEA J090723.56+171616.3	136.84816	17.27121	0.09831	53.37177	0.10000
WISEA J161745.63+060353.5	244.44015	6.06487	0.03788	40.52492	0.15200
WISEA J100438.82+151057.0	151.16177	15.18261	0.21875	48.90891	0.09300
PG 1138+222	175.31734	21.93939	0.06323	46.48263	0.06329
WISEA J124800.54+100958.9	192.00226	10.16638	0.11500	18.08488	0.06400
WISEA J121224.89+185920.2	183.10377	18.98894	0.21535	36.64762	0.08200
MRK 0783	195.74514	16.40772	0.06727	53.9232	0.06739
WISEA J132213.38+214721.1	200.55579	21.7892	0.08495	49.43757	0.06400

WISEA J134915.20+220032.6	207.31334	22.00909	0.06187	32.98677	0.06900
SBS 1527+564	232.28107	56.26853	0.09978	49.52855	0.09968
WISEA J145842.74+213609.9	224.67809	21.60277	0.06343	38.41075	0.10900
WISEA J152558.53+181416.0	231.4939	18.23781	0.13006	54.08919	0.18700
WISEA J152753.80+061018.9	231.9742	6.17192	0.17433	102.82724	0.11900
WISEA J145434.34+080336.7	223.64313	8.0602	0.12984	59.50144	0.07500
WISEA J150913.78+175710.1	227.30750	17.95279	0.17058	35.71925	0.07400
VII Zw 533	208.92816	64.67916	0.07514	36.26383	0.03700

Table A.1

Name	**N_e in cm^{-3}**	**T_e in K**
WISEA J123022.17+662154.6	898	151823
UM 614	865	12880
MRK 1392	814	10914
WISEA J235654.30-101605.4	593	10919
MRK 0110	487	13127
WISEA J211646.34+110237.4	520	10645
WISEA J101043.35+061201.4	735	11550
WISEA J115341.16+101754.0	433	12025
MRK 0699	1118	16173
WISEA J133120.18+484013.9	818	12880
SBS 1340+569	100	12201
WISEA J164819.02+302210.8	2358	8345
[HB89] 1612+261	574	9814
WISEA J165551.37+214601.7	407	10751
FBQS J081738.3+242330	1238	12212
WISEA J084205.57+075925.5	603	15969
WISEA J111907.07+413014.5	325	12021
WISEA J105635.05+414602.6	496	9908
B3 0745+453	148	14484
CGCG 244-033	270	19427

WISEA J104326.47+110524.2	297	11518
WISEA J114347.71+112847.8	229	9819
WISEA J134548.50+114443.5	422	11425
FBQS J1610+3303	1014	11337
WISEA J114434.72+070516.5	1221	9425
2MASS J12421060+3317027	528	10028
WISEA J133624.05+391731.1	408	9000
MRK 0646	311	10840
VIII Zw 327	748	10924
WISEA J091848.61+211717.0	330	11628
MRK 1220	210	12706
SDSS J104427.75+271806.3	454	20026
[HB89] 1142+310	244	20190
FBQS J1227+3214	182	10030
WISEA J090723.56+171616.3	297	11138
WISEA J161745.63+060353.5	537	13062
WISEA J100438.82+151057.0	264	11529
PG 1138+222	406	11483
WISEA J124800.54+100958.9	1396	24412
WISEA J121224.89+185920.2	401	9571
MRK 0783	161	9451
WISEA J132213.38+214721.1	264	14019
WISEA J134915.20+220032.6	331	8618
SBS 1527+564	640	12497
WISEA J145842.74+213609.9	132	9404
WISEA J152558.53+181416.0	335	15804
WISEA J152753.80+061018.9	1067	14217
WISEA J145434.34+080336.7	1428	8330
WISEA J150913.78+175710.1	261	11518
VII Zw 533	2043	13742

Table A.2

Name	$\mathbf{A}_n$	$\mathbf{x}^0_n$	$\mathbf{w}_n$	$\mathbf{A}_{b1}$	$\mathbf{x}^0_{b1}$	$\mathbf{w}_{b1}$	$\mathbf{A}_{b2}$	$\mathbf{x}^0_{b2}$	$\mathbf{w}_{b2}$	$\mathbf{A}_{e1}$	$\mathbf{x}^0_{e1}$	$\mathbf{w}_{e1}$	$\mathbf{A}_{e2}$	$\mathbf{x}^0_{e2}$	$\mathbf{w}_{e2}$
WISEA J123022.17+662154.6	104.92	6565.08	2.9	166.38	6567.56	38.19	77.5	6561.77	9.58	29.04	6581.28	3.57	19.11	6480.35	22.58
UM 614	315.63	6563.99	2.57	249.63	6564.27	28.38	222.87	6563.22	7.39	56.3	6600.93	40.0	-	-	-
MRK 1392	573.83	6564.18	3.59	481.81	6562.4	41.34	181.19	6566.87	10.05	23.78	6513.0	4.0	17.93	6543.0	4.0
WISEA J235654.30-101605.4	252.52	6564.53	3.38	210.7	6568.52	31.06	205.74	6564.43	8.27	-	-	-	-	-	-
MRK 0110	789.84	6563.79	3.08	348.95	6575.47	32.11	593.31	6564.5	12.23	-	-	-	-	-	-
WISEA J211646.34+110237.4	318.86	6564.87	3.05	81.27	6564.3	9.79	-	-	-	70.22	6545.0	50.0	18.07	6619.0	17.0
WISEA J101043.35+061201.4	175.82	6564.88	4.27	66.29	6552.63	26.02	44.18	6563.44	11.25	-	-	-	-	-	-
WISEA J115341.16+101754.0	113.11	6567.42	3.64	134.8	6562.0	32.2	120.03	6564.92	16.81	-	-	-	-	-	-
MRK 0699	501.98	6566.68	2.49	211.39	6553.54	21.01	379.7	6570.14	5.57	12.31	6504.0	11.65	19.71	6617.0	20.0
WISEA J133120.18+484013.9	151.27	6563.5	2.66	9.67	6571.46	46.71	147.24	6566.88	18.54	-	-	-	-	-	-
SBS 1340+569	290.74	6564.88	1.7	76.58	6562.96	25.3	-	-	-	-	-	-	-	-	-
WISEA J164819.02+302210.8	56.93	6566.76	3.21	174.17	6563.58	10.26	-	-	-	-	-	-	-	-	-
[HB89] 1612+261	581.31	6563.49	3.81	564.22	6563.69	22.88	-	-	-	75.16	6611.57	31.72	24.74	6509.02	15.18
WISEA J165551.37+214601.7	435.85	6563.37	4.42	497.26	6562.93	16.26	-	-	-	202.68	6581.41	32.52	73.84	6530.35	36.31
FBQS J081738.3+242330	106.68	6562.82	4.45	139.67	6560.79	29.48	-	-	-	20.51	6635.91	27.47	-	-	-
WISEA J084205.57+075925.5	139.07	6564.59	3.1	136.0	6585.44	19.67	84.76	6562.15	10.11	58.05	6455.0	26.33	91.42	6518.0	26.89
WISEA J111907.07+413014.5	225.99	6564.19	4.1	106.82	6566.35	33.3	-	-	-	-	-	-	-	-	-
WISEA J105635.05+414602.6	246.42	6564.44	7.31	94.09	6559.98	51.01	-	-	-	-	-	-	-	-	-
B3 0745+453	104.19	6564.05	2.46	150.63	6564.58	39.5	51.17	6563.09	7.29	42.47	6570.12	6.48	16.22	6636.53	35.0
CGCG 244-033	103.02	6564.03	1.96	27.69	6575.42	29.05	170.81	6565.9	13.3	-	-	-	-	-	-
WISEA J104326.47+110524.2	752.31	6565.65	2.12	334.32	6555.86	39.63	-	-	-	58.3	6628.55	23.82	-	-	-
WISEA J114347.71+112847.8	160.75	6564.05	2.34	71.65	6566.04	35.8	25.82	6558.05	9.2	-	-	-	-	-	-
WISEA J134548.50+114443.5	67.44	6563.36	2.72	161.91	6567.78	34.21	46.09	6562.64	6.32	23.48	6610.01	10.0	-	-	-
FBQS J1610+3303	108.67	6565.41	3.48	285.27	6554.7	20.74	-	-	-	151.78	6595.73	17.71	-	-	-
WISEA J114434.72+070516.5	105.72	6563.94	3.08	83.79	6568.08	31.89	107.36	6561.0	12.73	-	-	-	-	-	-
2MASS J12421060+3317027	432.15	6566.83	3.26	165.41	6558.81	28.01	562.67	6567.94	11.75	35.02	6594.47	16.0	-	-	-
WISEA J133624.05+391731.1	190.11	6566.7	3.99	77.88	6564.94	44.58	27.82	6556.67	6.24	-	-	-	-	-	-
MRK 0646	443.74	6565.73	2.54	77.98	6571.1	30.42	87.64	6560.22	8.92	-	-	-	-	-	-
VIII Zw 327	74.86	6563.6	2.99	70.0	6567.79	30.39	113.61	6566.59	14.47	-	-	-	-	-	-
WISEA J091848.61+211717.0	101.23	6564.59	4.7	22.65	6551.15	27.82	208.04	6563.67	14.3	-	-	-	-	-	-
MRK 1220	758.61	6567.67	1.86	111.84	6561.94	38.3	203.82	6559.41	9.93	-	-	-	-	-	-
SDSS J104427.75+271806.3	221.44	6564.7	2.83	102.77	6565.84	29.7	-	-	-	-	-	-	-	-	-
[HB89] 1142+310	882.29	6566.61	1.86	177.28	6564.18	19.53	-	-	-	-	-	-	-	-	-
FBQS J1227+3214	203.05	6564.74	4.35	176.85	6564.91	18.06	-	-	-	-	-	-	-	-	-
WISEA J090723.56+171616.3	154.28	6563.55	2.73	44.94	6573.51	41.81	172.18	6564.79	18.58	-	-	-	-	-	-
WISEA J161745.63+060353.5	452.9	6564.26	3.34	291.48	6563.42	31.79	146.38	6562.89	9.55	24.43	6646.97	19.9	14.2	6511.03	4.98
WISEA J100438.82+151057.0	243.67	6565.0	3.14	77.87	6556.12	43.33	60.2	6574.97	18.9	-	-	-	-	-	-
PG 1138+222	1238.93	6564.9	2.35	196.94	6566.43	34.96	494.99	6566.17	14.29	-	-	-	-	-	-
WISEA J124800.54+100958.9	163.12	6564.16	2.45	57.75	6561.6	36.5	102.53	6564.36	11.34	-	-	-	-	-	-
WISEA J121224.89+185920.2	127.11	6562.59	2.52	64.69	6569.86	35.45	135.89	6564.67	16.69	-	-	-	-	-	-
MRK 0783	791.65	6562.88	3.81	232.83	6578.88	30.02	430.73	6564.21	12.63	-	-	-	-	-	-
WISEA J132213.38+214721.1	139.37	6565.32	1.97	49.47	6559.06	59.95	120.26	6565.99	6.4	-	-	-	-	-	-
WISEA J134915.20+220032.6	334.01	6564.89	3.71	176.84	6567.91	26.32	-	-	-	-	-	-	-	-	-
SBS 1527+564	282.46	6565.61	3.21	258.97	6558.91	30.56	148.89	6565.71	8.05	116.59	6585.68	15.62	-	-	-
WISEA J145842.74+213609.9	676.88	6565.45	1.91	58.24	6567.07	39.43	466.65	6562.72	10.88	104.52	6582.83	9.0	-	-	-
WISEA J152558.53+181416.0	212.39	6563.05	3.62	112.96	6564.25	27.0	212.39	6563.05	3.62	23.62	6600.41	33.75	-	-	-
WISEA J152753.80+061018.9	170.06	6562.99	3.42	355.79	6567.41	36.41	214.41	6563.53	14.28	-	-	-	-	-	-
WISEA J145434.34+080336.7	130.54	6562.72	4.7	94.52	6568.71	34.51	133.62	6557.61	14.59	-	-	-	-	-	-
WISEA J150913.78+175710.1	134.86	6566.05	2.72	26.32	6560.79	43.64	192.89	6565.9	17.83	-	-	-	-	-	-
VII Zw 533	397.35	6565.96	2.49	217.47	6564.9	28.5	166.22	6560.16	11.72	52.46	6579.44	7.27	-	-	-

Table A.3: List of the fit parameter used for the Hα line. The parameters are indicated with A for the amplitude, x^0 for the center, and w for the width. Using this last parameter the Gaussians are divided in narrow (n), broad 1 (b1), broad 2 (b2), extra 1 (e1), and extra 2 (e2).

Name	$\mathbf{A}_n$	$\mathbf{x}_n^0$	$\mathbf{w}_n$	$\mathbf{A}_{b1}$	$\mathbf{x}_{b1}^0$	$\mathbf{w}_{b1}$	$\mathbf{A}_{b2}$	$\mathbf{x}_{b2}^0$	$\mathbf{w}_{b2}$	$\mathbf{A}_{e1}$	$\mathbf{x}_{e1}^0$	$\mathbf{w}_{e1}$	$\mathbf{A}_{e2}$	$\mathbf{x}_{e2}^0$	$\mathbf{w}_{e2}$
WISEA J123022.17+662154.6	35.73	4863.67	2.15	55.46	4864.56	28.29	30.18	4860.36	7.1	4.76	4879.87	2.64	9.45	4807.73	15.41
UM 614	117.29	4862.58	1.9	58.54	4862.86	21.02	54.64	4861.81	5.47	15.66	4904.19	8.75	-	-	-
MRK 1392	215.94	4862.77	2.66	157.5	4860.99	30.62	33.41	4865.46	7.45	23.78	4821.0	4.31	17.93	4845.41	1.6
WISEA J235654.30-101605.4	112.03	4863.13	2.5	62.24	4867.11	23.01	49.94	4859.7	6.13	-	-	-	-	-	-
MRK 0110	309.5	4862.38	2.28	65.41	4874.06	23.79	69.06	4863.09	9.06	-	-	-	-	-	-
WISEA J211646.34+110237.4	112.37	4862.76	2.26	29.64	4862.89	7.25	-	-	-	15.24	4823.51	22.67	18.32	4880.0	22.01
WISEA J101043.35+061201.4	49.95	4863.47	3.16	7.24	4851.22	19.28	21.96	4862.03	8.33	-	-	-	-	-	-
WISEA J115341.16+101754.0	28.06	4863.69	2.69	58.52	4860.59	23.85	32.35	4863.51	12.45	-	-	-	-	-	-
MRK 0699	153.46	4863.97	1.84	65.45	4852.13	15.56	115.88	4866.28	4.12	12.1	4818.94	3.44	13.94	4902.05	5.85
WISEA J133120.18+484013.9	43.1	4862.09	1.97	9.25	4870.05	34.6	38.12	4863.42	13.73	-	-	-	-	-	-
SBS 1340+569	109.32	4862.77	1.26	29.51	4861.17	22.69	-	-	-	-	-	-	-	-	-
WISEA J164819.02+302210.8	34.18	4865.35	2.38	28.24	4862.17	7.6	-	-	-	-	-	-	-	-	-
[HB89] 1612+261	196.92	4862.08	2.82	170.69	4862.28	16.95	-	-	-	31.3	4905.0	20.0	7.88	4817.61	10.39
WISEA J165551.37+214601.7	161.12	4861.96	3.27	205.49	4861.52	16.9	-	-	-	36.84	4900.0	12.69	19.77	4818.94	10.82
FBQS J081738.3+242330	40.58	4861.31	3.3	36.78	4859.38	21.83	-	-	-	6.01	4909.17	12.89	-	-	-
WISEA J084205.57+075925.5	51.35	4863.19	2.29	15.23	4884.03	14.57	30.3	4860.74	7.49	6.04	4781.72	11.27	10.31	4826.87	17.22
WISEA J111907.07+413014.5	82.81	4862.78	3.04	17.52	4864.94	24.67	-	-	-	-	-	-	-	-	-
WISEA J105635.05+414602.6	80.8	4863.03	5.42	13.62	4847.04	31.61	-	-	-	-	-	-	-	-	-
B3 0745+453	38.99	4862.64	1.82	47.38	4863.18	29.26	20.02	4861.68	5.4	9.98	4878.71	4.8	6.36	4917.06	10.17
CGCG 244-033	34.74	4862.63	1.45	8.28	4874.01	21.52	46.9	4862.41	9.85	-	-	-	-	-	-
WISEA J104326.47+110524.2	293.95	4863.28	1.57	82.88	4854.45	32.55	-	-	-	21.76	4905.02	13.7	-	-	-
WISEA J114347.71+112847.8	51.34	4862.64	1.73	26.21	4864.63	26.52	5.31	4856.64	6.81	-	-	-	-	-	-
WISEA J134548.50+114443.5	25.27	4861.95	2.02	45.4	4864.7	25.34	17.84	4861.49	4.68	8.08	4895.6	8.07	-	-	-
FBQS J1610+3303	39.67	4862.68	2.58	79.61	4853.29	15.36	-	-	-	51.02	4884.21	15.0	-	-	-
WISEA J114434.72+070516.5	39.01	4862.53	2.28	32.61	4866.67	23.62	26.82	4859.59	9.43	-	-	-	-	-	-
2MASS J12421060+3317027	97.67	4864.07	2.41	33.4	4857.4	20.75	129.95	4863.95	8.7	15.1	4883.06	4.52	-	-	-
WISEA J133624.05+391731.1	44.48	4863.67	2.95	12.26	4858.45	24.12	5.81	4855.26	4.62	-	-	-	-	-	-
MRK 0646	148.84	4863.47	1.88	25.29	4869.69	22.54	21.63	4858.81	6.61	-	-	-	-	-	-
VIII Zw 327	30.62	4862.19	2.22	27.77	4866.38	22.51	25.59	4865.18	10.72	-	-	-	-	-	-
WISEA J091848.61+211717.0	14.76	4863.18	3.48	4.98	4849.74	20.6	33.86	4862.26	10.59	-	-	-	-	-	-
MRK 1220	165.0	4864.86	1.37	49.09	4860.53	28.37	29.0	4858.0	7.36	-	-	-	-	-	-
SDSS J104427.75+271806.3	58.21	4862.84	2.1	30.26	4862.38	25.65	-	-	-	-	-	-	-	-	-
[HB89] 1142+310	276.11	4863.92	1.37	64.2	4859.96	16.66	-	-	-	-	-	-	-	-	-
FBQS J1227+3214	44.42	4863.33	3.22	19.5	4862.08	13.37	-	-	-	-	-	-	-	-	-
WISEA J090723.56+171616.3	43.4	4862.14	2.02	30.21	4872.1	30.97	51.68	4861.23	13.76	-	-	-	-	-	-
WISEA J161745.63+060353.5	187.96	4862.85	2.47	71.9	4860.08	23.55	32.6	4861.61	7.08	13.18	4903.96	9.15	-	-	-
WISEA J100438.82+151057.0	82.5	4862.85	2.32	19.65	4854.71	32.1	21.06	4869.49	14.0	-	-	-	-	-	-
PG 1138+222	452.51	4862.78	1.74	89.34	4865.02	25.89	112.52	4864.76	10.59	-	-	-	-	-	-
WISEA J124800.54+100958.9	45.85	4862.06	1.81	20.74	4860.19	27.04	14.81	4859.77	8.4	-	-	-	-	-	-
WISEA J121224.89+185920.2	47.66	4861.18	1.87	20.55	4868.45	26.26	37.77	4863.26	12.37	-	-	-	-	-	-
MRK 0783	280.81	4861.47	2.82	85.64	4877.47	22.24	111.56	4862.8	9.35	-	-	-	-	-	-
WISEA J132213.38+214721.1	54.73	4863.06	1.46	10.56	4853.94	44.41	31.78	4863.51	4.74	-	-	-	-	-	-
WISEA J134915.20+220032.6	93.29	4862.42	2.75	30.04	4866.5	19.49	-	-	-	-	-	-	-	-	-
SBS 1527+564	99.05	4863.25	2.38	73.0	4853.63	22.64	66.59	4863.32	5.97	35.7	4884.27	11.57	-	-	-
WISEA J145842.74+213609.9	231.12	4863.15	1.41	34.71	4865.66	29.2	145.8	4861.31	8.06	33.63	4876.65	4.42	-	-	-
WISEA J152558.53+181416.0	52.13	4861.64	2.68	36.51	4862.85	20.0	-	-	-	9.68	4899.0	25.0	-	-	-
WISEA J152753.80+061018.9	55.36	4861.58	2.53	128.94	4866.0	26.97	69.41	4862.12	10.58	-	-	-	-	-	-
WISEA J145434.34+080336.7	30.47	4861.31	3.48	32.49	4867.3	25.56	33.21	4856.2	10.81	-	-	-	-	-	-
WISEA J150913.78+175710.1	29.71	4863.55	2.01	11.66	4859.38	32.33	58.3	4863.45	13.21	-	-	-	-	-	-
VII Zw 533	121.92	4863.49	1.84	96.2	4863.49	21.11	66.93	4858.75	8.68	33.52	4878.03	5.39	-	-	-

Table A.4: List of the fit parameter used for the Hβ line. The parameters are indicated with A for the amplitude, x^0 for the center, and w for the width, using this last parameter the Gaussians are divided in narrow (n), broad 1 (b1), broad 2 (b2), extra 1 (e1) and, extra 2 (e2).

Name	$\mathbf{A}_n$	$\mathbf{x}_n^0$	$\mathbf{w}_n$	$\mathbf{A}_b$	$\mathbf{x}_b^0$	$\mathbf{w}_b$	$\mathbf{A}_e$	$\mathbf{x}_e^0$	$\mathbf{w}_e$
WISEA J123022.17+662154.6	361.73	5009.22	2.34	136.52	5007.34	4.89	-	-	-
UM 614	1403.4	5008.13	1.85	385.55	5007.01	4.89	-	-	-
MRK 1392	2093.33	5008.76	2.07	976.11	5008.5	4.35	-	-	-
WISEA J235654.30-101605.4	901.11	5009.45	2.03	463.47	5007.58	3.53	-	-	-
MRK 0110	3194.92	5008.06	2.4	0.0	5007.0	1.0	-	-	-
WISEA J211646.34+110237.4	1287.8	5008.39	2.33	352.17	5008.78	6.24	-	-	-
WISEA J101043.35+061201.4	302.06	5009.12	3.7	175.91	5008.28	11.21	-	-	-
WISEA J115341.16+101754.0	367.59	5010.05	2.56	209.76	5004.11	6.45	-	-	-
MRK 0699	1237.99	5009.81	2.0	323.31	5007.6	3.96	-	-	-
WISEA J133120.18+484013.9	433.92	5007.64	1.63	105.37	5007.41	3.34	-	-	-
SBS 1340+569	356.18	5008.47	1.5	0.0	5007.0	1.0	-	-	-
WISEA J164819.02+302210.8	200.0	5004.08	2.4	100.0	5005.61	9.1	615.65	5011.13	2.82
[HB89] 1612+261	1820.25	5007.98	2.33	688.44	5006.54	4.79	-	-	-
WISEA J165551.37+214601.7	1338.97	5007.07	2.59	510.44	5008.1	5.13	-	-	-
FBQS J081738.3+242330	186.12	5006.67	1.79	378.21	5007.25	3.85	-	-	-
WISEA J084205.57+075925.5	590.09	5008.94	2.43	182.45	5006.59	8.39	-	-	-
WISEA J111907.07+413014.5	687.01	5008.34	2.98	0.0	5007.0	1.0	-	-	-
WISEA J105635.05+414602.6	773.13	5008.71	5.7	0.0	5007.0	1.0	-	-	-
B3 0745+453	500.05	5008.32	2.43	84.3	5006.05	6.74	-	-	-
CGCG 244-033	170.3	5007.91	1.46	120.41	5006.8	5.56	-	-	-
WISEA J104326.47+110524.2	2127.47	5008.93	1.57	0.0	5007.0	1.0	-	-	-
WISEA J114347.71+112847.8	262.03	5008.5	2.37	0.0	5007.0	1.0	-	-	-
WISEA J134548.50+114443.5	303.44	5007.68	1.83	225.13	5007.09	3.76	-	-	-
FBQS J1610+3303	323.45	5008.22	2.19	122.21	5007.36	6.59	-	-	-
WISEA J114434.72+070516.5	444.26	5008.34	1.86	204.59	5007.23	4.11	-	-	-
2MASS J12421060+3317027	798.13	5009.7	2.16	308.79	5005.82	5.86	-	-	-
WISEA J133624.05+391731.1	147.15	5008.55	2.74	69.05	5004.85	5.72	-	-	-
MRK 0646	445.28	5008.09	2.08	0.0	5007.0	1.0	-	-	-
VIII Zw 327	396.97	5008.0	2.14	0.0	5007.0	1.0	-	-	-
WISEA J091848.61+211717.0	109.6	5008.99	2.67	69.15	5005.74	7.61	-	-	-
MRK 1220	209.95	5009.2	2.15	332.35	5003.85	5.06	-	-	-
SDSS J104427.75+271806.3	98.13	5008.18	2.3	0.0	5007.0	1.0	-	-	-
[HB89] 1142+310	221.66	5009.34	1.59	52.54	5007.26	4.21	-	-	-
FBQS J1227+3214	290.28	5009.34	2.23	115.68	5005.74	4.98	-	-	-
WISEA J090723.56+171616.3	435.96	5007.91	1.82	113.66	5006.84	3.2	-	-	-
WISEA J161745.63+060353.5	1904.77	5008.46	2.41	0.0	5007.0	1.0	-	-	-
WISEA J100438.82+151057.0	281.25	5008.51	2.0	219.71	5006.64	3.37	-	-	-
PG 1138+222	2461.47	5008.65	1.67	1301.73	5007.51	2.94	-	-	-
WISEA J124800.54+100958.9	298.29	5007.35	2.01	0.0	5007.0	1.0	-	-	-
WISEA J121224.89+185920.2	444.62	5006.63	1.74	37.46	5007.66	4.33	-	-	-
MRK 0783	2364.41	5006.86	3.14	0.0	5007.0	1.0	-	-	-
WISEA J132213.38+214721.1	539.86	5008.51	1.59	206.08	5008.44	3.88	-	-	-
WISEA J134915.20+220032.6	365.04	5008.96	1.56	61.75	5005.22	7.2	778.67	5007.11	2.73
SBS 1527+564	1317.92	5009.05	2.22	512.87	5008.15	6.35	-	-	-
WISEA J145842.74+213609.9	1370.93	5008.86	1.57	0.0	5007.0	1.0	-	-	-
WISEA J152558.53+181416.0	122.12	5007.04	2.7	20.26	5003.31	6.59	-	-	-
WISEA J152753.80+061018.9	535.54	5007.21	2.58	46.36	5009.85	5.53	-	-	-
WISEA J145434.34+080336.7	142.25	5004.87	2.28	311.11	5008.8	5.23	-	-	-
WISEA J150913.78+175710.1	203.09	5009.99	2.15	82.0	5006.09	7.21	-	-	-
VII Zw 533	763.26	5009.04	1.76	296.8	5006.79	4.58	-	-	-

Table A.5: List of the fit parameter used for the [O III]λ5007 line. The parameters are indicated with A for the amplitude, x^0 for the center, and w for the width, using this last parameter the Gaussians are divided in narrow (n), broad (b), and extra (e).

Name	$\mathbf{A}_n$	$\mathbf{x}_n^0$	$\mathbf{w}_n$	$\mathbf{A}_b$	$\mathbf{x}_b^0$	$\mathbf{w}_b$	$\mathbf{A}_e$	$\mathbf{x}_e^0$	$\mathbf{w}_e$
WISEA J123022.17+662154.6	120.58	4960.9	2.31	45.51	4959.01	4.85	-	-	-
UM 614	467.8	4959.8	1.83	128.52	4958.68	4.84	-	-	-
MRK 1392	697.78	4960.43	2.05	325.37	4960.17	4.3	-	-	-
WISEA J235654.30-101605.4	300.37	4961.12	2.01	154.49	4959.26	3.5	-	-	-
MRK 0110	1064.97	4959.73	2.38	0.0	0.0	0.0	-	-	-
WISEA J211646.34+110237.4	429.27	4960.06	2.3	117.39	4960.46	6.18	-	-	-
WISEA J101043.35+061201.4	100.69	4960.79	3.67	58.64	4959.95	11.1	-	-	-
WISEA J115341.16+101754.0	122.53	4961.72	2.53	69.92	4955.78	6.39	-	-	-
MRK 0699	412.66	4961.48	1.98	107.77	4959.27	3.93	-	-	-
WISEA J133120.18+484013.9	144.64	4959.31	1.62	35.12	4959.08	3.3	-	-	-
SBS 1340+569	118.73	4960.14	1.49	0.0	0.0	0.0	-	-	-
WISEA J164819.02+302210.8	66.67	4955.75	2.37	33.33	4957.28	9.01	205.22	4962.8	2.79
[HB89] 1612+261	606.75	4959.65	2.31	229.48	4958.21	4.75	-	-	-
WISEA J165551.37+214601.7	446.32	4958.75	2.56	170.15	4959.77	5.08	-	-	-
FBQS J081738.3+242330	62.04	4958.34	1.77	126.07	4958.92	3.81	-	-	-
WISEA J084205.57+075925.5	196.7	4960.61	2.41	60.82	4958.26	8.31	-	-	-
WISEA J111907.07+413014.5	229.0	4960.01	2.95	0.0	0.0	0.0	-	-	-
WISEA J105635.05+414602.6	257.71	4960.38	5.65	0.0	0.0	0.0	-	-	-
B3 0745+453	166.68	4959.99	2.41	28.1	4957.72	6.68	-	-	-
CGCG 244-033	56.77	4959.58	1.45	40.14	4958.47	5.5	-	-	-
WISEA J104326.47+110524.2	708.9	4960.6	1.56	0.0	0.0	0.0	-	-	-
WISEA J114347.71+112847.8	87.29	4960.17	2.35	0.0	0.0	0.0	-	-	-
WISEA J134548.50+114443.5	101.15	4959.35	1.81	75.04	4958.76	3.73	-	-	-
FBQS J1610+3303	107.82	4959.9	2.17	40.74	4959.03	6.52	-	-	-
WISEA J114434.72+070516.5	148.09	4960.01	1.84	68.2	4958.9	4.07	-	-	-
2MASS J12421060+3317027	49.05	4960.22	2.71	102.93	4957.49	5.86	-	-	-
WISEA J133624.05+391731.1	148.43	4959.76	2.06	23.02	4956.52	5.67	-	-	-
MRK 0646	266.04	4961.37	2.16	0.0	0.0	0.0	-	-	-
VIII Zw 327	132.32	4959.68	2.11	0.0	0.0	0.0	-	-	-
WISEA J091848.61+211717.0	36.53	4960.66	2.64	23.05	4957.41	7.54	-	-	-
MRK 1220	69.98	4960.87	2.13	110.78	4955.52	5.01	-	-	-
SDSS J104427.75+271806.3	32.71	4959.85	2.28	0.0	0.0	0.0	-	-	-
[HB89] 1142+310	73.89	4961.01	1.57	17.51	4958.93	4.17	-	-	-
FBQS J1227+3214	96.76	4961.01	2.21	38.56	4957.41	4.93	-	-	-
WISEA J090723.56+171616.3	145.32	4959.59	1.81	37.89	4958.51	3.17	-	-	-
WISEA J161745.63+060353.5	634.92	4960.13	2.38	0.0	0.0	0.0	-	-	-
WISEA J100438.82+151057.0	93.75	4960.18	1.98	73.24	4958.32	3.34	-	-	-
PG 1138+222	820.49	4960.33	1.65	433.91	4959.18	2.91	-	-	-
WISEA J124800.54+100958.9	99.43	4959.02	1.99	0.0	0.0	0.0	-	-	-
WISEA J121224.89+185920.2	148.21	4958.3	1.72	12.49	4959.33	4.28	-	-	-
MRK 0783	788.14	4958.53	3.11	0.0	0.0	0.0	-	-	-
WISEA J132213.38+214721.1	179.95	4960.18	1.57	68.69	4960.12	3.84	-	-	-
WISEA J134915.20+220032.6	121.68	4961.05	1.54	20.58	4956.64	7.13	259.56	4959.12	2.71
SBS 1527+564	439.31	4960.72	2.2	170.96	4959.82	6.29	-	-	-
WISEA J145842.74+213609.9	456.98	4960.53	1.56	0.0	0.0	0.0	-	-	-
WISEA J152558.53+181416.0	40.71	4958.72	2.67	6.75	4954.98	6.53	-	-	-
WISEA J152753.80+061018.9	178.51	4958.88	2.55	15.45	4961.52	5.47	-	-	-
WISEA J145434.34+080336.7	47.42	4956.54	2.26	103.7	4960.47	5.18	-	-	-
WISEA J150913.78+175710.1	67.7	4961.66	2.15	27.33	4957.76	7.21	-	-	-
VII Zw 533	254.42	4960.72	1.74	98.93	4958.46	4.53	-	-	-

Table A.6: List of the fit parameter used for the [O III]λ4959 line. The parameters are indicated with A for the amplitude, x^0 for the center, and w for the width, using this last parameter the Gaussians are divided in narrow (n), broad (b), and extra (e).

Name	A_n	x_n^0	w_n	A_b	x_b^0	w_b
WISEA J123022.17+662154.6	55.09	6587.45	2.86	-	-	-
UM 614	216.55	6585.21	3.0	87.89	6580.45	7.0
MRK 1392	776.9	6585.85	3.82	-	-	-
WISEA J235654.30-101605.4	221.78	6586.55	3.92	-	-	-
MRK 0110	223.45	6584.96	3.62	-	-	-
WISEA J211646.34+110237.4	162.21	6585.37	2.82	83.68	6586.42	8.98
WISEA J101043.35+061201.4	118.07	6585.84	6.08	-	-	-
WISEA J115341.16+101754.0	99.97	6587.81	4.75	-	-	-
MRK 0699	196.53	6587.45	3.0	-	-	-
WISEA J133120.18+484013.9	25.14	6584.55	1.27	-	-	-
SBS 1340+569	63.87	6585.73	1.61	-	-	-
WISEA J164819.02+302210.8	95.66	6587.83	9.91	-	-	-
[HB89] 1612+261	194.5	6584.38	3.54	-	-	-
WISEA J165551.37+214601.7	81.74	6582.93	4.12	-	-	-
FBQS J081738.3+242330	23.39	6568.92	10.62	-	-	-
WISEA J084205.57+075925.5	117.26	6586.24	3.95	-	-	-
WISEA J111907.07+413014.5	45.25	6584.59	4.62	-	-	-
WISEA J105635.05+414602.6	85.35	6584.92	6.63	-	-	-
B3 0745+453	96.99	6586.12	5.26	-	-	-
CGCG 244-033	111.9	6585.47	2.73	-	-	-
WISEA J104326.47+110524.2	85.72	6586.23	2.17	-	-	-
WISEA J114347.71+112847.8	82.63	6584.99	2.36	-	-	-
WISEA J134548.50+114443.5	55.68	6584.38	3.85	-	-	-
FBQS J1610+3303	42.25	6587.12	5.0	-	-	-
WISEA J114434.72+070516.5	95.95	6585.45	3.27	-	-	-
2MASS J12421060+3317027	240.98	6587.72	3.11	-	-	-
WISEA J133624.05+391731.1	130.01	6586.73	3.98	-	-	-
MRK 0646	204.29	6586.12	2.56	-	-	-
VIII Zw 327	54.41	6585.35	3.58	-	-	-
WISEA J091848.61+211717.0	63.06	6586.94	6.0	-	-	-
MRK 1220	352.46	6587.45	2.0	105.93	6583.45	9.38
SDSS J104427.75+271806.3	97.35	6585.14	2.9	-	-	-
[HB89] 1142+310	391.56	6587.14	1.81	-	-	-
FBQS J1227+3214	19.91	6586.89	2.03	-	-	-
WISEA J090723.56+171616.3	57.34	6584.36	2.81	-	-	-
WISEA J161745.63+060353.5	212.12	6585.41	3.2	-	-	-
WISEA J100438.82+151057.0	73.01	6585.35	3.39	-	-	-
PG 1138+222	285.22	6585.86	2.56	-	-	-
WISEA J124800.54+100958.9	11.04	6585.45	2.63	-	-	-
WISEA J121224.89+185920.2	15.19	6582.75	4.0	-	-	-
MRK 0783	231.97	6583.4	3.67	-	-	-
WISEA J132213.38+214721.1	85.17	6584.84	4.78	-	-	-
WISEA J134915.20+220032.6	143.87	6586.22	4.11	-	-	-
SBS 1527+564	55.45	6585.71	2.75	-	-	-
WISEA J145842.74+213609.9	130.43	6586.01	1.51	-	-	-
WISEA J152558.53+181416.0	121.69	6584.03	3.43	-	-	-
WISEA J152753.80+061018.9	166.41	6577.5	13.68	-	-	-
WISEA J145434.34+080336.7	158.04	6584.45	7.0	-	-	-
WISEA J150913.78+175710.1	84.13	6586.13	3.7	-	-	-
VII Zw 533	104.91	6586.8	5.21	-	-	-

Name	A_n	x_n^0	w_n	A_b	x_b^0	w_b
WISEA J123022.17+662154.6	58.33	3728.91	2.68	-	-	-
UM 614	379.92	3727.96	3.21	-	-	-
MRK 1392	574.57	3728.5	3.01	-	-	-
WISEA J235654.30-101605.4	260.21	3728.65	2.75	-	-	-
MRK 0110	895.62	3728.09	2.44	-	-	-
WISEA J211646.34+110237.4	346.86	3728.83	2.38	147.97	3727.93	4.73
WISEA J101043.35+061201.4	97.67	3728.35	3.38	-	-	-
WISEA J115341.16+101754.0	94.06	3730.23	3.12	-	-	-
MRK 0699	145.41	3728.95	2.39	-	-	-
WISEA J133120.18+484013.9	59.89	3727.8	2.22	-	-	-
SBS 1340+569	296.53	3728.7	1.97	-	-	-
WISEA J164819.02+302210.8	142.91	3729.49	2.98	46.18	3726.86	4.6
[HB89] 1612+261	453.1	3727.84	3.11	-	-	-
WISEA J165551.37+214601.7	308.21	3727.92	3.23	-	-	-
FBQS J081738.3+242330	50.49	3727.46	3.24	-	-	-
WISEA J084205.57+075925.5	161.87	3728.82	2.8	-	-	-
WISEA J111907.07+413014.5	232.88	3728.58	2.81	-	-	-
WISEA J105635.05+414602.6	241.18	3728.4	4.67	-	-	-
B3 0745+453	99.09	3728.78	2.62	-	-	-
CGCG 244-033	109.17	3727.82	2.9	-	-	-
WISEA J104326.47+110524.2	477.56	3728.71	2.09	-	-	-
WISEA J114347.71+112847.8	79.39	3728.87	2.33	-	-	-
WISEA J134548.50+114443.5	101.05	3727.99	2.76	-	-	-
FBQS J1610+3303	72.25	3728.05	2.17	-	-	-
WISEA J114434.72+070516.5	58.66	3728.38	2.47	-	-	-
2MASS J12421060+3317027	179.67	3729.87	2.64	26.33	3722.76	4.43
WISEA J133624.05+391731.1	80.77	3729.41	2.64	-	-	-
MRK 0646	289.02	3728.99	2.18	-	-	-
VIII Zw 327	65.52	3727.94	2.31	-	-	-
WISEA J091848.61+211717.0	24.19	3729.63	3.67	-	-	-
MRK 1220	120.73	3729.88	2.09	-	-	-
SDSS J104427.75+271806.3	62.97	3728.68	2.48	-	-	-
[HB89] 1142+310	264.39	3729.4	2.07	-	-	-
FBQS J1227+3214	101.8	3728.92	2.64	8.39	3722.83	3.43
WISEA J090723.56+171616.3	78.72	3728.15	2.2	-	-	-
WISEA J161745.63+060353.5	593.86	3728.72	2.57	-	-	-
WISEA J100438.82+151057.0	178.51	3728.68	2.42	-	-	-
PG 1138+222	842.24	3728.54	2.11	-	-	-
WISEA J124800.54+100958.9	20.54	3727.95	2.35	-	-	-
WISEA J121224.89+185920.2	80.59	3727.41	2.42	-	-	-
MRK 0783	938.3	3727.07	2.8	-	-	-
WISEA J132213.38+214721.1	116.68	3728.49	2.68	-	-	-
WISEA J134915.20+220032.6	254.51	3728.47	2.95	-	-	-
SBS 1527+564	392.0	3727.87	3.21	-	-	-
WISEA J145842.74+213609.9	470.16	3728.96	2.05	-	-	-
WISEA J152558.53+181416.0	86.07	3728.21	2.37	-	-	-
WISEA J152753.80+061018.9	63.25	3727.49	2.69	-	-	-
WISEA J145434.34+080336.7	82.07	3728.38	4.12	-	-	-
WISEA J150913.78+175710.1	77.29	3729.35	2.95	-	-	-
VII Zw 533	69.7	3728.3	3.03	-	-	-

Table A.7: On the left there is the list of the fit parameter used for the [N II]λ6583 line. The parameters are indicated with A for the amplitude, x^0 for the center, and w for the width. In this case the only detected components are the narrow and broad ones. On the right, the same for [O II]λ3727. In this case the only detected components are the narrow and broad ones.

Name	A_n	x_n^0	w_n
WISEA J123022.17+662154.6	6.66	6303.49	3.73
UM 614	63.81	6301.66	3.36
MRK 1392	133.92	6302.86	3.28
WISEA J235654.30-101605.4	32.64	6303.34	3.2
MRK 0110	229.52	6302.15	3.14
WISEA J211646.34+110237.4	33.85	6302.17	2.44
WISEA J101043.35+061201.4	38.99	6303.93	8.97
WISEA J115341.16+101754.0	17.9	6305.18	3.8
MRK 0699	34.69	6303.57	2.75
WISEA J133120.18+484013.9	11.9	6301.59	2.56
SBS 1340+569	20.39	6302.37	1.94
WISEA J164819.02+302210.8	22.65	6303.2	7.09
[HB89] 1612+261	67.2	6301.35	3.81
WISEA J165551.37+214601.7	31.71	6301.54	3.34
FBQS J081738.3+242330	10.91	6300.82	4.68
WISEA J084205.57+075925.5	62.32	6302.42	5.08
WISEA J111907.07+413014.5	26.09	6302.3	3.62
WISEA J105635.05+414602.6	22.72	6301.92	6.36
B3 0745+453	10.86	6302.15	3.53
CGCG 244-033	26.02	6302.33	2.97
WISEA J104326.47+110524.2	84.88	6302.98	2.23
WISEA J114347.71+112847.8	11.65	6302.23	2.61
WISEA J134548.50+114443.5	12.43	6300.63	3.97
FBQS J1610+3303	9.7	6301.88	4.33
WISEA J114434.72+070516.5	16.44	6302.15	2.77
2MASS J12421060+3317027	21.79	6304.39	3.91
WISEA J133624.05+391731.1	12.32	6303.96	3.8
MRK 0646	31.04	6302.58	2.4
VIII Zw 327	16.06	6302.01	2.72
WISEA J091848.61+211717.0	4.25	6302.46	6.19
MRK 1220	25.34	6304.4	2.01
SDSS J104427.75+271806.3	7.36	6302.41	2.92
[HB89] 1142+310	20.57	6303.96	1.76
FBQS J1227+3214	16.26	6302.81	3.75
WISEA J090723.56+171616.3	7.58	6301.26	2.47
WISEA J161745.63+060353.5	61.28	6302.29	3.35
WISEA J100438.82+151057.0	13.77	6302.15	2.8
PG 1138+222	94.76	6302.36	2.25
WISEA J124800.54+100958.9	6.5	6301.64	2.84
WISEA J121224.89+185920.2	11.77	6299.98	2.99
MRK 0783	112.93	6300.77	3.6
WISEA J132213.38+214721.1	13.46	6302.36	3.0
WISEA J134915.20+220032.6	38.98	6303.11	3.33
SBS 1527+564	51.7	6302.49	4.03
WISEA J145842.74+213609.9	31.2	6302.83	1.72
WISEA J152558.53+181416.0	10.21	6301.35	3.25
WISEA J152753.80+061018.9	21.5	6300.83	3.49
WISEA J145434.34+080336.7	12.21	6302.88	6.5
WISEA J150913.78+175710.1	12.79	6303.2	4.24
VII Zw 533	25.4	6302.91	3.05

Name	A_n	x_n^0	w_n
WISEA J123022.17+662154.6	14.91	6719.27	3.2
UM 614	89.21	6718.37	3.79
MRK 1392	191.49	6718.85	3.92
WISEA J235654.30-101605.4	76.86	6719.85	3.29
MRK 0110	177.63	6716.88	3.19
WISEA J211646.34+110237.4	106.38	6718.78	3.72
WISEA J101043.35+061201.4	38.86	6719.12	4.87
WISEA J115341.16+101754.0	22.15	6721.44	4.04
MRK 0699	39.14	6720.23	2.42
WISEA J133120.18+484013.9	14.0	6716.7	2.39
SBS 1340+569	57.45	6718.83	1.89
WISEA J164819.02+302210.8	41.34	6718.97	6.04
[HB89] 1612+261	101.22	6716.7	4.52
WISEA J165551.37+214601.7	62.84	6716.61	4.01
FBQS J081738.3+242330	5.9	6716.69	3.71
WISEA J084205.57+075925.5	46.18	6718.0	5.1
WISEA J111907.07+413014.5	30.23	6718.6	4.16
WISEA J105635.05+414602.6	46.38	6718.35	7.31
B3 0745+453	23.17	6718.61	3.03
CGCG 244-033	47.77	6718.8	3.42
WISEA J104326.47+110524.2	96.49	6719.14	2.06
WISEA J114347.71+112847.8	36.25	6718.52	2.54
WISEA J134548.50+114443.5	21.89	6716.68	3.57
FBQS J1610+3303	14.19	6716.88	2.88
WISEA J114434.72+070516.5	17.3	6718.73	2.82
2MASS J12421060+3317027	81.52	6720.85	3.32
WISEA J133624.05+391731.1	33.85	6720.5	3.85
MRK 0646	75.81	6719.23	2.51
VIII Zw 327	14.87	6716.24	2.8
WISEA J091848.61+211717.0	11.49	6721.44	4.73
MRK 1220	99.97	6721.26	1.97
SDSS J104427.75+271806.3	28.56	6718.27	2.7
[HB89] 1142+310	140.53	6720.21	1.83
FBQS J1227+3214	23.07	6719.68	3.53
WISEA J090723.56+171616.3	23.9	6716.66	2.79
WISEA J161745.63+060353.5	82.14	6718.61	3.45
WISEA J100438.82+151057.0	37.51	6718.86	3.15
PG 1138+222	165.29	6718.73	2.13
WISEA J124800.54+100958.9	3.15	6716.55	1.9
WISEA J121224.89+185920.2	11.4	6716.33	2.59
MRK 0783	182.76	6716.79	3.75
WISEA J132213.38+214721.1	42.02	6718.83	3.62
WISEA J134915.20+220032.6	71.4	6719.47	3.68
SBS 1527+564	75.52	6718.12	4.33
WISEA J145842.74+213609.9	109.98	6719.03	1.82
WISEA J152558.53+181416.0	32.45	6716.51	3.28
WISEA J152753.80+061018.9	9.94	6716.12	3.04
WISEA J145434.34+080336.7	33.24	6718.1	6.57
WISEA J150913.78+175710.1	31.54	6719.75	3.64
VII Zw 533	20.84	6718.98	2.81

Name	A_n	x_n^0	w_n
WISEA J123022.17+662154.6	15.16	6734.2	3.21
UM 614	91.54	6732.28	3.78
MRK 1392	196.94	6733.12	3.91
WISEA J235654.30-101605.4	73.72	6734.46	3.28
MRK 0110	160.58	6732.33	3.19
WISEA J211646.34+110237.4	98.78	6732.63	3.71
WISEA J101043.35+061201.4	38.74	6733.99	4.86
WISEA J115341.16+101754.0	19.87	6735.82	4.03
MRK 0699	42.45	6734.6	2.42
WISEA J133120.18+484013.9	14.11	6732.06	2.38
SBS 1340+569	42.89	6733.3	1.88
WISEA J164819.02+302210.8	36.13	6734.08	6.03
[HB89] 1612+261	96.6	6731.65	4.51
WISEA J165551.37+214601.7	55.44	6731.47	4.01
FBQS J081738.3+242330	6.71	6730.95	3.7
WISEA J084205.57+075925.5	42.92	6732.28	5.09
WISEA J111907.07+413014.5	25.31	6733.08	4.15
WISEA J105635.05+414602.6	42.71	6733.21	7.3
B3 0745+453	17.66	6732.65	3.02
CGCG 244-033	38.5	6732.84	3.41
WISEA J104326.47+110524.2	81.79	6733.49	2.06
WISEA J114347.71+112847.8	28.84	6732.82	2.53
WISEA J134548.50+114443.5	19.29	6731.79	3.56
FBQS J1610+3303	15.41	6732.06	2.87
WISEA J114434.72+070516.5	20.18	6733.21	2.82
2MASS J12421060+3317027	76.13	6734.8	3.31
WISEA J133624.05+391731.1	29.98	6734.82	3.84
MRK 0646	64.02	6733.6	2.51
VIII Zw 327	15.07	6732.44	2.79
WISEA J091848.61+211717.0	9.8	6735.82	4.72
MRK 1220	80.56	6735.51	1.96
SDSS J104427.75+271806.3	24.75	6732.76	2.69
[HB89] 1142+310	113.08	6734.62	1.82
FBQS J1227+3214	18.12	6733.46	3.52
WISEA J090723.56+171616.3	19.79	6732.16	2.78
WISEA J161745.63+060353.5	75.16	6732.79	3.45
WISEA J100438.82+151057.0	30.61	6733.02	3.14
PG 1138+222	144.01	6733.04	2.12
WISEA J124800.54+100958.9	3.42	6731.66	1.89
WISEA J121224.89+185920.2	10.12	6730.59	2.58
MRK 0783	141.28	6731.05	3.75
WISEA J132213.38+214721.1	34.35	6732.49	3.61
WISEA J134915.20+220032.6	61.17	6733.64	3.67
SBS 1527+564	72.62	6732.62	4.32
WISEA J145842.74+213609.9	85.54	6733.49	1.82
WISEA J152558.53+181416.0	26.87	6731.86	3.27
WISEA J152753.80+061018.9	10.71	6731.2	3.03
WISEA J145434.34+080336.7	41.25	6732.84	6.56
WISEA J150913.78+175710.1	25.7	6733.75	3.63
VII Zw 533	27.2	6733.29	2.81

Table A.8: On the left there is the list of the fit parameter used for the [O I]λ6300 line. The parameters are indicated with A for the amplitude, x^0 for the center, and w for the width, in this case the only detected component is the narrow one. In the center, the list of the fit parameter used for the [S II]λ6716 line. In this case the only detected component is the narrow one. On the right, the list of the fit parameter used for the [S II]λ6731 line. In this case the only detected component is the narrow one.

Appendix B

Plots and images

Figures B.1, B.2, and B.3: the velocity diagrams made for the pathological sources. The comparison is between Hα and Hβ. The idea is to understand if the BLR emission correspond in the two profiles. Figures B.4 and B.5: the SDSS images from http://cdsportal.u-strasbg.fr of the pathological objects in the sample. The field of view in these cases is always 2.61'. The source is at the center identified by the red cross.

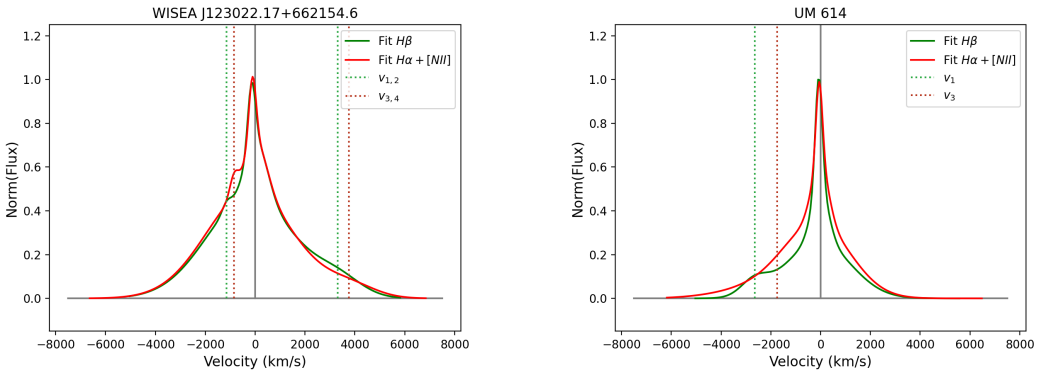

(a)

(b)

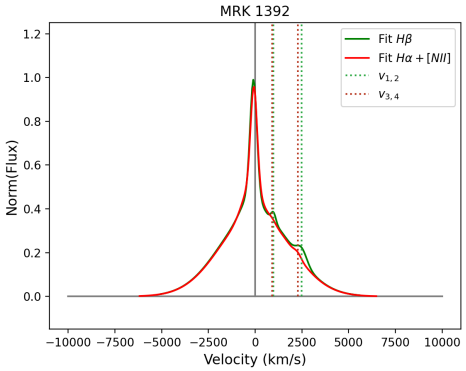

(c)

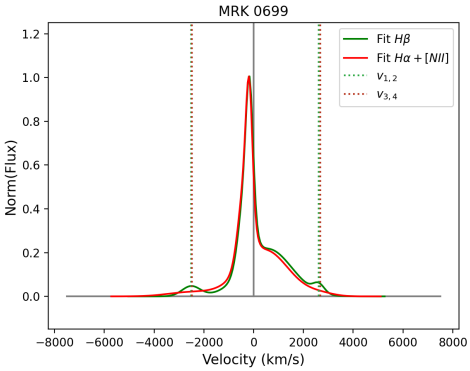

(d)

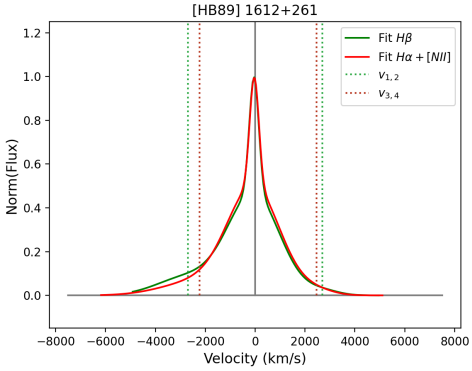

(e)

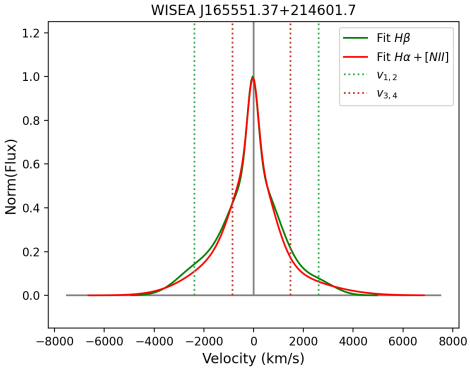

(f)

Figure B.1

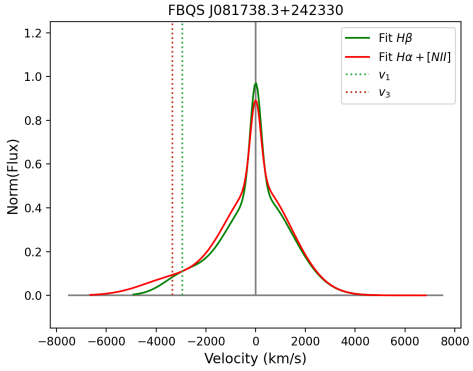

(a)

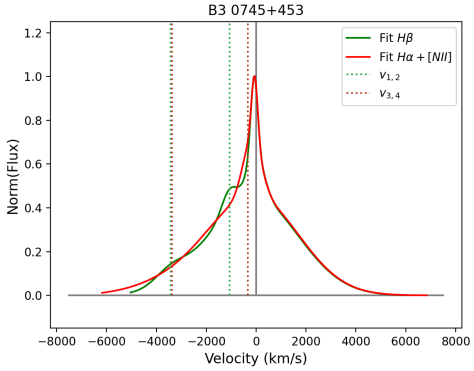

(b)

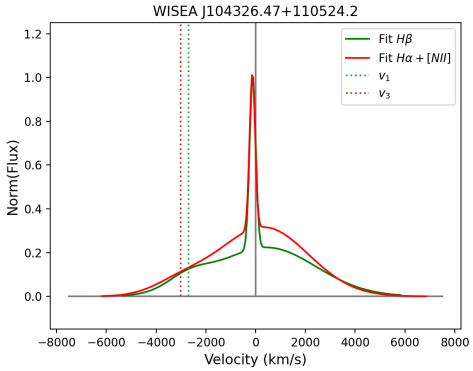

(c)

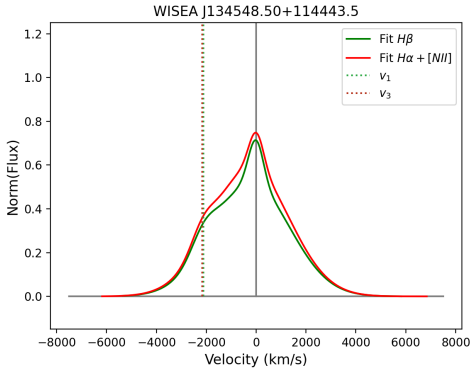

(d)

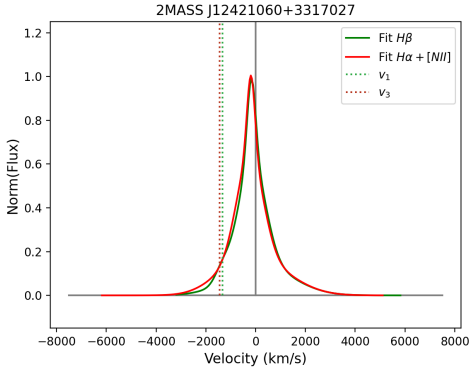

(e)

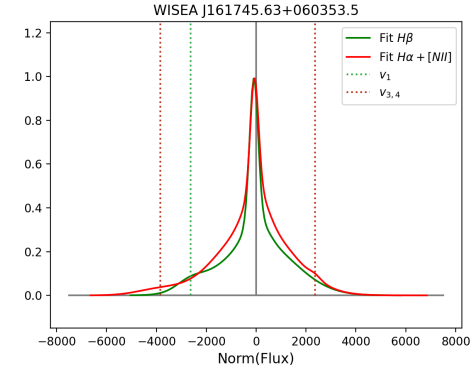

(f)

Figure B.2

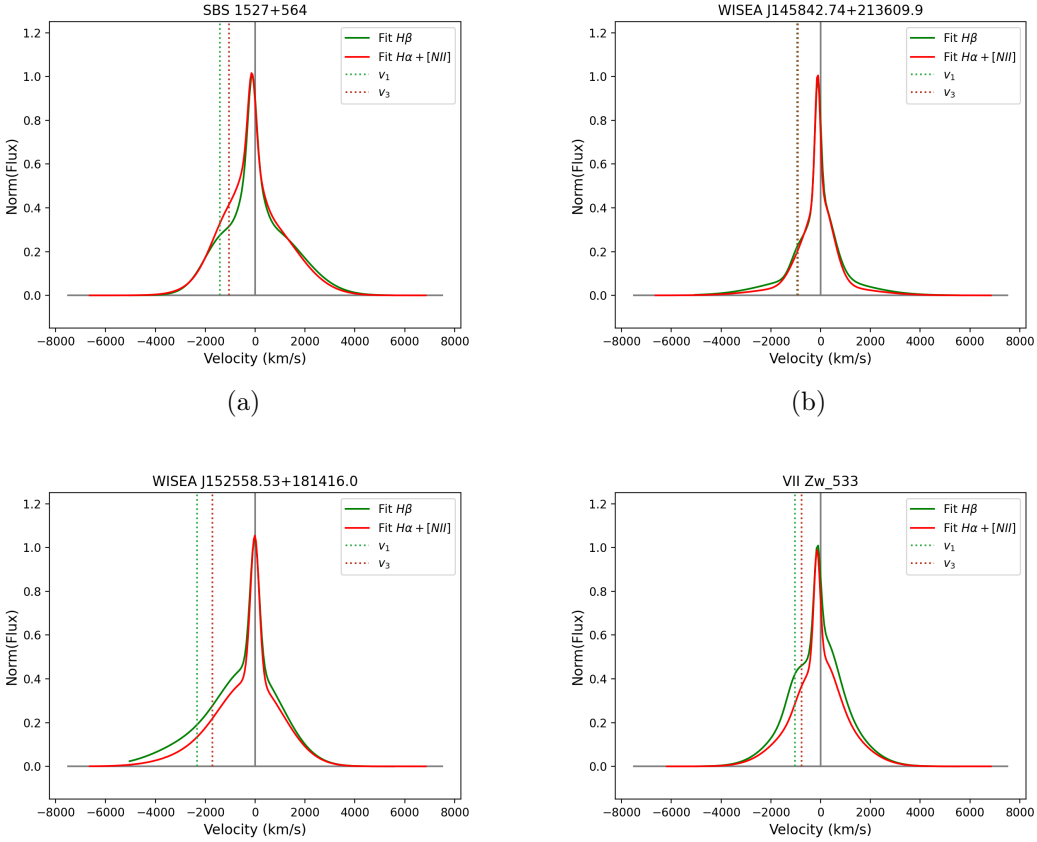

(a) (b)

(c) (d)

Figure B.3

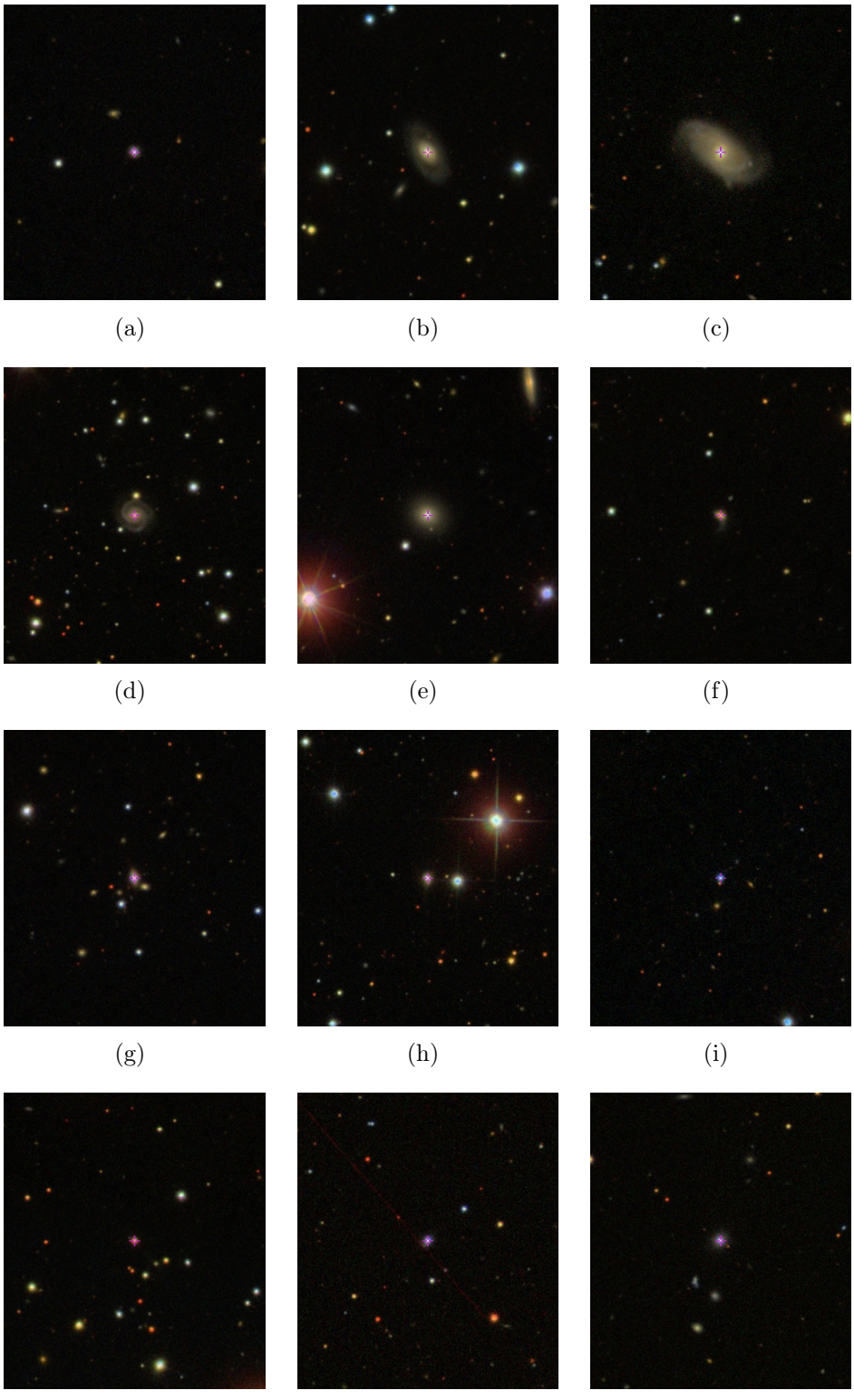

Figure B.4: (a) *WISEA J123022.17+662154.6*, (b) *UM 614*, (c) *MRK 1392*, (d) *WISEA J211646.34+110237.4*, (e) *MRK 0699*, (f) *WISEA J164819.02+302210.8*, (g) *[HB89] 1612+261*, (h) *WISEA J165551.37+214601.7*, (i) *FBQS J081738.3+242330*, (j) *WISEA J084205.57+075925.5*, (k) *B3 0745+453*, and (l) *WISEA J104326.47+110524.2*.

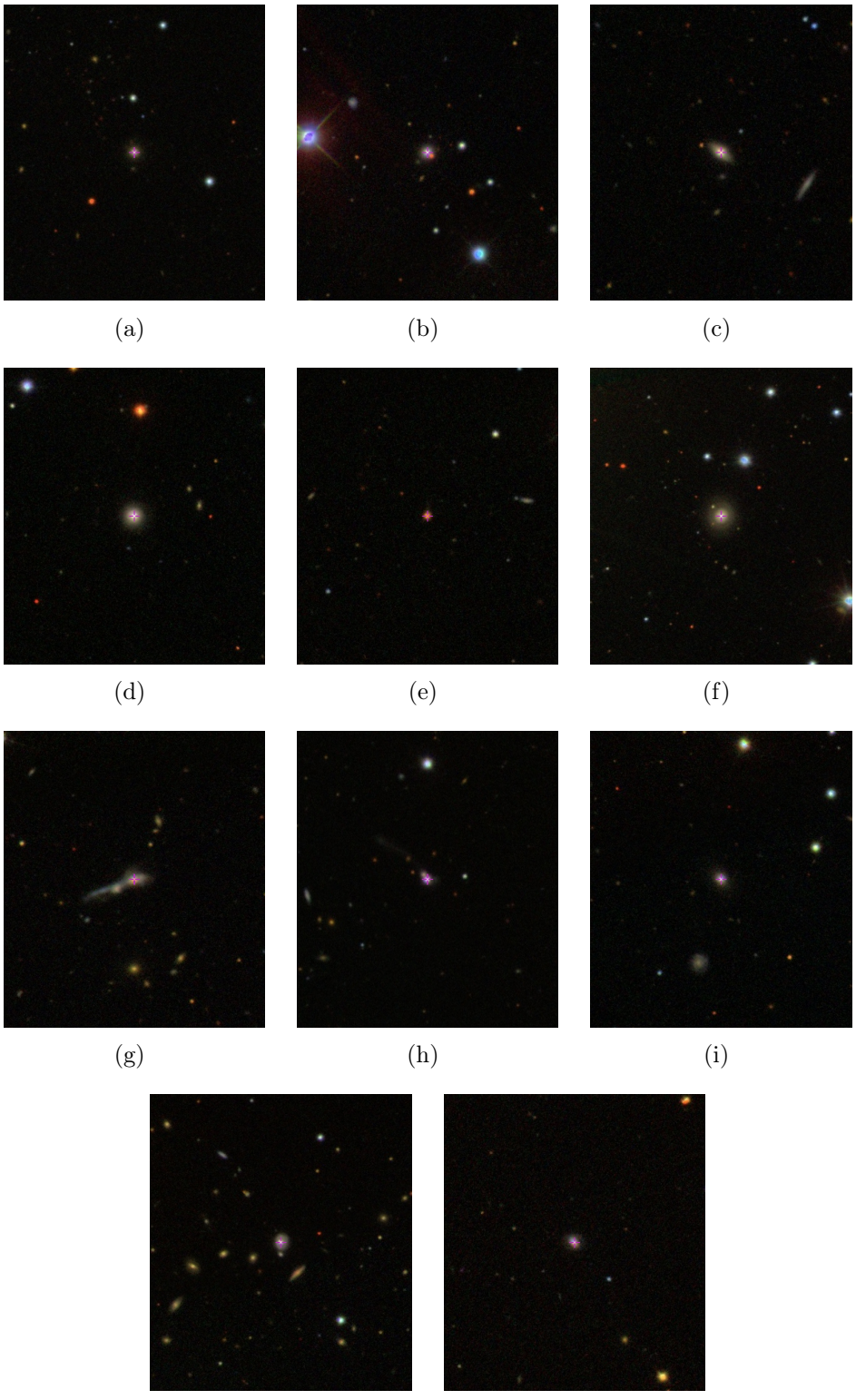

Figure B.5: (a) *WISEA J134548.50+114443.5*, (b) *FBQS J1610+3303*, (c) *2MASS J12421060+3317027*, (d) *MRK 1220*, (e) *FBQS J1227+3214*, (f) *WISEA J161745.63+060353.5*, (g) *WISEA J134915.20+220032.6*, (h) *SBS 1527+564*, (i) *WISEA J145842.74+213609.9*, (j) *WISEA J152558.53+181416.0*, and (k) *VII Zw 533*.